

# **A STUDY ON EXPERIMENTAL DETERMINATION OF MIXED-MODE SIF'S USING DIGITAL PHOTOELASTICITY AND DIC**

Vikrant V. Veerkar

A Dissertation Submitted to  
Indian Institute of Technology Hyderabad  
In Partial Fulfillment of the Requirements for  
The Degree of Master of Technology



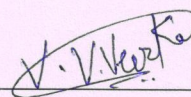
भारतीय प्रौद्योगिकी संस्थान हैदराबाद  
Indian Institute of Technology Hyderabad

Department of Mechanical Engineering

July, 2012

## **Declaration**

I declare that this written submission represents my ideas in my own words, and where others' ideas or words have been included, I have adequately cited and referenced the original sources. I also declare that I have adhered to all principles of academic honesty and integrity and have not misrepresented or fabricated or falsified any idea/data/fact/source in my submission. I understand that any violation of the above will be a cause for disciplinary action by the Institute and can also evoke penal action from the sources that have thus not been properly cited, or from whom proper permission has not been taken when needed.



(Signature)

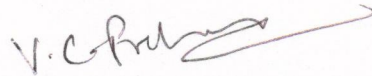
Vikrant V. Veerkar

ME10M12



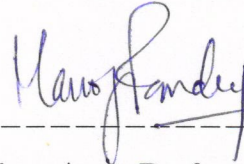
## Approval Sheet

This thesis entitled 'A Study on Experimental Determination of Mixed-mode SIF's using Digital Photoelasticity and DIC' by Veerkar Vikrant Vinod is approved for the degree of Master of Technology from IIT Hyderabad.



-----  
Dr. Chandrika Prakash Vyasarayani, Asst. Professor, IIT Hyderabad

Examiner



-----  
Dr. Manoj Pandey, Asst. Professor, IIT Hyderabad

Examiner



-----  
Dr. M. Ramji, Asst. Professor, IIT Hyderabad

Adviser



-----  
Dr. B. Umashankar, Asst. Professor, IIT Hyderabad

Chairman

## **Acknowledgements**

Apart from my efforts, the success of this project work depends largely on the encouragement and guidelines of many others. I take this opportunity to express my gratitude to the people who have been instrumental in the successful completion of this work.

I sincerely acknowledge my guide Dr. M. Ramji for his valuable guidance, encouragement and inspiration throughout my work. I wish to express a deep sense of gratitude towards him.

I would like to acknowledge Mr. RGR Prasath (Guru Sir) for his constant support and many useful suggestions for this work. I would like to thank research scholar Mr. Mohammad Kashfuddoja for his help and suggestions which helped me in completing this work in time. I am very thankful to my colleagues at engineering optics lab, Jabir, Naresh, Rahul and Vishwajeet for their valuable assistance in the project work. I am also thankful to Mr. K. Sathyanarayana, Project Engineer In-charge, Central Workshop and Mr. P. Raju, Project Engineer, Central Workshop for informative discussions. I would also like to thank Mr. A. Praveen Kumar, Mr. S. Jagadeesan, Mr. S. Velmurugan, Mr. Moulali Syed and all the other staff of Central Workshop for giving me valuable suggestions in specimen preparation.

I am thankful to all my M. Tech. (Design) class mates and all my M. Tech. batch mates for their help and support during the completion of my post-graduation. I also thank all my 600 series friends for making my very first hostel stay a wonderful and memorable experience.

I am obliged to my parents who have always inspired and supported me throughout my life despite any adverse situation. My brother, Devendra, Grandparents and other family members are also very much supportive to me. I am greatly indebted to all of them.



*Dedicated to*

*All My Teachers including My Parents*

*and*

*My Beloved Friends*

## **Abstract**

Several experimental techniques can be used for the estimation of mixed-mode SIF's. Out of these, digital photoelasticity and digital image correlation (DIC) have evolved as the most preferred techniques for the evaluation of fracture parameters. The present study attempts to evaluate SIF's for different specimen configurations using digital photoelasticity and DIC. For photoelastic determination of SIF's, an over-deterministic nonlinear least square approach has been used. Isochromatic fringe order has been evaluated over the entire model domain by using ten-step method. Using the techniques of digital image processing, data required for evaluation of SIF's has been collected in an automated manner. The methodology has been applied for the extraction of SIF's for two different specimen configurations, single edge notched (SEN) panel and interacting parallel edge cracked panel. The experimental results have been compared with analytical and finite element (FE) estimates. For the estimation of mixed-mode SIF's using DIC, required displacement data has been obtained using 3D-DIC. Using this data as an input, over-deterministic nonlinear least square approach has been implemented in modified form for reliable and better convergence of solution. For this purpose, MATLAB program has been written. In order to ensure the sufficiency of number of parameters, displacement field has been reconstructed theoretically to compare it with the experimentally obtained displacement distribution. The presented methodology has been used to extract mixed-mode SIF's for various specimen configurations. The experimentally obtained results are compared with the analytical solutions available in the literature.

# Nomenclature

SIF	Stress Intensity Factor
FEM	Finite Element Method
DIC	Digital Image Correlation
$N$	Total Isochromatic Fringe Order
$u, u_x$	Horizontal component of displacement
$v, u_y$	Vertical component of displacement



# Contents

Declaration.....	ii
Approval Sheet .....	iii
Acknowledgements.....	iv
Abstract.....	vi
Nomenclature.....	vii
List of Figures.....	1
List of Tables.....	3
<b>1 Introduction and Literature Review .....</b>	<b>4</b>
1.1 Introduction .....	4
1.2 Literature Review .....	5
1.2.1 Evaluation of fracture parameters using digital photoelasticity .....	5
1.2.2 Estimation of fracture parameters using digital image correlation (DIC) .....	9
1.3 Scope and Motivation.....	13
1.4 Thesis layout.....	13
<b>2 Photoelastic Determination of SIF's .....</b>	<b>14</b>
2.1 Introduction .....	14
2.2 Multi-parameter stress field equations.....	15
2.2.1 Tri-axial state of stress.....	16
2.2.2 Finite slit-tip radius.....	16
2.2.3 Stress-singularity .....	16
2.2.4 Localized crack-tip blunting.....	16
2.2.5 Plastic zone ahead of the crack-tip .....	16
2.3 Digital photoelastic parameter estimation using Ten-step method.....	17
2.4 Over-deterministic Non-linear Least Square Methodology.....	19
2.4.1 Formulation of equations.....	19
2.4.2 Convergence criteria.....	19
2.4.3 Implementation.....	20
2.5 Experimental Validation .....	20
2.5.1 Specimen preparation .....	20
2.5.2 Experimental procedure.....	21
2.5.3 Photoelastic analysis.....	23
2.6 Numerical computation of SIF's .....	29
2.7 Results and Discussion .....	31

2.8 Closure.....	33
<b>3 Estimation of SIF's using digital image correlation .....</b>	<b>34</b>
3.1 Introduction .....	34
3.2 Multi-parameter displacement field equations .....	36
3.3 Over-deterministic nonlinear least squares methodology .....	36
3.3.1 Formulation of equations.....	36
3.3.2 Convergence criteria.....	38
3.3.3 Implementation.....	38
3.4 Experimental validation.....	39
3.4.1 Specimen preparation .....	39
3.4.2 Experimental procedure.....	42
3.4.3 Data analysis.....	43
3.5 Results and Discussion .....	55
3.6 Closure.....	58
<b>4 Conclusion and Recommendations for Future Work .....</b>	<b>59</b>
<b>Appendix A.....</b>	<b>61</b>
<b>Appendix B.....</b>	<b>65</b>
<b>Appendix C.....</b>	<b>67</b>
<b>References.....</b>	<b>70</b>

# List of Figures

Fig. 1.1 Coordinate system with respect to a crack.....	4
Fig. 1.2 Dark field plane polariscope image of a disk under diametric compression showing both isoclinic and isochromatic fringe contours .....	6
Fig. 1.3 General procedure in digital photoelasticity for isochromatic parameter estimation:6	
Fig. 1.4 Dark field circular polariscope image of SEN specimen showing isochromatic fringe pattern around the crack-tip .....	7
Fig. 1.5 Schematic of deformation process in two dimensions with subsets in deformed and un-deformed state [20] .....	9
Fig. 1.6 (a) $u$ -displacement contour map and (b) $v$ -displacement contour map for SEN specimen obtained from 3D-DIC .....	11
Fig. 2.1 General steps involved in the photoelastic determination of mixed-mode SIF's ....	15
Fig. 2.2 Generic arrangement of a circular polariscope set-up .....	18
Fig. 2.3 Optical microscope image of notched epoxy specimen showing the details of the slit-tip .....	21
Fig. 2.4 Specimen geometry for (a) SEN panel, (b) Interacting parallel edge cracked panel21	
Fig. 2.5 (a) Experimental setup for digital photoelasticity, (b) Image recorded in a circular polariscope showing isochromatics, (c) Image recorded in a plane polariscope showing isochromatics as well as isoclinics .....	22
Fig. 2.6 Dark field isochromatic fringe pattern for (a) SEN specimen, (b) Interacting parallel edge cracked specimen.....	23
Fig. 2.7 Full field phase map obtained using ten-step method.....	24
Fig. 2.8 Full field phase map obtained using ten-step method for interacting parallel edge cracked specimen .....	25
Fig. 2.9 Reconstructed dark field fringe contours for SEN specimen obtained using various parameters .....	26
Fig. 2.10 Comparison of dark field image for SEN specimen (a) Experimentally obtained dark field isochromatic fringe pattern, (b) Theoretically reconstructed dark field isochromatic fringe contours with data points (shown by red colored dots).....	27
Fig. 2.11 Comparison of dark field image for interacting parallel edge cracked specimen..	28
Fig. 2.12 (a) Two coincident nodes near the crack tip before loading (b) Two nearest nodes near the crack tip after loading.....	30
Fig. 2.13 FE model of SEN specimen.....	30
Fig. 2.14 FE model of interacting parallel edge cracked specimen .....	31



Fig. 2.15 Experimentally obtained dark field isochromatic fringe pattern for (a) SEN specimen, (b) interacting parallel edge cracked specimen .....	32
Fig. 3.1 General steps involved in the determination of mixed-mode SIF's using DIC .....	35
Fig. 3.2 Specimen geometries for various specimen configurations.....	40
Fig. 3.3 showing the optical microscope image of short fatigue crack obtained for SEN specimen.....	41
Fig. 3.4 Experimental set-up used for 3D-DIC .....	42
Fig. 3.5 Experimental set-up used for ESC and CSC specimen .....	43
Fig. 3.6 showing the results of data analysis for SEN specimen.....	44
Fig. 3.7 showing the results of data analysis with subset size: 15×15 .....	45
Fig. 3.8 Theoretically reconstructed displacement field for SEN specimen for various parameters .....	46
Fig. 3.9 Theoretically reconstructed displacement field for SEN specimen (8-parameter solution) with data points echoed back (indicated by red marker points).....	47
Fig. 3.10 Graph showing (a) variation of $K_I$ (b) variation of $K_{II}$ as a function of number of parameters .....	48
Fig. 3.11 Graph of (a) convergence error and (b) co-ordinates of the crack-tip location vs. number of parameters.....	49
Fig. 3.12 Theoretically reconstructed displacement field for SCC specimen (14-parameter solution) with data points echoed back (indicated by red marker points).....	50
Fig. 3.13 Theoretically reconstructed displacement field for CSC specimen (14-parameter solution) with data points echoed back (indicated by red marker points).....	51
Fig. 3.14 Graph showing variation of $K_I$ as a function of number of parameters.....	51
Fig. 3.15 Graph showing variation of $K_{II}$ as a function of number of parameters.....	52
Fig. 3.16 Graph of co-ordinates of the crack-tip location vs. number of parameters.....	52
Fig. 3.17 Graph of convergence error vs. number of parameters.....	53
Fig. 3.18 Theoretically reconstructed displacement field for parallel edge cracked specimen (16-parameter solution) with data points echoed back (indicated by red marker points) .....	53
Fig. 3.19 Theoretically reconstructed displacement field for ESC specimen (8-parameter solution) with data points echoed back (indicated by red marker points).....	54
Fig. 3.20 showing the variation of mixed-mode SIF's for SEN specimen obtained using analytical and experimental (DIC) method as a function of applied load.....	55
Fig. 3.21 showing the variation of mixed-mode SIF's for SEN specimen obtained using analytical and experimental (DIC) method as a function of applied load.....	56

## List of Tables

Table 2.1 Optical arrangements for Ten-step phase shifting technique .....	18
Table 2.2 Parameters obtained for SEN specimen.....	28
Table 2.3 Parameters obtained for interacting parallel edge cracked specimen.....	28
Table 2.4 comparison of results obtained by different methods .....	32
Table 3.1 Summary of fatigue pre-cracking procedure.....	41
Table 3.2 comparison of results for SCC and ESC specimen obtained by different methods .....	57
Table 3.3 comparison of results obtained by different methods for parallel edge cracked panel.....	57

# Chapter 1

## Introduction and Literature Review

### 1.1 Introduction

Understanding the failures of the structures and components subjected to loading is very important for design engineers. It is well known fact that the presence of the flaws such as crack, sharp notches etc. in these engineering structures and components reduces their strength considerably and is mainly responsible for initiation of fracture. The causes for the presence of cracks or crack like defects are virtually impossible to avoid. The cracks can be introduced due to mechanical loading during manufacturing or because of the stresses induced during thermo-mechanical processing (such as welding or heat treatment) or during service (due to fatigue and/or creep, stress corrosion cracking, thermal stresses etc.) etc. Many catastrophic structural failures have occurred due to brittle fracture and even led to loss of life.

The presence of the crack results in the redistribution of stresses and strains around the crack-tip, the knowledge of which is essential for understanding the crack growth behavior and fracture. In fracture mechanics, stress intensity factor (SIF) is used to characterize the stress field around the crack tip. SIF depends on the far field stress ( $\sigma$ ), flaw size ( $a$ ), component geometry and the mode of loading.

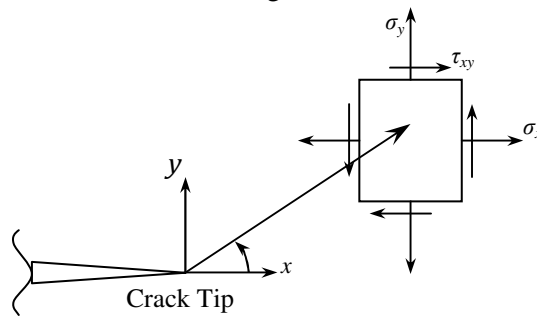


Fig. 1.1 Coordinate system with respect to a crack

$$\sigma_{ij} = \frac{K}{\sqrt{2\pi r}} f_{ij}(\theta) \quad (1.1)$$

Where,  $K$  = stress intensity factor; Unit =  $\text{MPa}\sqrt{\text{mm}}$



The SIF can be evaluated analytically, numerically and experimentally. Most of the analytical solutions are based on highly idealized models of the component geometry and give the basic relations between the parameters affecting the fracture. Analytical closed-form solutions are available for various simple configurations [1]. However, analytical techniques are rigorous and mostly applicable for simple geometries. For complex configurations, SIF need to be extracted by experimental or numerical analysis. The numerical methods especially finite element method (FEM) require precise knowledge about the boundary conditions and are required to be compared against analytical or experimental results for possible errors. The experimental methods are particularly well suited for determining SIF for specific geometry / loading conditions in situations where analytical or numerical methods fail to provide acceptable answers. Also, techniques of experimental stress analysis can be used to verify the solutions obtained by other methods. Many researchers have developed and applied methodologies for estimating SIF's using different experimental techniques. These experimental techniques include whole field non-contact optical methods such as holographic interferometry [2], electronic-speckle-pattern interferometry (ESPI) [3], moiré interferometry [3-4], coherent gradient sensing [5], method of caustics [6], photoelasticity, digital image correlation etc. as well as contact methods such as resistance strain gauges. Amongst these experimental techniques, digital photoelasticity and digital image correlation (DIC) have become the most popular ones for SIF determination because of their relatively simple specimen preparation, ease of use and requirement of less complicated optics. Thus, digital photoelasticity and DIC have been considered in this work for the estimation of fracture parameters (SIF's).

## **1.2 Literature Review**

### **1.2.1 Evaluation of fracture parameters using digital photoelasticity**

Photoelasticity is an optical, non-contact technique of whole field stress analysis which provides the information of principal stress difference (isochromatics) and principal stress direction (isoclinics) in the form of fringe contours. This is the only technique which can analyze both 2-D and 3-D elasticity problems (see Fig. 1.2). Though photoelasticity is a whole field technique, in the early days of its development, quantitative isoclinic ( $\theta_c$ ) and isochromatic ( $N$ ) data were obtained easily only at the fringe contours.

With the advent of personal computer based digital image processing systems, automation of photoelastic parameter estimation has now become simpler. A paradigm shift in data acquisition methodologies came into existence with the development of charge coupled device (CCD) cameras which could record intensity data at video rates. Several whole field

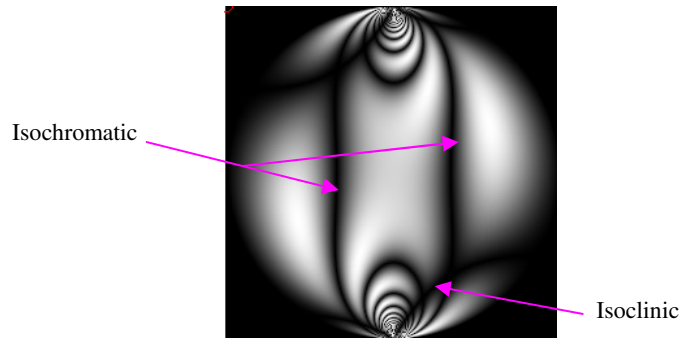


Fig. 1.2 Dark field plane polariscope image of a disk under diametric compression showing both isoclinic and isochromatic fringe contours

techniques were also developed. The techniques could be broadly classified into spatial domain and frequency domain methods. Phase shifting techniques (PST), polarization stepping techniques and load stepping come under spatial domain methods. Spatial domain methods require smaller number of images to be recorded (from three to ten in most cases). Further, they are computationally very fast and rugged. Hence, they are considered in this work for whole field isochromatic parameter estimation.

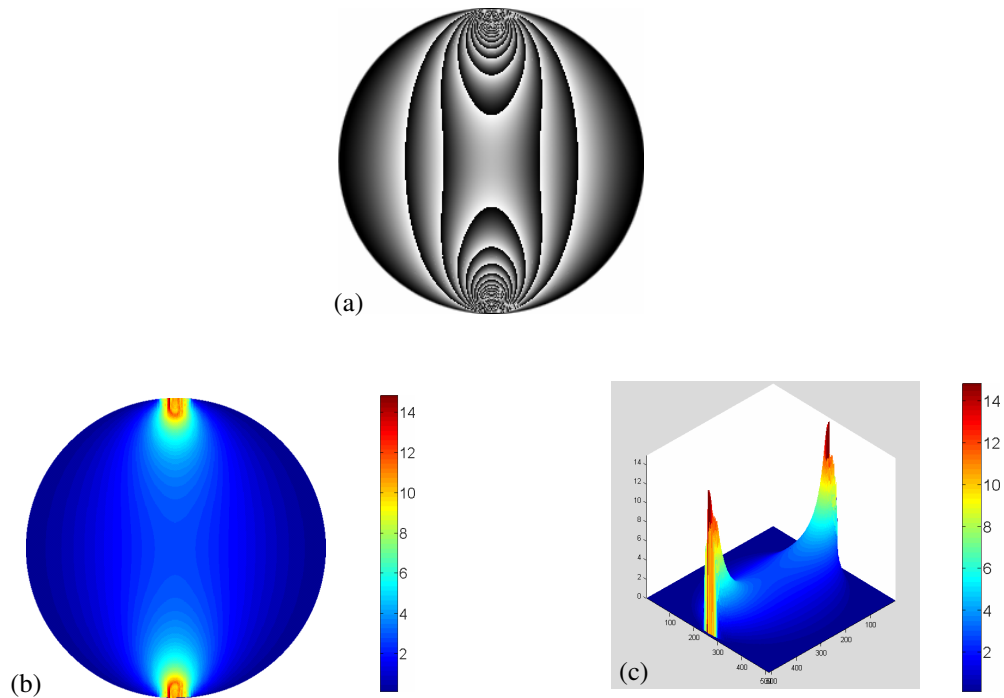


Fig. 1.3 General procedure in digital photoelasticity for isochromatic parameter estimation:

For the problem of a disk under diametric compression

(a) Isochromatic phasemap (b) unwrapped isochromatic phasemap (2-D plot)

(c) 3-D plot of the unwrapped isochromatic phasemap

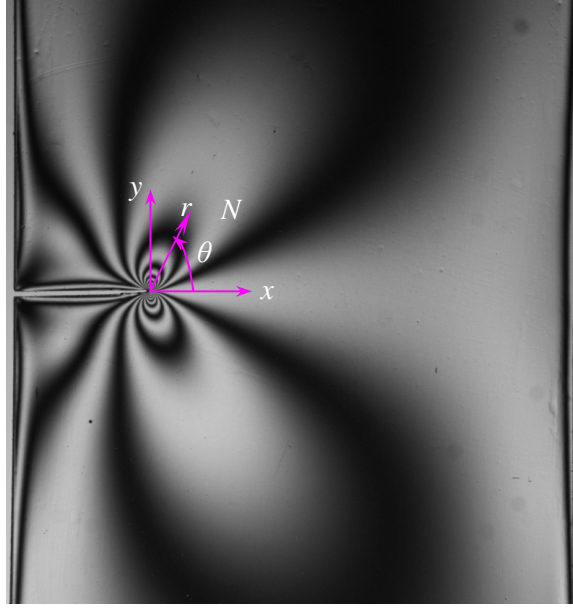


Fig. 1.4 Dark field circular polariscope image of SEN specimen showing isochromatic fringe pattern around the crack-tip

The phase shifting algorithms basically provide isochromatic values in the form of wrapped phasemaps which are different from the conventional fringe patterns of photoelasticity (Fig. 1.3a). The wrapped phasemap essentially gives the fractional retardation at the point of interest. Unwrapping of isochromatic phasemap refers to the suitable addition of integral value to the fractional retardation values for making it as a continuous phase data. The unwrapped isochromatic phasemap is shown in Fig. 1.3b and 3-D view of the unwrapped isochromatic phasemap is shown in Fig. 1.3c.

Dally and Sanford [7] used the theoretically constructed isochromatic fringe patterns to classify the state of stress at the crack tip and showed the influence of far field, non-singular stress (also called as  $T$ -stress -  $\sigma_{0x}$ ) on the shape, size and the orientation of isochromatic loops. Sanford and Dally [8] developed and applied the popular nonlinear over-deterministic least square methodology, involving multiple data points obtained from the whole field isochromatic fringe pattern near the crack tip, to determine the mixed-mode stress intensity factors ( $K_I$  and  $K_{II}$ ) and  $T$ -stress ( $\sigma_{0x}$ ). For that purpose, they used modified Westergaard equations (three-parameter solution) to obtain  $K$ - $N$  relation which relates the position coordinates ( $r$ ,  $\theta$ ) and the fringe order ( $N$ ) at the point of interest with the fracture parameters ( $K_I$ ,  $K_{II}$  and  $\sigma_{0x}$ ). (Refer Fig. 1.4) They showed the improvement in results, achieved because of the use of method of least square, over the conventional approaches (point measurement methods like selected line approach etc.) while successfully utilizing data ( $r$ ,  $\theta$  and  $N$ ) from multiple points. Sanford [9] showed that the linear and non-linear least square method can

be used, for any type of optical-stress analysis method which produces a fringe pattern over a field, to determine the certain key parameters (e.g. stress-optic coefficient in case of photoelasticity, fracture parameters etc.). Smith and Olaosebikan [10] employed the multiple-points over-deterministic least square algorithm, developed by Sanford and Dally to evaluate the mixed-mode SIF's from near-tip three dimensional stress-frozen photoelastic models. They emphasized the influence of initial (starting) estimates for the fracture parameters on the determination of mixed-mode SIF's which leads to inherent convergence problems. Nigam and Shukla [11] compared the values of mode-I SIF's obtained using the optical techniques of photoelasticity and method of caustics for the specimens with identical geometry under identical loading conditions. They found a good agreement between the results obtained by both techniques under static loading conditions. Mehdi-Soozani et al. [12] extracted mixed-mode SIF's for two interacting straight cracks using the photoelastic data ( $r$ ,  $\theta$  and  $N$ ) collected from digitally skeletonized isochromatic fringe patterns obtained from fringe thinning algorithm. They used the stress field equations in series expansion form derived from William's eigen function approach and also, considering the effect of higher order terms (up to seven) in the equations.

All the above approaches uses near-field equations to extract SIF's from whole field fringe pattern and the zone of data collection had to be confined to the singularity dominated zone which is very small in the specimens of finite geometry [13]. In order to increase the accuracy of measurement of SIF's and to take advantage of the additional information contained in the whole field fringe contours (which may not lie within the singularity dominated zone), Sanford [13] extended the over-deterministic least square algorithm and developed the method of local collocation by including few additional lower order non-singular terms (which may affect the fracture behavior such as crack branching and crack curvature). Taudou and Ravi-chandar [14] compared the values of dynamic mode-I SIF obtained for a moving crack using photoelasticity and method of caustics. They analyzed the effect of number of data points, their location on the isochromatic fringe loops and the number of terms needed in the stress field equation on the estimation of dynamic SIF. They observed that using too many number of terms in multi-parameter stress field equations does not necessarily improve the estimate of SIF's and a sensitivity analysis must be performed for determining the number of terms to be used in the stress field equations. They emphasized the fact that photoelasticity provides valuable visual information about the transient nature of dynamic fracture process that method of caustics fails to capture. Ramesh et al. [15] brought out the equivalence among the various multi-parameter stress field equations such as generalized Westergaard equations proposed by Sanford, Williams' eigen

function expansion and Atluri & Kobayashi equations. They evaluated the fracture parameters using Atluri and Kobayashi's multi-parameter stress field equations, following multi-points over-deterministic non-linear least square approach developed by Sanford and Dally. They showed that the use of multi-parameter stress field equations allows the collection of data from a larger zone around the crack-tip which helps to simplify the data collection from experiments. Their study considered the influence of ten numbers of terms in the multi-parameter equation. Guagliano et al. [16] used the same methodology to analyze the effect of adding up to twenty terms in the multi-parameter equation while collecting the data from the isochromatic fringe pattern spread over a wider zone around the crack-tip.

### 1.2.2 Estimation of fracture parameters using digital image correlation (DIC)

DIC refers to the class of non-interferometric, non-contact optical methods of experimental stress analysis that acquire images of an object, store these images in digital form and perform image analysis to extract full-field shape and deformation measurement [17-18]. It directly provides information about the displacements and strains by comparing the digital images of the specimen surface in the un-deformed (or reference) and deformed states respectively. In principle, DIC is based on pattern matching and numerical computing [19]. In DIC, one of the most commonly used approaches employs random patterns and compares sub-regions (subsets) from 'deformed' and 'un-deformed' images to obtain a full-field of sensor-plane measurements [18].

The basic principle of 2D DIC is the matching of the small subsets between the digitized

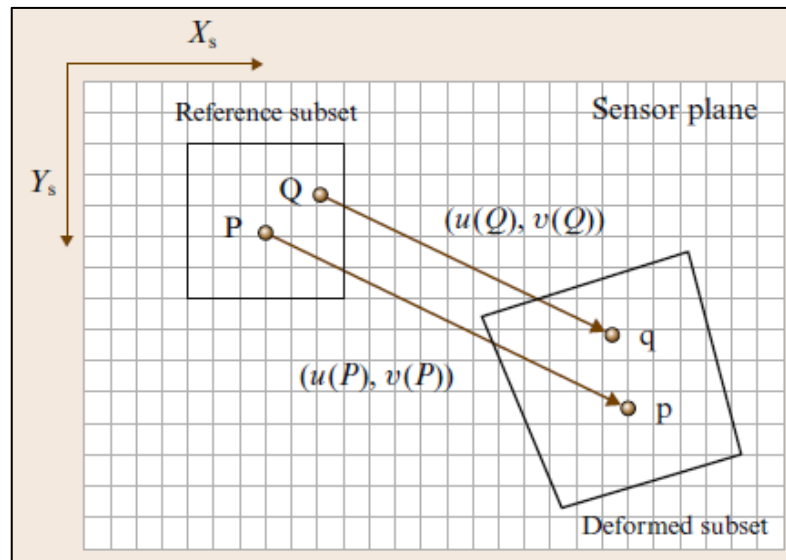


Fig. 1.5 Schematic of deformation process in two dimensions with subsets in deformed and un-deformed state [20]



images of the specimen surface recorded in un-deformed (reference) and deformed state as schematically illustrated in Fig. 1.5 [19]. The matching process is performed to locate the corresponding position of each reference subset within each deformed image [20]. In order to evaluate the degree of similarity between the subsets from reference image and the deformed image, a zero-normalized cross-correlation ( $C$ ) coefficient is used which is defined as [19]:

$$C(u,v) = \frac{\sum_{i=1}^m \sum_{j=1}^m [f(x_i, y_j) - \bar{f}] [g(x'_i, y'_j) - \bar{g}]}{\sqrt{\sum_{i=1}^m \sum_{j=1}^m [f(x_i, y_j) - \bar{f}]^2} \sqrt{\sum_{i=1}^m \sum_{j=1}^m [g(x'_i, y'_j) - \bar{g}]^2}} \quad (1.2)$$

Where,

$\bar{f}$  = mean intensity value of reference subset

$\bar{g}$  = mean intensity value of deformed subset

$$x' = x + u_0 + \frac{\partial u}{\partial x} dx + \frac{\partial u}{\partial y} dy \quad (1.3a)$$

$$y' = y + v_0 + \frac{\partial v}{\partial x} dx + \frac{\partial v}{\partial y} dy \quad (1.3b)$$

where,  $f(x, y)$  and  $g(x', y')$  represent the gray levels of reference and deformed images, respectively; and  $(x, y)$  and  $(x', y')$  are the co-ordinates of a point in the subset before and after deformation respectively. Once the maximum of this correlation coefficient is detected, the position of the deformed subset is determined. Then, in-plane displacement vector at point P can be calculated using the difference in the positions of the reference subset center and the deformed subset center [19].

Two-dimensional (2D) DIC uses a single imaging camera, the sensor plane of which is kept parallel to the surface of planar object. However, 2D-DIC is applicable only for planar objects that exhibit little or no out-of-plane displacement and cases where the recording camera can be set perpendicular to the object surface [18]. In actual practice, it may not be possible to avoid the out-of-plane deformation (e.g. crack-tip analysis). To overcome this fundamental limitation, three-dimensional (3D) DIC method is developed which uses a stereo vision system employing two or more cameras to accurately measure the full three-dimensional shape and deformation of a curved or planar object, even when the object undergoes large out-of-plane rotation and displacement [18-20]. Figure 1.6 shows the whole field  $u$  and  $v$  displacement for single edge notched (SEN) specimen.

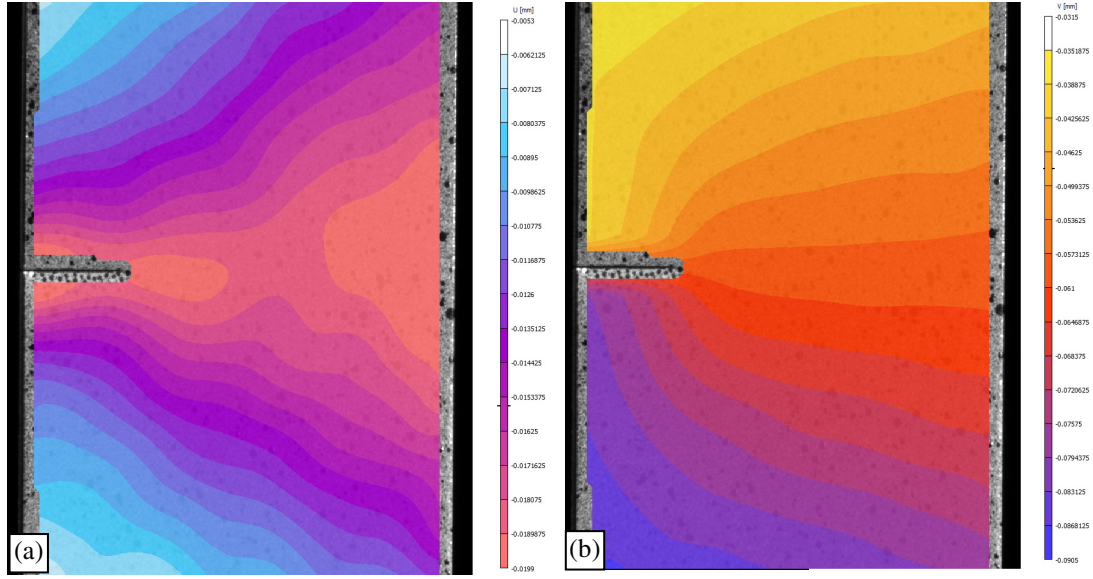


Fig. 1.6 (a)  $u$ -displacement contour map and (b)  $v$ -displacement contour map for SEN specimen obtained from 3D-DIC

Barker et al. [21] presented a general algorithm to determine mode-I fracture parameters ( $K_I$  and  $\sigma_{0x}$ ), in a linear least square sense, from full field displacement fringe patterns obtained using moiré or speckle interferometric technique. Using numerical experiments, they studied the sensitivity of the algorithm to the systematic position errors introduced due to incorrect location of the crack-tip. In order to minimize this error, they suggested method of assuming various crack-tip locations in the vicinity of actual crack-tip and then selecting best-fit results. Using linear least square method, McNeill et al. [22] determined the  $K_I$  from data points ( $r$ ,  $\theta$  and  $v$ ), collected over full field displacement field surrounding the crack-tip involving 2D-DIC technique. They used  $v$ -displacement field near the crack-tip and investigated the effect of using higher order terms on the evaluation of SIF. Sutton et al. [23] employed 2D-DIC to study the three-dimensional effects near the crack-tip. In order to reduce the effect of out-of-plane motion, an adjustable extension tube was added between the camera and lens. In order to reduce the experimental noise, they used smoothened  $u$ -displacement and  $v$ -displacement field obtained for SEN specimen to predict the presence of three-dimensional and/or non-linear zone near the crack-tip. Luo et al. [24] used 3D-DIC to evaluate the three-dimensional displacement field in the vicinity of the crack-tip for compact tension (CT) specimen. In their study, the symmetry of displacement field was used effectively to determine the rigid body rotation. Han et al. [25] studied the in-plane deformation near the stationary crack-tip for thin SEN specimen using 2D-DIC. Using the multi-parameter displacement field equations derived from William's eigen function approach, they obtained the values of  $K_I$  separately, from both  $u$ -displacement and  $v$ -

displacement field near the crack-tip which compare well with those obtained using finite element and boundary-point collocation method. A total of 10 to 15 terms were used to estimate  $K_I$  from large number of data points. Chao et al. [26] used in-plane displacements obtained from 2D-DIC to compute dynamic  $K_I$  and  $\sigma_{ox}$  in a linear least square sense using the asymptotic steady-state crack-tip field equations. However, all these studies were limited to mode-I crack problems. Luo and Huang [27] used full field in-plane displacement field, obtained with the help of 3D-DIC, to evaluate the mixed-mode SIF's for compact tension shear (CTS) specimen through a linear least square fit. Using both the radial and tangential displacement components ( $u_r$  and  $u_\theta$ ), derived from William's eigen function approach, they evaluated  $K_I$  and  $K_{II}$  as well as in-plane rigid body translation and rotation.

All the above mentioned methodologies either neglected the error introduced due to ambiguous location of the crack-tip or used trial and error technique to locate the crack-tip that minimizes this error [21-22]. Using the whole field displacement data ( $u$  and  $v$ ) obtained from 2D-DIC, Yoneyama et al. [28] employed a non-linear least square algorithm to estimate the mixed-mode SIF's ( $K_I$  and  $K_{II}$ ), rigid body displacement as well as the location of crack-tip. They used radial and tangential components of displacement ( $u_r$  and  $u_\theta$ ) derived from Atluri and Kobayashi's multi-parameter displacement field equations as a basis for their mathematical formulation. They treated the displacement components separately and compared the values of  $K_I$  and  $K_{II}$  obtained separately from whole field displacement components -  $u_r$ ,  $u_\theta$ ,  $u$  and  $v$ . They accounted for the effect of twenty terms and found that polar displacement components ( $u_r$  and  $u_\theta$ ) are better suited for determination of mixed mode fracture parameters as compared to Cartesian displacement components ( $u$ ,  $v$ ). Yoneyama et al. [29] extended the non-linear least square algorithm by using novel mathematical formulation that treats  $u$  and  $v$  displacement components in a combined way. They proposed new convergence criteria based on the correlation coefficient and the sum of absolute values of error between experimentally obtained and theoretically reconstructed displacement field. The algorithm is found to be effective even when the material exhibited small scale yielding. López-Crespo et al. [30] obtained the mixed-mode SIF's through a least square fit for a crack emanating from a fastener hole using displacement data obtained from 2D-DIC technique for various specimen configurations. They have used multi-parameter displacement field equations derived using Muskhelishvili's complex function analysis and considered the effect of twenty terms on SIF accuracy. In order to minimize the effect of error due to uncertainty in locating the crack-tip, crack tip coordinates were located automatically in the displacement images using the Sobel edge-finding algorithm. In their study, near-tip data was collected from the zone spread all around the crack-tip and the

different sources of errors (such as crack-tip plasticity, crack closure, crack curvature etc.) were predicted. Using the full field displacement data ( $u, v$ ) obtained using DIC, Zhang and Lingfeng [31] estimated the mixed mode SIF's through linear least square fit, the formulation of which was based on multi-parameter displacement field equations derived using William's Eigen function approach. In order to locate the crack-tip, they used trial and error technique in coarse-fine form which is based on the minimization of absolute value of error in the displacement field.

### **1.3 Scope and Motivation**

Estimation of mixed-mode SIF's using digital photoelasticity is established very well in the literature. However, all the present methods require manual data collection ( $r, \theta$  and  $N$ ) which is very cumbersome and may sometimes lead to human error. Thus, there exists a need to automate the data collection technique involving DIP technique for accurate SIF estimation. Off late lot of fracture study is carried out using DIC because if it is of greater accuracy and uses simple optics. Even specimen preparation is simpler. Determination of mixed-mode SIF's using DIC technique has got a lot of potential applications in varied areas like patch repair, material testing and inclusion problems. The same procedure can be easily adapted for fracture study in functionally graded and composite materials thereby increasing its range of application.

### **1.4 Thesis layout**

Chapter 1 mainly gives the idea about the estimation of fracture parameters using various methods, brief literature review of the evaluation of fracture parameters using digital photoelasticity and digital image correlation, scope and motivation for the thesis.

Chapter 2 deals with the determination of fracture parameters using digital photoelasticity. It describes the methodology, implementation, details of specimen preparation and experimentation. Also a comparative study between analytical, experimental and numerical SIF value is made.

Chapter 3 considers the estimation of fracture parameters using DIC. It describes the methodology, implementation, details of specimen preparation and experimental. Also a comparative study between analytical and experimental SIF value is made. The SIF's are compared against numerical value.

Chapter 4 comprises the conclusion and the recommendation for the future work.

# Chapter 2

## Photoelastic Determination of SIF's

### 2.1 Introduction

Photoelasticity is an amplitude division based interferometric technique of experimental stress analysis. Photoelasticity gives physical insight into the engineering design problem and can be used as an effective visualization tool. With the advent of PC-based digital image processing systems to obtain the intensity data, a quantitative and automatic estimation of the whole field photoelastic parameters has now become possible. Because of the advances in digital photoelasticity, photoelastic analysis has become more efficient and reliable technique for understanding the complex structural behavior (e.g. measurement of SIF's, Stress Concentration Factor (SCF), and contact stress parameters etc.). Photoelasticity has seen wide applications in the field of fracture mechanics, especially for the determining of fracture parameters.

This chapter focuses on the evaluation of mixed-mode SIF's using digital photoelasticity. Figure 2.1 summarizes the general steps involved in the evaluation of fracture parameters using digital photoelasticity. It also shows the different algorithms/software used for various purposes in the present work (written outside the box). SIF's are estimated for two different configurations - Single edge notched (SEN) panel and interacting parallel edge cracked panel. Ten-step method has been used for the accurate evaluation of total isochromatic fringe order over the entire model domain. In order to avoid any human error in data collection, automatic data collection has been employed. SIF's are estimated using the multi-point over-deterministic nonlinear least square technique. The experimentally evaluated SIF's are compared with the analytical as well as finite element (FE) estimates. In case of interacting parallel edge cracked panel, the isochromatic fringe pattern in the vicinity of both the crack-tips reveals some of the key features of the interaction of stress fields surrounding the two parallel edge crack tips. The study emphasizes the fact that analytical and FEM fail to give such a physical understanding of the complex structural



phenomena. The details regarding the specimen preparation, experimental procedure and implementation of the nonlinear least square technique are also given.

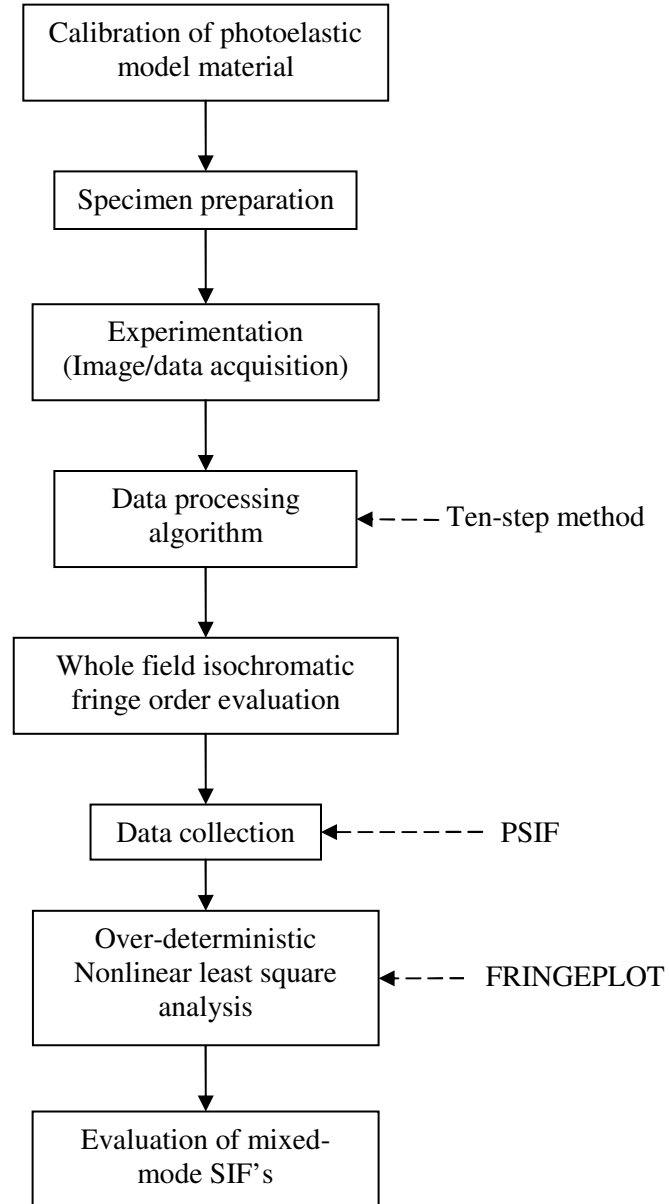


Fig. 2.1 General steps involved in the photoelastic determination of mixed-mode SIF's

## 2.2 Multi-parameter stress field equations

Many researchers [12-16] have emphasized the need of using multi-parameter stress field equations while evaluating the mixed-mode SIF's using digital photoelasticity. This need stems from the practical limitations on the zone of data ( $r$ ,  $\theta$  and  $N$ ) collection due to the following reasons:

### 2.2.1 Tri-axial state of stress

It has been established [11, 15, 32-34] that there exists a three-dimensional state of stress in the close vicinity of the crack-tip and a plane stress assumption is no more valid in this region. Also, the experimental observations are affected by the high gradient of stresses present in this zone.

### 2.2.2 Finite slit-tip radius

The influence of finite tip radius of the artificial notch/slit used in the photoelastic studies to simulate the natural crack has been studied by different researchers [32-34]. It has been shown that the effect of finite slit-tip radius is very high in its close vicinity and this effect becomes minimal as one move away from slit-tip.

### 2.2.3 Stress-singularity

Due to presence of very high stress-concentration, the isochromatic fringe order in the close vicinity of the crack-tip may exceed the linear limit in the stress-fringe curve of the photoelastic material [32].

### 2.2.4 Localized crack-tip blunting

The presence of non-linear zone has been predicted [33] in the close vicinity of the crack-tip due to finite rotations associated with the crack-tip blunting. Because of this, stress field gets altered [15].

### 2.2.5 Plastic zone ahead of the crack-tip

It is well known fact that there is a formation of plastic zone in the close vicinity of the crack-tip and linear elastic fracture mechanics (LEFM) assumptions are not valid in this region close to the crack-tip.

Because of the above mentioned reasons, the zone of data collection cannot be confined to near-tip region and data has to be collected from the larger zone. Ramesh et al. [15] have shown the significance of using the multi-parameter stress field equations proposed by Atluri and Kobayashi in evaluating the fracture parameters by employing non-linear least squares approach from the isochromatic fringe field. Two-dimensional stress field equations introduced by Atluri and Kobayashi, [15, 35] for the general mixed-mode case, are given below and the same have been used in the present work.

$$\begin{Bmatrix} \sigma_x \\ \sigma_y \\ \tau_{xy} \end{Bmatrix} = \sum_{n=1}^{\infty} \frac{n}{2} A_n r^{\frac{n-2}{2}} \begin{Bmatrix} \left\{ 2 + (-1)^n + \frac{n}{2} \right\} \cos\left(\frac{n}{2}-1\right)\theta - \left(\frac{n}{2}-1\right) \cos\left(\frac{n}{2}-3\right)\theta \\ \left\{ 2 - (-1)^n - \frac{n}{2} \right\} \cos\left(\frac{n}{2}-1\right)\theta + \left(\frac{n}{2}-1\right) \cos\left(\frac{n}{2}-3\right)\theta \\ - \left\{ (-1)^n + \frac{n}{2} \right\} \sin\left(\frac{n}{2}-1\right)\theta + \left(\frac{n}{2}-1\right) \sin\left(\frac{n}{2}-3\right)\theta \end{Bmatrix}$$

$$-\sum_{n=1}^{\infty} \frac{n}{2} A_{\text{IIn}} r^{\frac{n-2}{2}} \left\{ \begin{aligned} &\left\{ 2 - (-1)^n + \frac{n}{2} \right\} \sin\left(\frac{n-1}{2}\right) \theta - \left(\frac{n}{2} - 1\right) \sin\left(\frac{n-3}{2}\right) \theta \\ &\left\{ 2 + (-1)^n - \frac{n}{2} \right\} \sin\left(\frac{n-1}{2}\right) \theta + \left(\frac{n}{2} - 1\right) \sin\left(\frac{n-3}{2}\right) \theta \\ &-\left\{ (-1)^n - \frac{n}{2} \right\} \cos\left(\frac{n-1}{2}\right) \theta - \left(\frac{n}{2} - 1\right) \cos\left(\frac{n-3}{2}\right) \theta \end{aligned} \right\} \quad (2.1)$$

Where,  $A_{\text{I1}} = K_{\text{I}} / \sqrt{2\pi}$  and  $A_{\text{II1}} = -K_{\text{II}} / \sqrt{2\pi}$  and  $4A_{\text{I2}} = -\sigma_{0x}$ . In Eq. (2.1), polar co-ordinates are measured from the crack tip as shown in Fig.1.1.

### 2.3 Digital photoelastic parameter estimation using Ten-step method

To evaluate mixed-mode SIF's using digital photoelasticity, it is of great importance to obtain the total isochromatic fringe order information around the crack tip. Phase shifting techniques are one of the widely used methodologies for quantitative extraction of isochromatic and isoclinic parameter at every point (pixel) in the domain. In phase shifting techniques, specific phase shifts are introduced between the recorded images for a given experimental situation using specific arrangement of the optical elements [35]. Ten-step method [36] is one of such phase shifting techniques. Recently, Ramji and Prasath [37] recommended the use of ten-step phase shifting method for manual polariscope for digital photoelastic applications. It has been found that ten-step method gives both isoclinic and isochromatic parameter with greater accuracy as compared to other phase shifting methods even in the presence of the various sources of error [37]. Hence, in the present study, ten-step method is used. The optical arrangements of the ten-step method [36] are shown in Table 2.1. The first four steps correspond to the plane polariscope setup and the next six arrangements are based on the circular polariscope setup. For isoclinic parameter estimation,  $\theta_c$  is to be evaluated by atan2() function. The isoclinic values thus obtained are then unwrapped and further used for isochromatic evaluation.

$$\theta_c = \frac{1}{4} \tan^{-1} \left( \frac{I_4 - I_2}{I_3 - I_1} \right) = \frac{1}{4} \tan^{-1} \left( \frac{\sin 4\theta \sin^2 \frac{\delta}{2}}{\cos 4\theta \sin^2 \frac{\delta}{2}} \right), \quad \text{for } \sin^2 \frac{\delta}{2} \neq 0 \quad (2.2)$$

$$\delta_c = \tan^{-1} \left( \frac{(I_9 - I_7) \sin 2\theta + (I_8 - I_{10}) \cos 2\theta}{I_5 - I_6} \right). \quad (2.3)$$

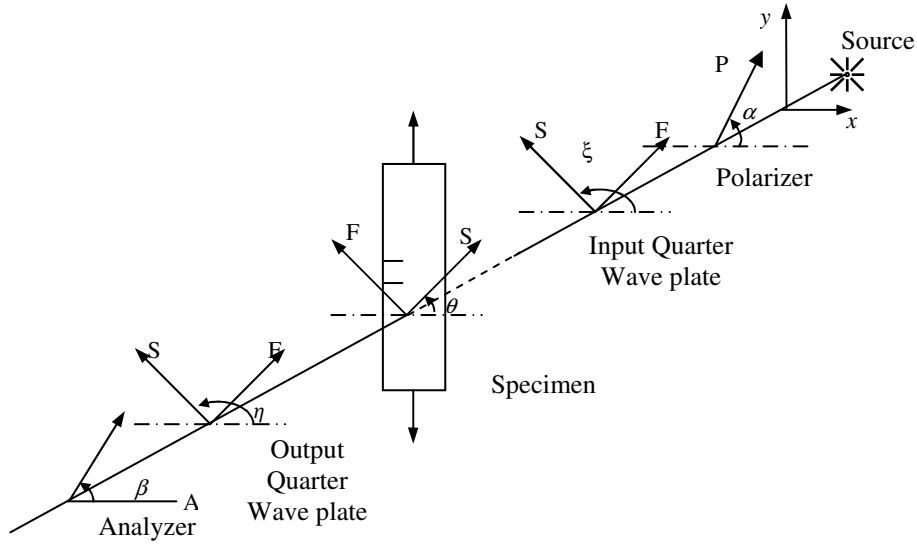


Fig. 2.2 Generic arrangement of a circular polariscope set-up

Table 2.1 Optical arrangements for Ten-step phase shifting technique

$\alpha$	$\xi$	$\eta$	$\beta$	Intensity equation
$\pi/2$	-	-	0	$I_1 = I_b + I_a \sin^2 \frac{\delta}{2} \sin^2 2\theta$
$5\pi/8$	-	-	$\pi/8$	$I_2 = I_b + \frac{I_a}{2} \sin^2 \frac{\delta}{2} [1 - \sin 4\theta]$
$3\pi/4$	-	-	$\pi/4$	$I_3 = I_b + I_a \sin^2 \frac{\delta}{2} \cos^2 2\theta$
$7\pi/8$	-	-	$3\pi/8$	$I_4 = I_b + \frac{I_a}{2} \sin^2 \frac{\delta}{2} [1 + \sin 4\theta]$
$\pi/2$	$3\pi/4$	$\pi/4$	$\pi/2$	$I_5 = I_b + \frac{I_a}{2} (1 + \cos \delta)$
$\pi/2$	$3\pi/4$	$\pi/4$	0	$I_6 = I_b + \frac{I_a}{2} (1 - \cos \delta)$
$\pi/2$	$3\pi/4$	0	0	$I_7 = I_b + \frac{I_a}{2} (1 - \sin 2\theta \sin \delta)$
$\pi/2$	$3\pi/4$	$\pi/4$	$\pi/4$	$I_8 = I_b + \frac{I_a}{2} (1 + \cos 2\theta \sin \delta)$
$\pi/2$	$\pi/4$	0	0	$I_9 = I_b + \frac{I_a}{2} (1 + \sin 2\theta \sin \delta)$
$\pi/2$	$\pi/4$	$3\pi/4$	$\pi/4$	$I_{10} = I_b + \frac{I_a}{2} (1 - \cos 2\theta \sin \delta)$

By using Eq. (2.2), isoclinic phase map is obtained and it has to be unwrapped by adaptive quality guided approach to remove the inconsistent zone [38]. The unwrapped isoclinic

values are then used to obtain isochromatic phase map thereby avoiding any ambiguous zones using Eq. (2.3). Later, the isochromatic phase map is unwrapped to get the whole field fringe order. This continuous fringe order information will be the input for SIF estimation using over-deterministic non-linear least square technique.

## 2.4 Over-deterministic Non-linear Least Square Methodology

The details of the methodology can be found in Ref. [15, 35] and are summarized here for completeness.

### 2.4.1 Formulation of equations

Stress optic law is given by,

$$\sigma_1 - \sigma_2 = \frac{NF_\sigma}{h} \quad (2.4a)$$

where,  $F_\sigma$  = material stress-fringe value and  $h$  = model thickness

$$\sigma_1, \sigma_2 = \frac{\sigma_x + \sigma_y}{2} \pm \sqrt{\frac{(\sigma_x - \sigma_y)^2}{4} + (\tau_{xy})^2} \quad (2.4b)$$

$$\text{The error function can be defined as: } g_m = \left\{ \frac{\sigma_x - \sigma_y}{2} \right\}^2 + (\tau_{xy})^2 - \left\{ \frac{NF_\sigma}{2h} \right\}^2 \quad (2.4c)$$

Applying Taylor series expansion,

$$(g_m)_{i+1} = (g_m)_i + \frac{\partial g}{\partial A_{I1}}(\Delta A_{I1}) + \frac{\partial g}{\partial A_{I2}}(\Delta A_{I2}) + \dots + \frac{\partial g}{\partial A_{Ik}}(\Delta A_{Ik}) + \frac{\partial g}{\partial A_{I11}}(\Delta A_{I11}) + \frac{\partial g}{\partial A_{I12}}(\Delta A_{I12}) + \dots + \frac{\partial g}{\partial A_{I1n}}(\Delta A_{I1n})$$

where,  $i = i^{th}$  iteration step and  $\Delta A$  is incremental value to be added to the previous estimate of  $A$

To determine the corrections,  $(g_m)_{i+1} = 0$

$$-(g_m)_i = \frac{\partial g}{\partial A_{I1}}(\Delta A_{I1}) + \frac{\partial g}{\partial A_{I2}}(\Delta A_{I2}) + \dots + \frac{\partial g}{\partial A_{Ik}}(\Delta A_{Ik}) + \frac{\partial g}{\partial A_{I11}}(\Delta A_{I11}) + \frac{\partial g}{\partial A_{I12}}(\Delta A_{I12}) + \dots + \frac{\partial g}{\partial A_{I1n}}(\Delta A_{I1n})$$

Rearranging in matrix form,

$$\begin{aligned} \{g\}_i &= -[b]_i \{\Delta A\}_i \\ \{\Delta A\}_i &= -[c]_i^{-1} \{d\}_i \end{aligned} \quad (2.5)$$

Where,  $[c]_i = [b]_i^T [b]_i$  and  $\{d\}_i = [b]_i^T \{g\}_i$

$$\{A\}_{i+1} = \{A\}_i + \{\Delta A\}_i$$

### 2.4.2 Convergence criteria

The above equations are solved using Newton-Raphson scheme in an iterative manner. The iterations are stopped using the fringe order error minimization criteria. The fringe order error is defined as:

$$\frac{\sum |N_{theory} - N_{exp}|}{\text{total no. of data points}} \leq \text{convergence error} \quad (2.6)$$

where,  $N_{theory}$  and  $N_{exp}$  correspond to recalculated and experimental values of fringe order. The solution for a given number of parameters is considered as acceptable when the convergence error is of the order of 0.05 to 0.1 and the iterations are stopped.

### **2.4.3 Implementation**

Since the number of parameters required for modeling the stress field is not known a priori, the iteration is started with minimum number of parameters in the stress field equations. The isochromatic fringe pattern is reconstructed at every stage using the obtained parameters for cross-verification with experimental fringe pattern. For the comparison between the theoretically reconstructed and experimentally obtained fringe field, the data points are echoed back. If the converged solution does not model the stress field correctly, then by using the solution of the parameters thus obtained as starting values, the number of parameters is increased by one. The process is continued until a good match is obtained between the theoretically reconstructed and experimentally obtained fringe contours.

## **2.5 Experimental Validation**

### **2.5.1 Specimen preparation**

As mentioned in section 2.1, two types of specimens are considered in the present study, namely - Single edge notched (SEN) panel and interacting parallel edge cracked panel. Experiments are conducted on the test specimens, cut from an epoxy sheet casted in house by mixing commercially available C-51 epoxy resin and K-6 hardener in the proportion of 10:1 by weight. The mixture is mixed at room temperature for about 30 minutes with due precaution taken to avoid the formation of any air bubbles. The resin-hardener mixture is then poured into the mold and left to cure for 24 hours at room temperature. The casted epoxy sheets are then checked in polariscope for the presence of any residual stresses. The specimens of the size of 40 mm × 210 mm are then milled from 6 mm thick casted sheet. During the machining, precaution is taken to avoid high cutting forces and excessive amount of heat generation. As it is not possible to pre-crack the epoxy specimens using fatigue loading due to very high brittle nature of epoxy, thin slits of thickness 0.3 mm are cut with the help of grinded hacksaw blades to simulate the real cracks. In order to reduce the effect of finite width and tip radius of the slit, the ends of the slits are extended with the help of toothed razor blade (thickness  $\approx$  0.1 mm) by an amount of 0.1 to 0.5 mm. (See Fig. 2.3) The SEN specimen contains a straight crack of length 10 mm as shown in Fig. 2.4(a), while the interacting parallel edge cracked specimen contains two straight cracks, each of length 8 mm, separated by the distance of 10 mm and located symmetrically with respect to

loading as shown in Fig. 2.4(b). In case of both test specimens, the crack is oriented in a direction normal to the loading direction.

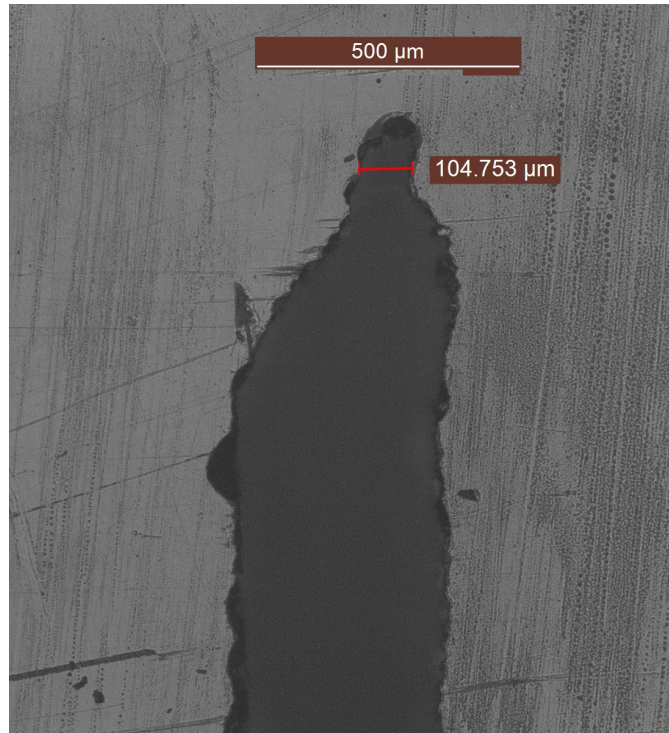


Fig. 2.3 Optical microscope image of notched epoxy specimen showing the details of the slit-tip

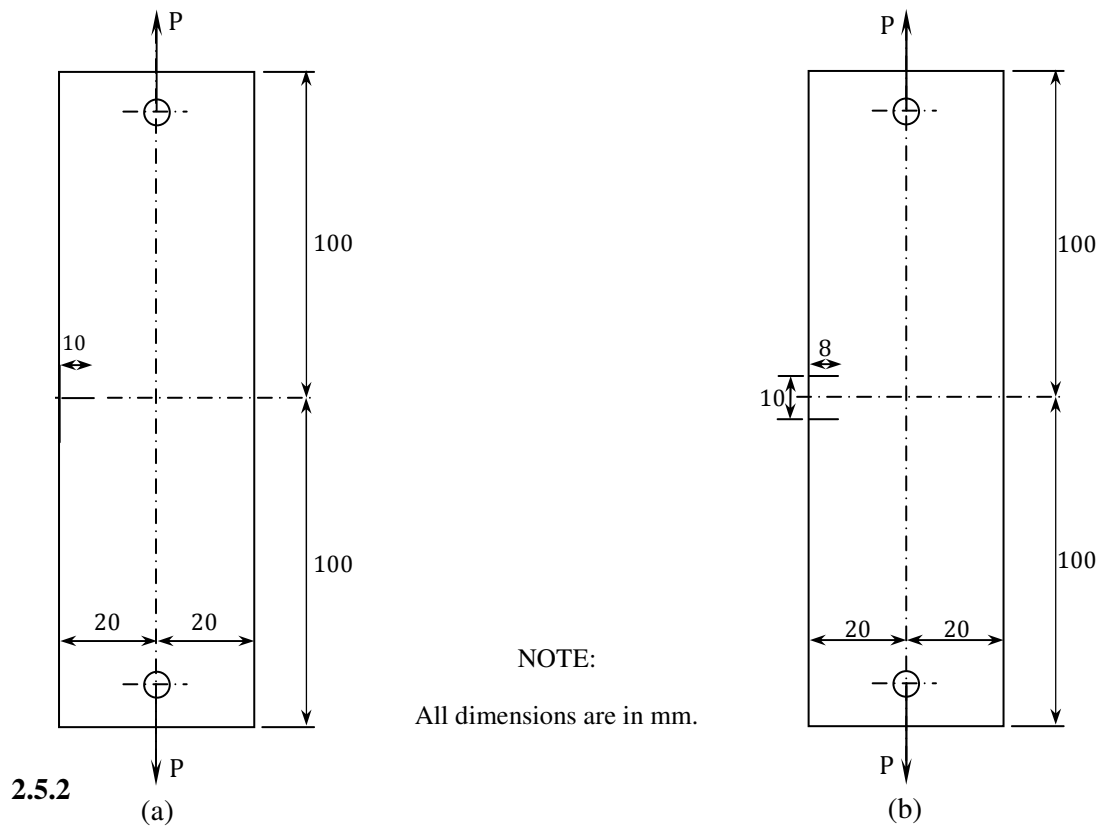


Fig. 2.4 Specimen geometry for (a) SEN panel, (b) Interacting parallel edge cracked panel

## Experimental procedure

Figure 2.5 shows the experimental setup for digital photoelasticity used in the current study. Transmission photoelasticity experiments are conducted on the epoxy test specimens. The loading frame arrangement uses dead weights for applying uniaxial tensile load on the specimens along their longitudinal direction. Digitized images of the epoxy test specimen subjected to uniaxial tensile load are recorded using CCD camera for different optical arrangements as shown in Table 2.1. Material stress fringe value for the epoxy specimen ( $F_\sigma$ ) is 12 N/mm/fringe. Monochromatic light source of wavelength of 589 nm is used in the experiment. The images are recorded using BASLER monochrome CCD camera that has a spatial resolution of  $1392 \times 1040$  pixels and it digitizes the image at video rate. The zoomed up portion of the crack tips are recorded in the image. Fig. 2.6 shows the dark field isochromatics obtained for SEN specimen and interacting parallel edge cracked specimen. For SEN panel, load of 577.4 N is applied and for interacting parallel edge cracked panel, load of 641.6 N is applied on to the specimen.

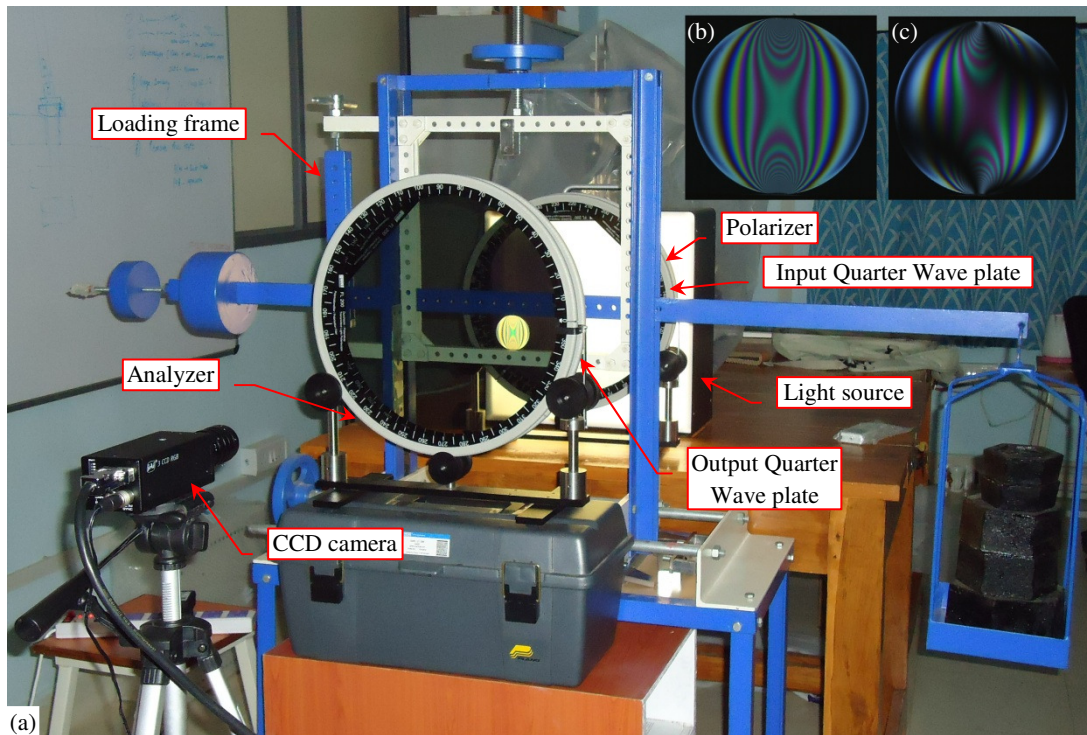


Fig. 2.5 (a) Experimental setup for digital photoelasticity, (b) Image recorded in a circular polariscope showing isochromatics, (c) Image recorded in a plane polariscope showing isochromatics as well as isoclinics



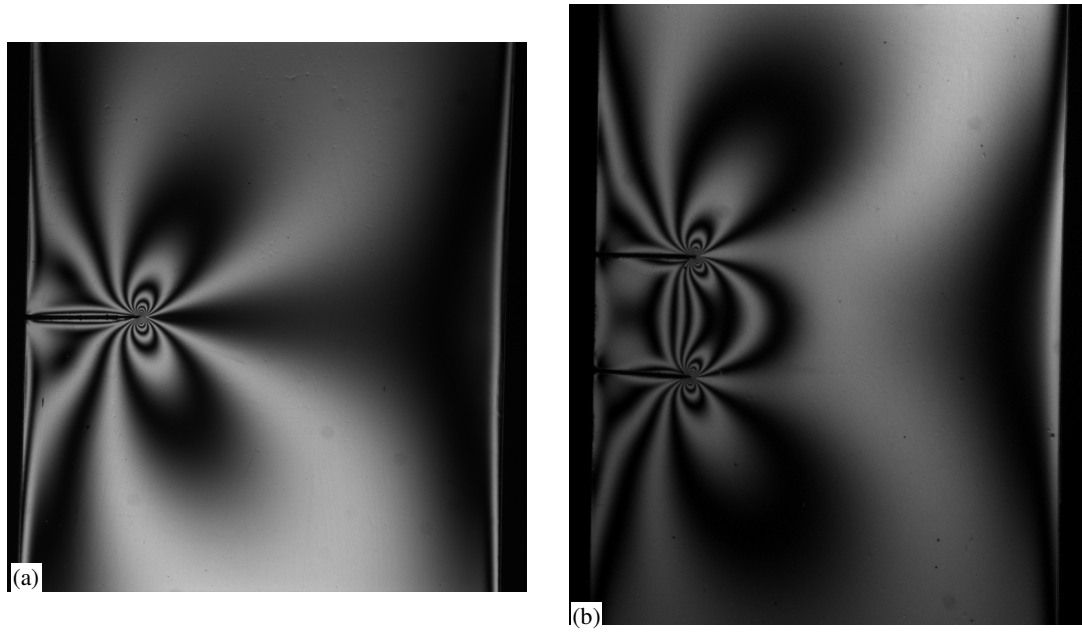


Fig. 2.6 Dark field isochromatic fringe pattern for (a) SEN specimen, (b) Interacting parallel edge cracked specimen

### 2.5.3 Photoelastic analysis

Figure 2.7 shows the full field isochromatic and isoclinic phase map for the SEN specimen subjected to uniaxial tensile load. Figure 2.7 (a) shows the wrapped isoclinic phase map and the unwrapped isoclinic phase map is shown in Fig. 2.7 (b). The unwrapped isoclinic is used to get the isochromatic phase map without any ambiguity and is shown in Fig. 2.7 (c). The wrapped isochromatic phase map need to be unwrapped to get the total fringe order over the model domain and the unwrapped isochromatic phase map is shown in Fig. 2.7 (d) as a MATLAB plot. Similarly, Fig. 2.8 shows the full field isochromatic and isoclinic phase map for the parallel edge cracked specimen subjected to uniaxial tensile load. Figure 2.8(a) shows the wrapped isoclinic phase map and, the unwrapped isoclinic phase map is shown in Fig. 2.8(b). The unwrapped isoclinic is used to get the isochromatic phase map which is shown in Fig. 2.8 (c). The wrapped isochromatic phase map needs to be unwrapped to get the total fringe order over the model domain and the unwrapped isochromatic phase map is shown in Fig. 2.8(d) as gray scale plot and the MATLAB plot of the same is shown in Fig. 2.8 (e). An over-deterministic least squares procedure [8, 15] is then invoked using FRINGE PLOT [39] to evaluate the multiple parameters governing the stress field. Although data can be collected anywhere from the fringe field, for easy convergence, it has been reported [15] that the fringe order and the corresponding positional coordinates need to be collected such that, when plotted, they capture the basic geometric features of the fringe field near the crack tip.

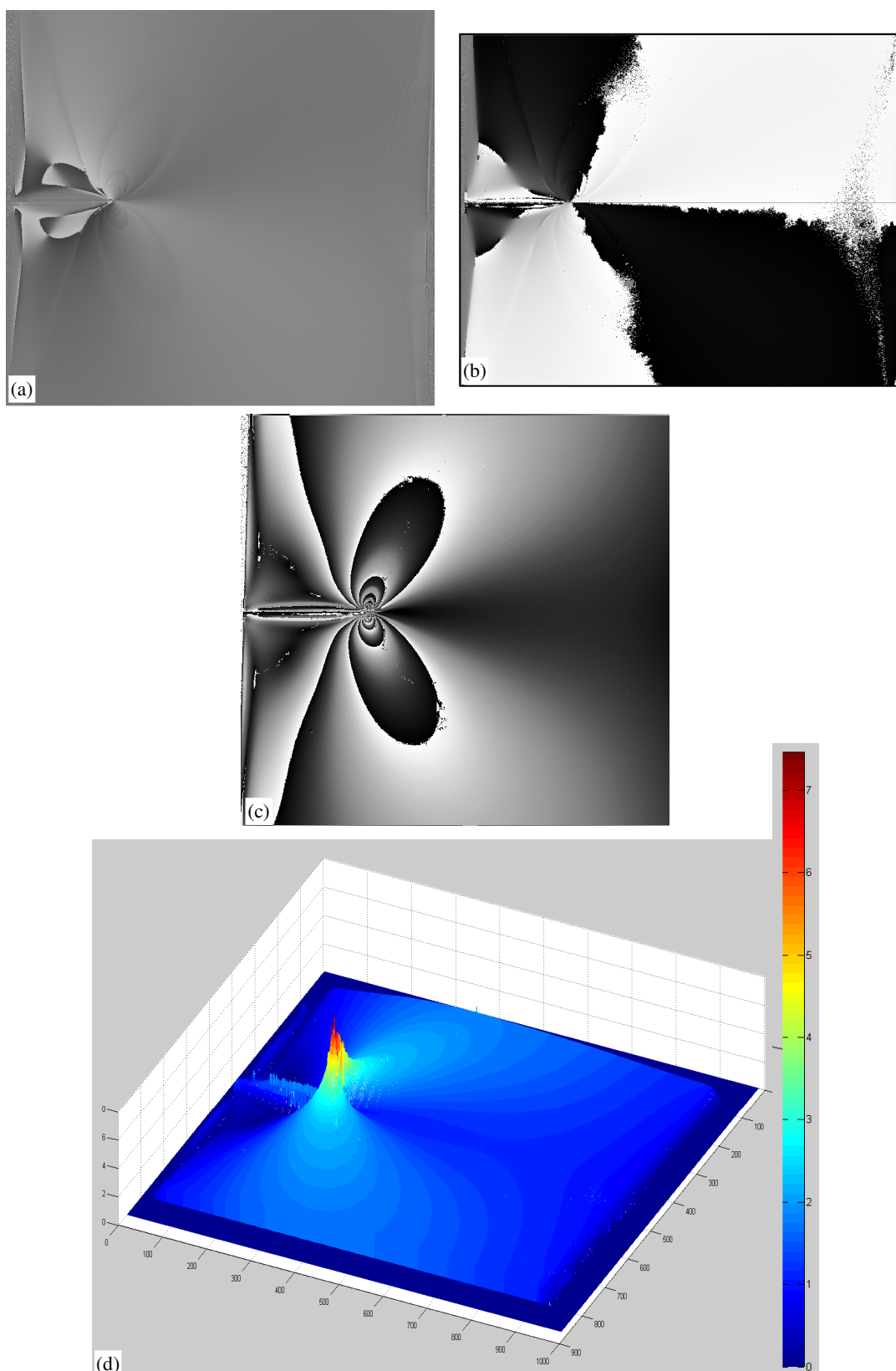
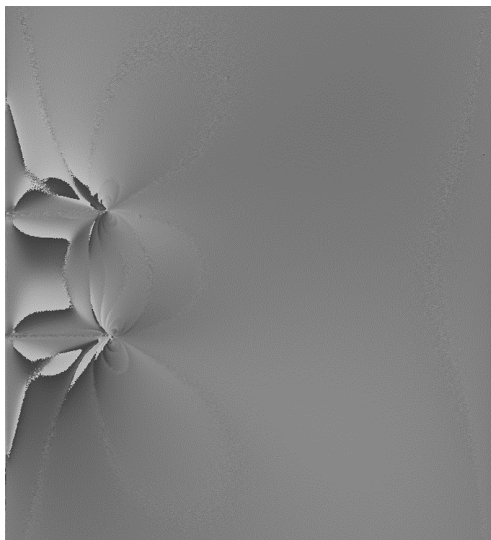
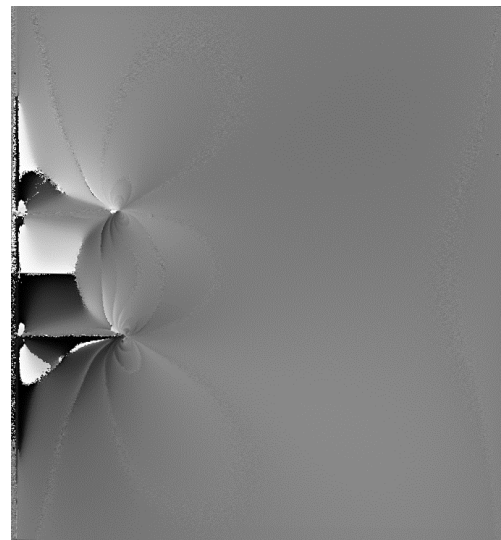


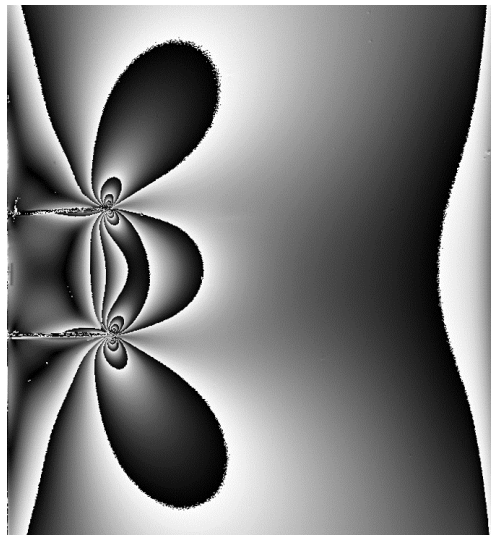
Fig. 2.7 Full field phase map obtained using ten-step method (a) wrapped isoclinic phase map  
 (b) unwrapped isoclinic phase map (c) isochromatic phase map  
 (d) MATLAB plot for unwrapped isochromatic phase map



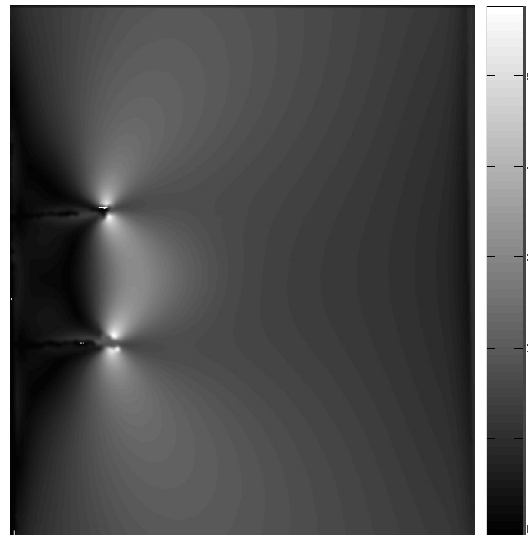
(a)



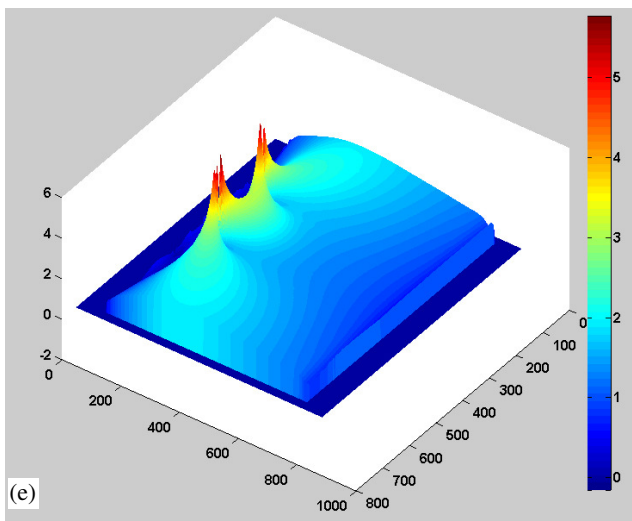
(b)



(c)

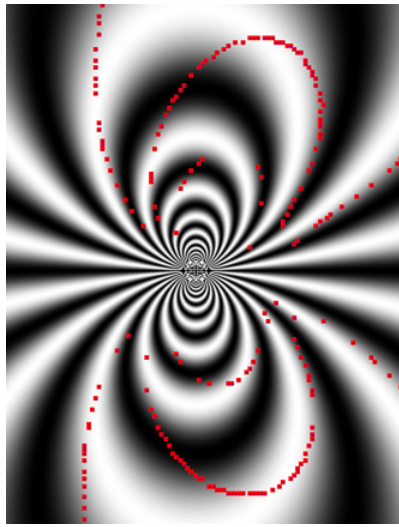


(d)

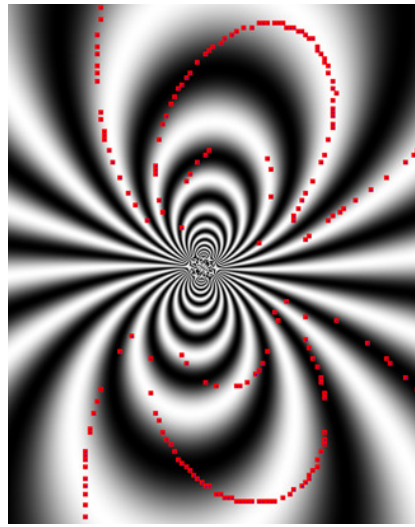


(e)

Fig. 2.8 Full field phase map obtained using ten-step method for interacting parallel edge cracked specimen  
(a) wrapped isoclinic phase map  
(b) unwrapped isoclinic phase map  
(c) isochromatic phase map  
(d) gray scale plot for unwrapped isochromatic phase map  
(e) MATLAB plot



One parameter



Two parameters



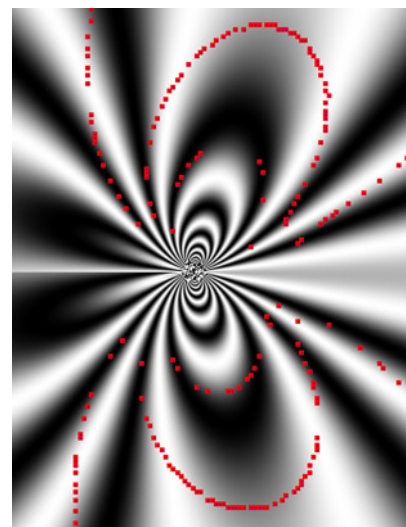
Three parameters



Four parameters



Five parameters



Six parameters

Fig. 2.9 Reconstructed dark field fringe contours for SEN specimen obtained using various parameters

As data needs to be collected nearer to crack tip for each load step, manual data collection along the thinned fringe skeletons would not only be erroneous but also it is tedious as well. Hence, automated data collection is implemented. The automated data collection software PSIF [39] developed in house using VC++ has an interactive module to remove outliers. The fringe orders and coordinates defining the positions of various data points surrounding crack tip are selected automatically in the range  $0.0625 < r/a < 0.375$  and they are used for SIF evaluation using the method of least squares. Total 345 and 393 data points are collected for SEN specimen and interacting parallel edge cracked specimen respectively. For SEN specimen, seven-parameter solution is found to be suitable with the convergence error of 0.112, while for interacting parallel edge cracked specimen, twelve-parameter solution is found to model the stress field in a better way with the convergence error of 0.056. Figure 2.10 (a) shows an experimentally obtained isochromatic fringe pattern for SEN specimen in dark field arrangement. Figure 2.10 (b) shows the magnified image of theoretically reconstructed dark field isochromatic fringe pattern around the crack obtained for SEN specimen using an seven-parameter solution with data points echoed back (indicated by red colored marker dots). Figure 2.11 (a) shows an experimentally obtained dark field isochromatic fringe pattern for interacting parallel edge cracked specimen while Fig. 2.11 (b) shows the magnified image of theoretically reconstructed dark field isochromatic fringe pattern around the bottom crack of interacting parallel edge cracked specimen obtained using a twelve-parameter solution with data points superimposed.

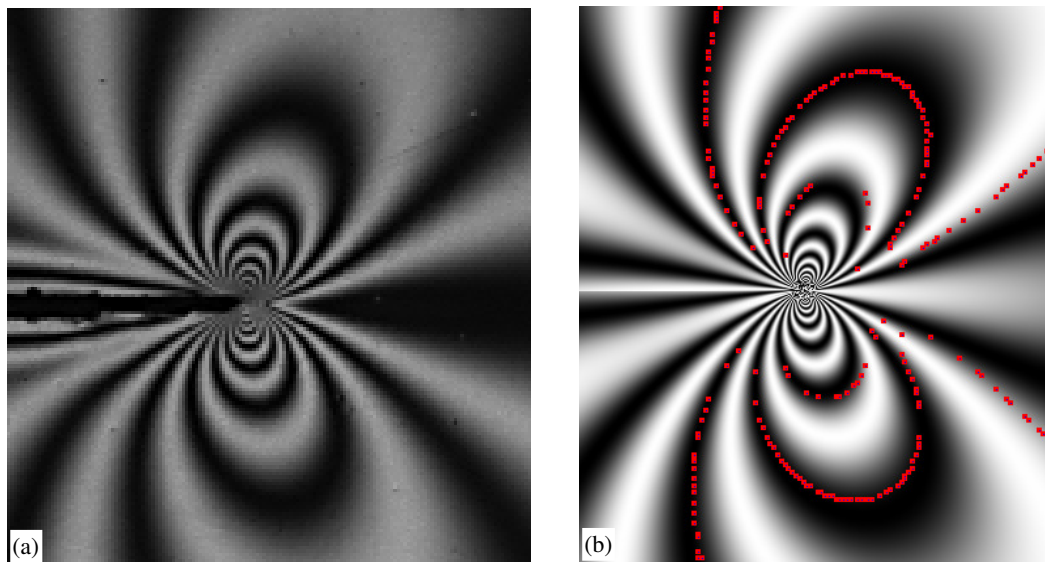


Fig. 2.10 Comparison of dark field image for SEN specimen (a) Experimentally obtained dark field isochromatic fringe pattern, (b) Theoretically reconstructed dark field isochromatic fringe contours with data points (shown by red colored dots)



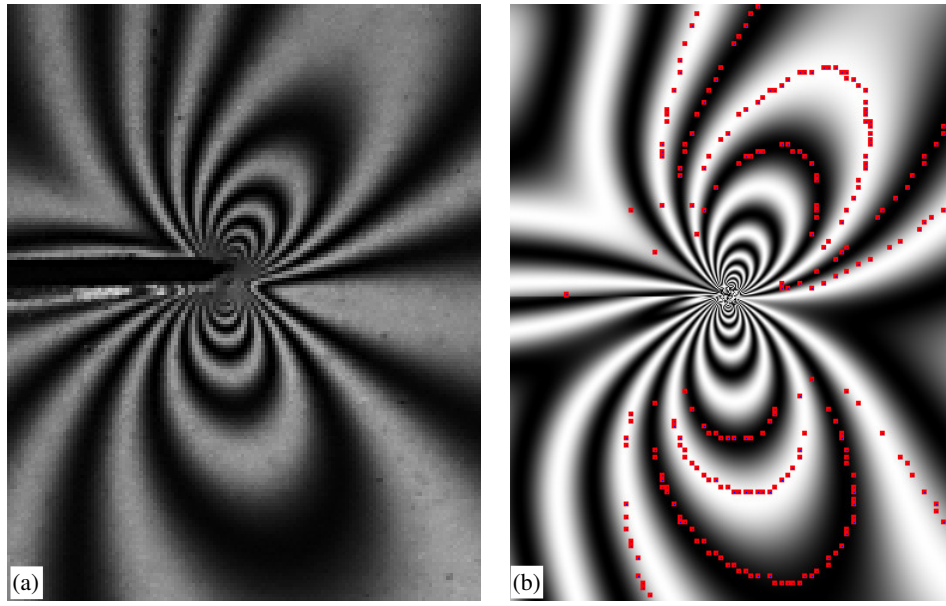


Fig. 2.11 Comparison of dark field image for interacting parallel edge cracked specimen  
(a) Experimentally obtained dark field isochromatic fringe pattern (b) Theoretically reconstructed dark field isochromatic fringe contours with data points (shown by red colored dots)

Table 2.2 shows the values of mixed-mode parameters obtained for SEN specimen. Table 2.3 shows the values of mode I and mode II parameters that are obtained for interacting parallel edge cracked specimen.

Table 2.2 Parameters obtained for SEN specimen

Mode I parameters	Mode II parameters
$A_{I1} = 7.331966$	$A_{II1} = -0.163132$
$A_{I2} = -0.828656$	$A_{II2} = 0.000000$
$A_{I3} = 0.294120$	$A_{II3} = -0.007503$
$A_{I4} = -0.015597$	----

Table 2.3 Parameters obtained for interacting parallel edge cracked specimen

Mode I parameters	Mode II parameters
$A_{I1} = 5.977325$	$A_{II1} = -0.864861$
$A_{I2} = -1.210526$	$A_{II2} = 0.000000$
$A_{I3} = 0.284130$	$A_{II3} = -0.127176$
$A_{I4} = 0.065423$	$A_{II4} = 0.128939$
$A_{I5} = -0.085857$	$A_{II5} = -0.015556$
$A_{I6} = 0.011058$	$A_{II6} = 0.008839$

## 2.6 Numerical computation of SIF's

To begin with, the problem of interacting parallel edge cracks subjected to uniaxial tensile load is considered as a mixed mode problem while SEN specimen under uniaxial tensile load is a pure mode-I problem. Thus, one has to obtain both the SIF's ( $K_I$  and  $K_{II}$ ) characterizing the stress field around crack tip for interacting parallel edge cracked panel. Although numerical computation of SIF's is straight forward, finite element analysis with conventional elements near the crack tip often underestimate the intense stress-displacement gradients [40]. Hence, computation of SIF's using FEA requires either a fine mesh around the crack tip or the use of 'special elements' with embedded stress singularity near the crack tip. There are several popular approaches for evaluating the fracture parameters ( $K_I$  and  $K_{II}$ ) numerically. In the present work, SIF's have been computed using J-integral approach as well as direct approach. During this estimation, linear elastic fracture mechanics (LEFM) behavior has been assumed for simplicity. The J-integral definition [41] considers a balance of mechanical energy for a translation in front of the crack along the  $x$ -axis, which is path independent contour integral defined as

$$\oint_C \left( W n_1 - \sigma_{ij} n_j \frac{\partial u_i}{\partial x} \right) ds \quad (2.7)$$

where,  $W$  is strain energy density;  $\sigma_{ij}$  are stress components;  $u_i$  are the displacements corresponding to local  $i$ -axis;  $s$  is the arc length of the contour;  $n_j$  is the  $j^{\text{th}}$  component of the unit vector outward normal to the contour  $C$ , which is any path of vanishing radius surrounding the crack tip.

The mixed-mode  $J$ -integral value is obtained from ANSYS directly by domain integral method [42]. Using the assumption of linear elastic fracture mechanics,  $K_I$  and  $K_{II}$  are related to the  $J$ -integral as shown below:

$$J = K_I^2 / E' + K_{II}^2 / E' \quad (2.8)$$

where,  $E'$  is modulus of elasticity,  $E' = E$  for plane stress conditions and  $E' = E / (1 - \nu^2)$  for plane strain conditions,  $\nu$  is Poisson's ratio. In order to determine  $K_I$  and  $K_{II}$ , the ratio of  $K_I$  over  $K_{II}$  is obtained from the ratio of the normal distance to the horizontal distance of two closest nodes to the crack-tips which they have been coincided before loading (see Ref. 43, 44) as shown in Fig. 2.12. SIF's can be evaluated directly from ANSYS (KCALC command) which uses a fit of the nodal displacements in the vicinity of the crack tip [45]. For this purpose, quarter-point (singular) elements have been used for meshing the region adjacent to the crack tip. Finite element analysis is carried out using ANSYS 12.1. Figure 2.13 (a) shows the FE mesh and symmetric boundary conditions used for modeling SEN

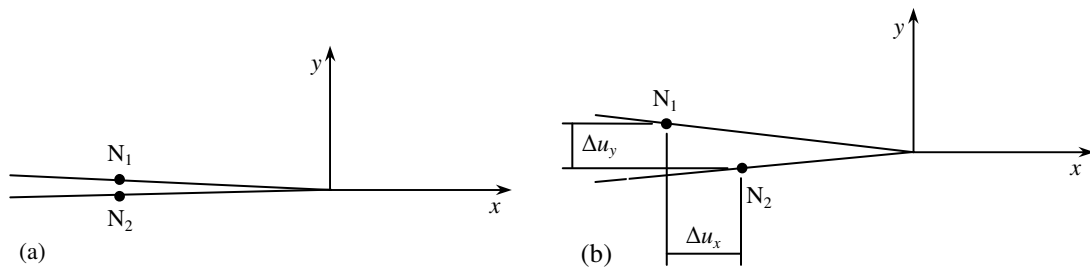


Fig. 2.12 (a) Two coincident nodes near the crack tip before loading (b) Two nearest nodes near the crack tip after loading

specimen subjected to uniform tensile load of 2.406 MPa. Figure 2.11(b) shows the meshing around the crack tip. Figure 2.14(a) shows the FE model and symmetric boundary conditions used for parallel edge cracked panel subjected to uniform tensile load of 2.67 MPa. Figure 2.14(b) shows the meshing around the crack tip. In both FE models, 8-noded quadrilateral element (PLANE183) is used and element size at the crack tip is kept as 0.001 mm.

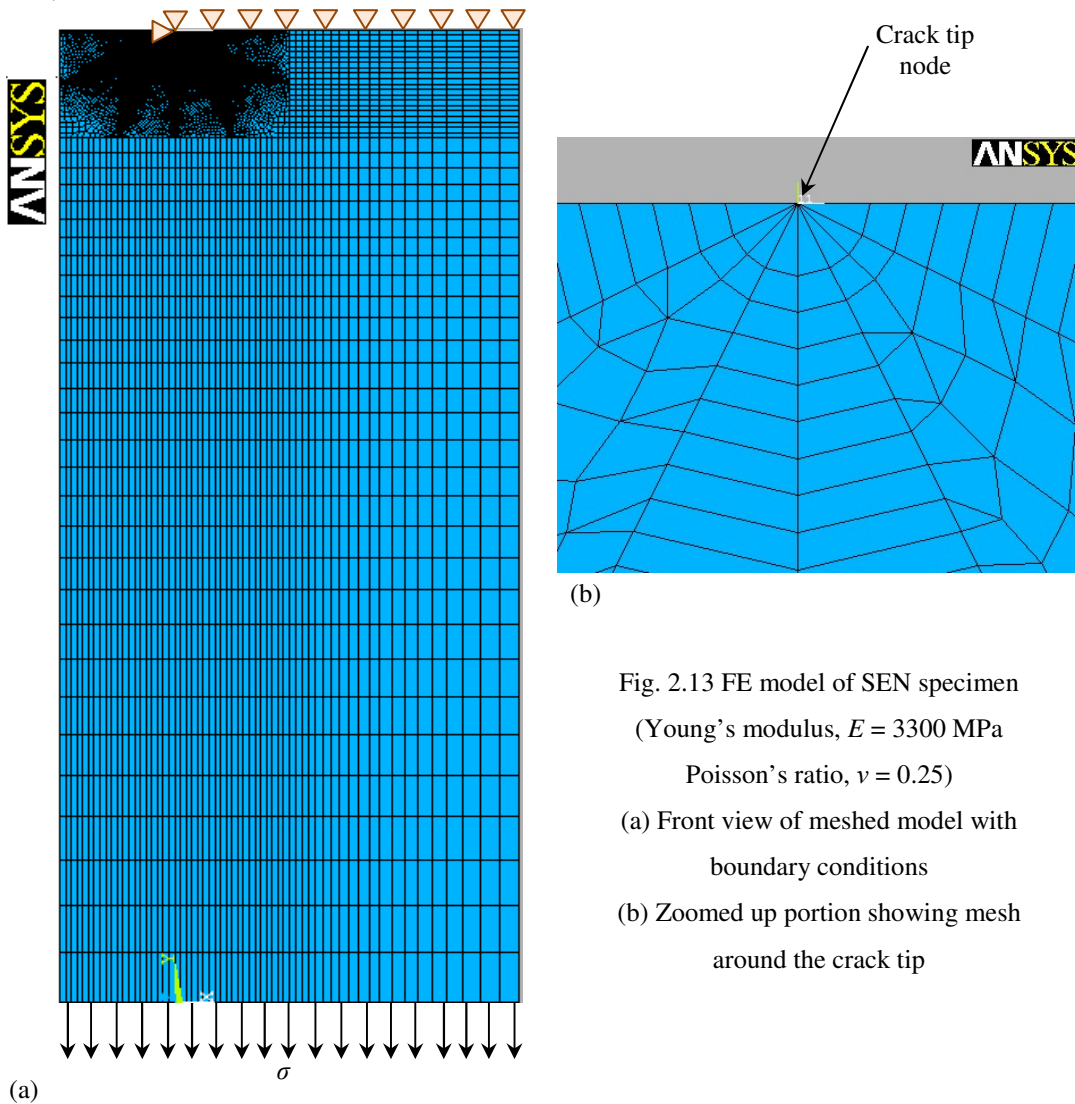


Fig. 2.13 FE model of SEN specimen  
(Young's modulus,  $E = 3300$  MPa  
Poisson's ratio,  $\nu = 0.25$ )

- (a) Front view of meshed model with boundary conditions  
(b) Zoomed up portion showing mesh around the crack tip



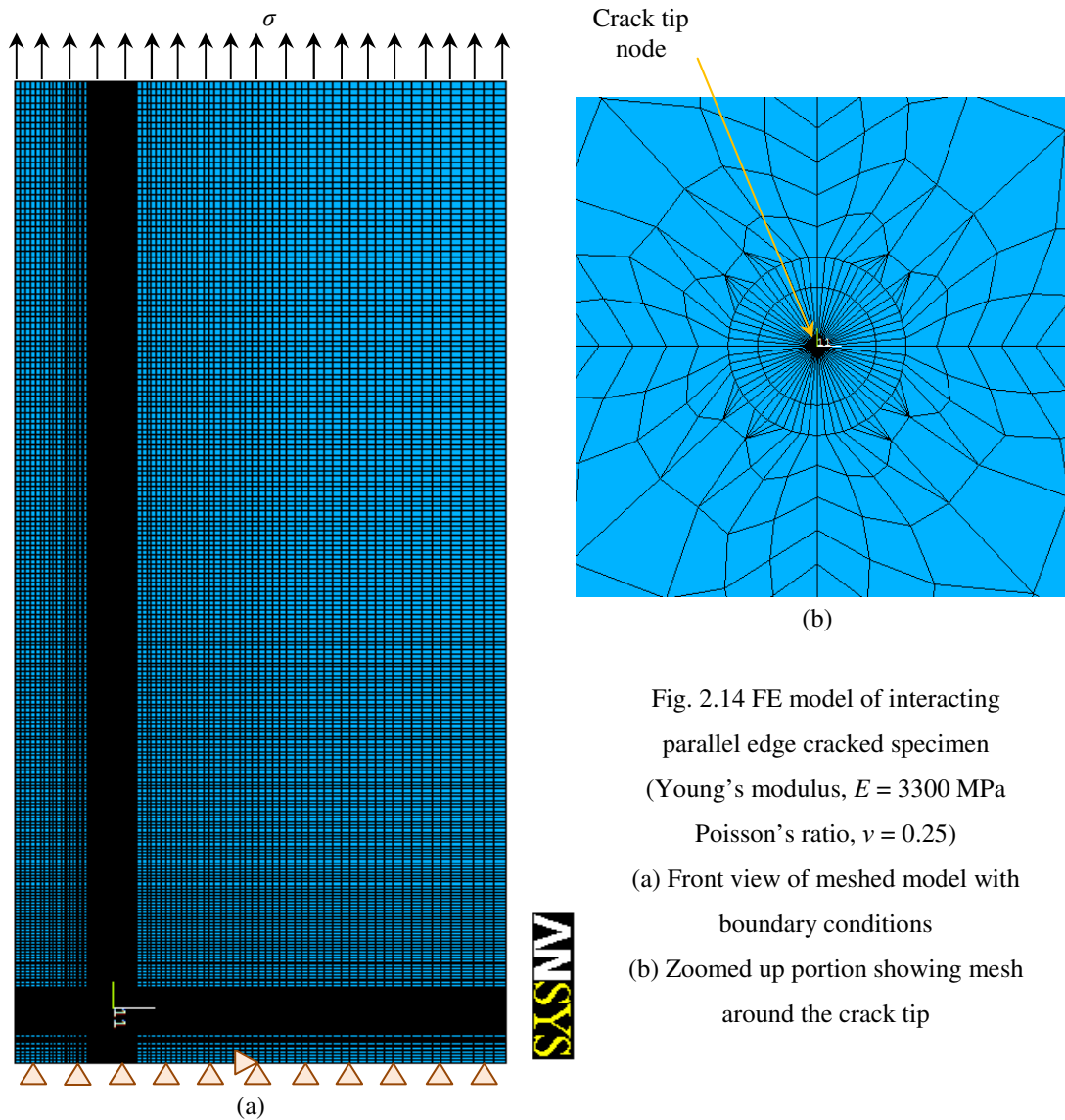


Fig. 2.14 FE model of interacting parallel edge cracked specimen  
(Young's modulus,  $E = 3300$  MPa  
Poisson's ratio,  $\nu = 0.25$ )

- (a) Front view of meshed model with boundary conditions  
(b) Zoomed up portion showing mesh around the crack tip

## 2.7 Results and Discussion

Fig. 2.15 shows the close view of the dark field isochromatic fringe pattern obtained near the crack tip for SEN specimen and interacting parallel edge cracked specimen. For SEN specimen, the fringe loops are symmetric about the crack-line while for interacting parallel edge cracked specimen, fringe loops are no more symmetric about the crack-line; instead the fringes are symmetric about the line parallel to both the crack faces and equidistant from both the cracks (refer Fig. 2.6). This is because, in case of parallel edge cracked panel, the stress fields around the two cracks tend to interact with each other; as a result the problem becomes of mixed-mode type even though the applied tensile load is along a direction normal to the crack faces. The influence of the  $K_{II}$  can also be seen in the form of relative displacement in  $x$ -direction between the two nodes on the crack line after the application of load in FE model.

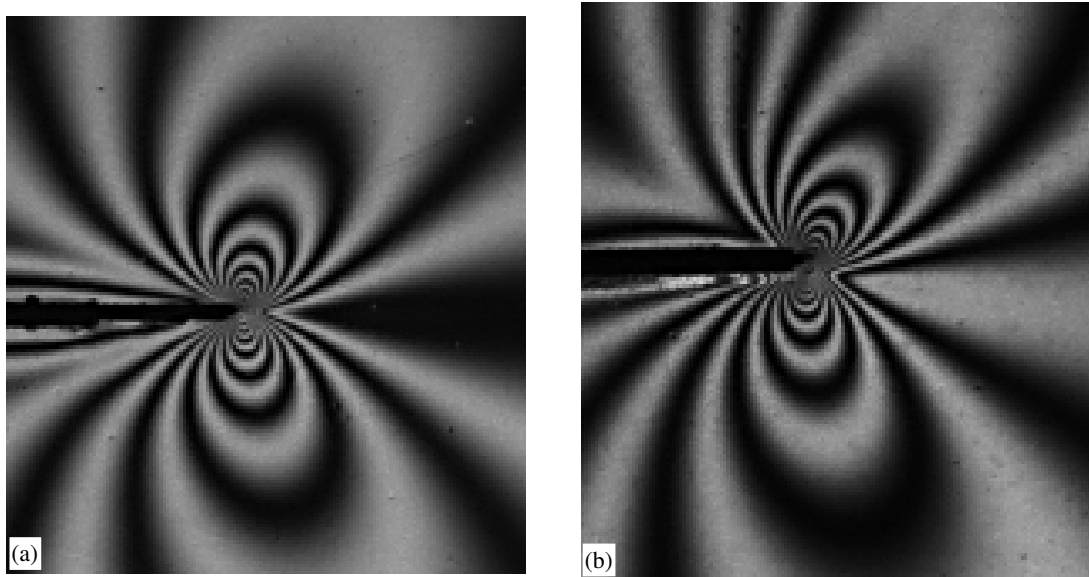


Fig. 2.15 Experimentally obtained dark field isochromatic fringe pattern for (a) SEN specimen, (b) interacting parallel edge cracked specimen

Table 2.4 summarizes the values of SIF's obtained using analytical (see Appendix A), numerical (FEM) and experimental (digital photoelasticity) method. For SEN specimen, a good agreement can be observed between the results obtained by all the three methods. For interacting parallel edge cracked specimen, results of FEM and experimental method show good agreement; however, analytical results show significant deviation. This is because of the fact that analytical closed form solution has been obtained by assuming semi-infinite geometry of interacting parallel edge cracked panel while the actual specimen is of finite geometry.

Table 2.4 comparison of results obtained by different methods

Specimen type	$K_I$ (MPa $\sqrt{\text{mm}}$ )				$K_{II}$ (MPa $\sqrt{\text{mm}}$ )			
	Analytical	FEM		Exp.	Analytical	FEM		Exp.
		Direct method	$J$ -integral method			Direct method	$J$ -integral method	
SEN	20.2405	20.226	20.192	18.3785	0	0	0	0.4089
Interacting parallel edge crack	12.7515	15.166	15.1649	14.9829	1.9834	2.0849	2.0855	2.1679

## **2.8 Closure**

In the present study, an attempt has been made to determine SIF's for SEN specimen and interacting parallel edge cracked specimen using digital photoelasticity. Special attention has been given for specimen preparation. Ten-step method has been used for accurate evaluation of total isochromatic fringe order. Automated data collection has been implemented in order to avoid any human error in data collection. Then, SIF's have been estimated using the over-deterministic nonlinear least square approach involving multiple data points. The experimental results are found to show good agreement with FE and analytical results. The slight difference between experimental and analytical / FE results can be due to reasons such as error introduced due to ambiguous location of the crack-tip and imperfect loading conditions. The present study highlights importance of using ten-step method in conjunction with automated data collection for improving the accuracy of the experimental results. The study also emphasizes the fact that physical insight gained from experiments can be used effectively while applying the boundary conditions in FE model.

# Chapter 3

## Estimation of SIF's using digital image correlation

### 3.1 Introduction

Experimental techniques that measure the surface deformation of components and structures, subjected to a variety of loading conditions, play an important role in many areas of engineering. Many techniques have evolved over the period of time to address the issue of accurate measurement of surface displacements and strains. These techniques include point-wise techniques such as resistance strain gauges as well as whole field non-contact optical techniques, based on interferometry such as holographic interferometry, speckle pattern interferometry, moiré interferometry etc. and non-interferometric techniques such as grid method and digital image correlation (DIC). However, many of these whole field interferometric techniques suffer from the disadvantage that they require complicated optical set up and have stringent stability requirements under experimental conditions which limit their applicability. DIC is now established in the field of experimental mechanics as an effective and flexible tool for the full field measurement of shape and deformation. This is due to the range of advantages DIC offers over the other experimental techniques such as simple optical set up, ease of specimen preparation, relatively less stringent requirements on measurement conditions and wide range of sensitivity of measurement. When used with a single recording camera (2D-DIC), it can measure only in-plane surface displacements of a planar object. When used with a stereo pair of cameras, it can measure three-dimensional surface displacements of any 3-D object. Now-a-days, many commercial DIC software's with a variety of advanced data processing features are available (e.g Vic-2D / Vic-3D, DaVis, ARAMIS, Q-400 etc.). Because of these reasons, DIC is becoming increasingly popular in the field of fracture mechanics.

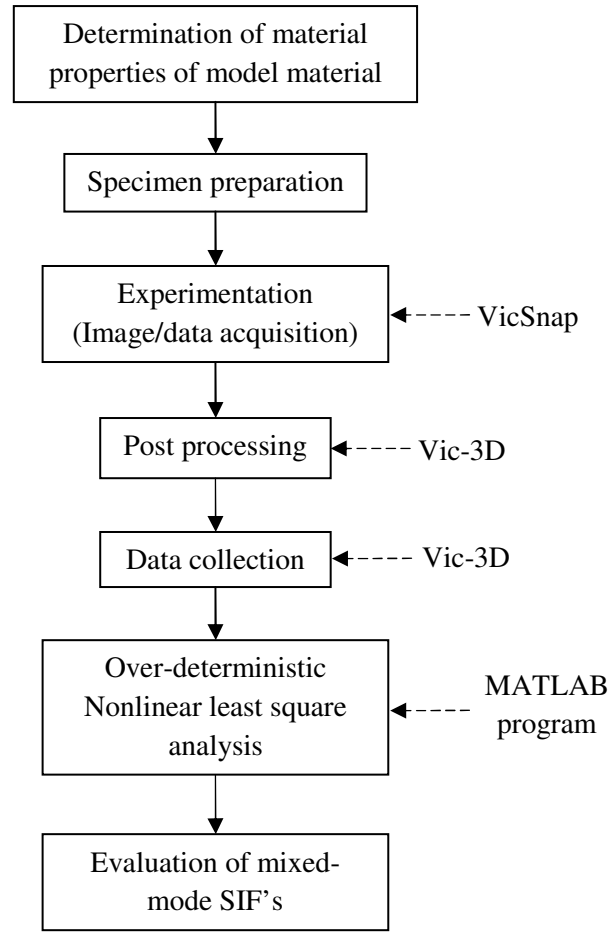


Fig. 3.1 General steps involved in the determination of mixed-mode SIF's using DIC

This chapter deals with the evaluation of mixed-mode SIF's using whole field displacement data obtained by 3D-DIC. Fig. 3.1 summarizes the general steps involved in the evaluation of fracture parameters using displacement field. It also shows the different codes / software used for various purposes in the present work (written outside the box). Over-deterministic non-linear least square algorithm, proposed by Yoneyama et al. [29] for the estimation of mixed-mode SIF's from whole field displacement field, has been implemented in modified form to achieve reliable and better rate of convergence. A modified form of the algorithm is implemented in MATLAB [46]. The required displacement field around the crack tip is obtained by analyzing the acquired images using commercially available software Vic-3D [47], whose advanced data processing features are used to collect data ( $x$ ,  $y$ ,  $u$  and  $v$ ) along  $u$  and  $v$  contours. Number of terms required in multi-parameter displacement field equations to model the displacement field correctly, is incremented until the reconstructed  $u$  and  $v$  displacement field matches with experimental distribution. This is cross checked by theoretically reconstructing  $u$  and  $v$  displacement contour maps. In order to validate the

methodology, mixed-mode SIF's have been estimated for five different specimen configurations representing different mode-mixity conditions and are compared with the analytical solutions.

### 3.2 Multi-parameter displacement field equations

Atluri and Kobayashi [28, 29] introduced the two-dimensional displacement field equations for the general mixed mode case which is as follows:

$$\begin{aligned} \begin{Bmatrix} u \\ v \end{Bmatrix} &= \sum_{n=1}^{\infty} \frac{A_{In}}{2G} r^{\frac{n}{2}} \begin{Bmatrix} k \cos \frac{n}{2} \theta - \frac{n}{2} \cos \left( \frac{n}{2} - 2 \right) \theta + \left\{ (-1)^n + \frac{n}{2} \right\} \cos \frac{n}{2} \theta \\ k \sin \frac{n}{2} \theta + \frac{n}{2} \sin \left( \frac{n}{2} - 2 \right) \theta - \left\{ (-1)^n + \frac{n}{2} \right\} \sin \frac{n}{2} \theta \end{Bmatrix} \\ &- \sum_{n=1}^{\infty} \frac{A_{IIIn}}{2G} r^{\frac{n}{2}} \begin{Bmatrix} k \sin \frac{n}{2} \theta + \frac{n}{2} \sin \left( \frac{n}{2} - 2 \right) \theta + \left\{ -(-1)^n + \frac{n}{2} \right\} \sin \frac{n}{2} \theta \\ -k \cos \frac{n}{2} \theta - \frac{n}{2} \cos \left( \frac{n}{2} - 2 \right) \theta + \left\{ -(-1)^n + \frac{n}{2} \right\} \cos \frac{n}{2} \theta \end{Bmatrix} \end{aligned} \quad (3.1)$$

where,  $G$  is shear modulus,  $k = (3 - \nu)/(1 + \nu)$  for plane stress condition and  $k = (3 - 4\nu)$  for plane strain condition.  $A_{II} = K_I / \sqrt{2\pi}$  and  $A_{III} = -K_{II} / \sqrt{2\pi}$  and  $4A_{I2} = -\sigma_{\theta x}$ . In Eq. (3.1), polar co-ordinates are measured from the crack tip as shown in Fig.1.1. In above displacement field equations, it is worth to be noted that  $A_{II2} = 0$ .

### 3.3 Over-deterministic nonlinear least squares methodology

#### 3.3.1 Formulation of equations

After accounting for rigid body motion, Eq. (3.1) can be rewritten as

$$u_x = \sum_{n=1}^{\infty} A_{In} f_I(r, \theta) - \sum_{n=1}^{\infty} A_{IIIn} f_{II}(r, \theta) + T_x + x(\cos R - 1) - y \sin R \quad (3.2a)$$

$$u_y = \sum_{n=1}^{\infty} A_{In} g_I(r, \theta) - \sum_{n=1}^{\infty} A_{IIIn} g_{II}(r, \theta) + T_y + y(\cos R - 1) + x \sin R \quad (3.2b)$$

where,  $f_I, f_{II}, g_I$  and  $g_{II}$  are trigonometric functions of position co-ordinates  $r$  and  $\theta$ ;  $T_x$  and  $T_y$  are rigid body translations in  $x$  and  $y$ -directions,  $R$  is the rigid body rotation. If we assume  $R$  is very small, then equations reduce to following form:

$$u_x = \sum_{n=1}^{\infty} A_{In} f_I(r, \theta) - \sum_{n=1}^{\infty} A_{IIIn} f_{II}(r, \theta) + T_x - Ry \quad (3.3a)$$

$$u_y = \sum_{n=1}^{\infty} A_{In} g_I(r, \theta) - \sum_{n=1}^{\infty} A_{IIIn} g_{II}(r, \theta) + T_y + Rx \quad (3.3b)$$

Although any of the Eq. (3.2) or (3.3) can be used in the implementation, Eq. (3.2) tend to increase the computational time by reducing the rate of convergence as it is non-linear in terms of unknowns  $T_x$ ,  $T_y$  and  $R$ . Equation (3.3) is not applicable when  $R$  cannot be assumed as small angle which is especially true when the initial guesses for the required unknowns are not close to their actual values. The compromise can be achieved by incorporating simple ‘if... else’ during the implementation of the algorithm. If  $-0.15 \leq R \leq 0.15$ , Eq. 3.3 is used otherwise Eq. 3.2 is used as a default one.

In many cases, there is ambiguity in location of the crack-tip due to low values of scale factors (pixel / mm). The location of the crack tip can be treated as one of the unknown to be determined in over-deterministic least square technique. In such case,

$$\left. \begin{aligned} r &= \sqrt{(x' - x_c)^2 + (y' - y_c)^2} \\ \theta &= \tan^{-1} \left( \frac{x' - x_c}{y' - y_c} \right) \\ x &= x' - x_c \\ y &= y' - y_c \end{aligned} \right\} \quad (3.4)$$

where,  $x_c$  and  $y_c$  are the locations of a crack tip relative to an arbitrary Cartesian co-ordinate system whose  $x$  and  $y$ -axes are parallel to that of crack tip co-ordinate system of Fig 1.1.

$x'$  and  $y'$  are the position co-ordinates of the point of interest relative to the same arbitrary Cartesian co-ordinate system. Error function can be defined as:

$$h_{xm} = u_x - (u_x)_{\text{exp}} \quad (3.5a)$$

$$h_{ym} = u_y - (u_y)_{\text{exp}} \quad (3.5b)$$

Applying Taylor series expansion,

$$\begin{aligned} (h_m)_{i+1} &= (h_m)_i + \frac{\partial h}{\partial A_{I1}}(\Delta A_{I1}) + \frac{\partial h}{\partial A_{I2}}(\Delta A_{I2}) + \dots + \frac{\partial h}{\partial A_{Ik}}(\Delta A_{Ik}) + \frac{\partial h}{\partial A_{III}}(\Delta A_{III}) \\ &+ \frac{\partial h}{\partial A_{II2}}(\Delta A_{II2}) + \dots + \frac{\partial h}{\partial A_{IIIn}}(\Delta A_{IIIn}) + \frac{\partial h}{\partial T_x}(\Delta T_x) + \frac{\partial h}{\partial T_y}(\Delta T_y) + \frac{\partial h}{\partial x_c}(\Delta x_c) + \frac{\partial h}{\partial y_c}(\Delta y_c) \end{aligned}$$

Where  $i = i^{\text{th}}$  iteration step and  $\Delta A$  is correction to be added to the previous estimates of  $A$

To determine the corrections,  $(h_m)_{i+1} = 0$

$$\begin{aligned} -(h_m)_i &= \frac{\partial h}{\partial A_{I1}}(\Delta A_{I1}) + \frac{\partial h}{\partial A_{I2}}(\Delta A_{I2}) + \dots + \frac{\partial h}{\partial A_{Ik}}(\Delta A_{Ik}) + \frac{\partial h}{\partial A_{III}}(\Delta A_{III}) + \\ &\frac{\partial h}{\partial A_{II2}}(\Delta A_{II2}) + \dots + \frac{\partial h}{\partial A_{IIIn}}(\Delta A_{IIIn}) + \frac{\partial h}{\partial T_x}(\Delta T_x) + \frac{\partial h}{\partial T_y}(\Delta T_y) + \frac{\partial h}{\partial x_c}(\Delta x_c) + \frac{\partial h}{\partial y_c}(\Delta y_c) \end{aligned}$$

Rearranging in matrix form,

$$\begin{aligned} \{h\}_i &= -[b]_i \{\Delta A\}_i \\ \{\Delta A\}_i &= -[c]_i^{-1} \{d\}_i \end{aligned} \quad (3.6)$$

$$\text{where, } [c]_i = [b]_i^T [b]_i \text{ and } \{d\}_i = [b]_i^T \{h\}_i$$

$$\{A\}_{i+1} = \{A\}_i + \{\Delta A\}_i$$

### 3.3.2 Convergence criteria

The above equations are solved using Newton-Raphson scheme in an iterative manner. The iterations are stopped using two criteria, namely: (a) Parameter error ( $\Delta A$ ) minimization (b) minimization of displacement vector sum error which is defined as

$$\frac{\sum |u_{theory} - u_{exp}|}{\text{Total no. of data points}} \leq \text{Convergence error}$$

where,  $u_{theory}$  is vector sum of theoretically recalculated  $u$  and  $v$ -displacements and  $u_{exp}$  is vector sum of experimental  $u$  and  $v$ -displacements.

The solution for the given number of parameters is considered as acceptable when the convergence error is of the order of 0.001 and parameter error ( $\Delta A$ ) becomes reasonably small (say of the order of  $10^{-2}$ ).

### 3.3.3 Implementation

The above described procedure has been implemented in MATLAB [46] program which requires three input excel files (with extension '.xlsx'). Out of three input files, one file contains the pixel data collected along  $u$ -contour and other file contains the pixel data collected along  $v$ -contour. The third file contains the material properties of the model material and the values of  $u$  and  $v$ -contours for the data point collected. Since the number of parameters required for modeling the displacement field is not known a priori, the iteration is started with minimum number of parameters in the displacement field equations. The contour maps for  $u$  and  $v$ -displacement components are reconstructed at every stage using the obtained parameters for cross-verification with experimental data. This method of cross-verification has been popular in the field of photoelasticity and the same has been used here. For the comparison between the theoretically reconstructed and experimentally obtained displacement field, the data points are echoed back. If the converged solution does not model the displacement field correctly, then by using the solution of  $T_x$  and  $T_y$  thus obtained as their starting values, the number of parameters is increased by one. The process is continued until a good match is obtained between the theoretically reconstructed and experimentally obtained displacement contours.



### **3.4 Experimental validation**

#### **3.4.1 Specimen preparation**

As mentioned in section 3.1, five different specimen configurations are considered in the present work for the validation of methodology, viz. - Single edge notched (SEN) panel, single center cracked (SCC) panel, interacting parallel edge cracked panel, edge slant cracked (ESC) panel and center slant cracked (CSC) panel. Experiments are conducted on the test specimens machined from 3 mm thick sheet of aluminum alloy (Al 2014 T6), material properties of which are determined according to ASTM E 8M-04 [48]. The material is a high strength alloy and is used extensively in aerospace industry. Figure 3.2 shows the specimen geometry for various specimen configurations. In order to simulate the natural crack, test specimens are pre-cracked in fatigue loading condition using MTS Landmark<sup>®</sup> servo-hydraulic cyclic testing machine of 100 kN capacity. For fatigue pre-cracking, fatigue crack starter notches having root radii of 0.25 mm are machined into the test specimens using wire-EDM (electro-discharge machining) process. For ease of crack detection, both the sides of specimens are polished with emery paper of fine grade P#2000 using BOSCH<sup>®</sup> portable polishing machine. Care is taken while locating and securing the specimens in the hydraulic test fixtures so as to have approximately similar fatigue crack growth behavior on both the sides of the specimen. During the pre-cracking process, specimen is monitored closely with magnifying glass. Liquid dye-penetrant NDT-19 is used to detect any fatigue crack initiation. Fatigue pre-cracking is conducted using force control mode and a short crack of the approximate length of 0.5-1 mm is obtained for all the test specimens. Using optical microscope, lengths of the cracks are measured on both the sides of the specimens and total crack-length is obtained by averaging the values of measured crack lengths on both the sides of the specimen. Table 3.1 summarizes the details of the fatigue pre-cracking procedure. Figure 3.3 shows the optical microscope image of short fatigue crack obtained for SEN specimen using the procedure described above. Then, the pre-cracked test specimens are cleaned thoroughly with isopropyl alcohol. The surface of the specimens are coated with thin layer of white acrylic paint and over-sprayed with carbon black paint using an airbrush to obtain a random black-and-white speckle pattern.

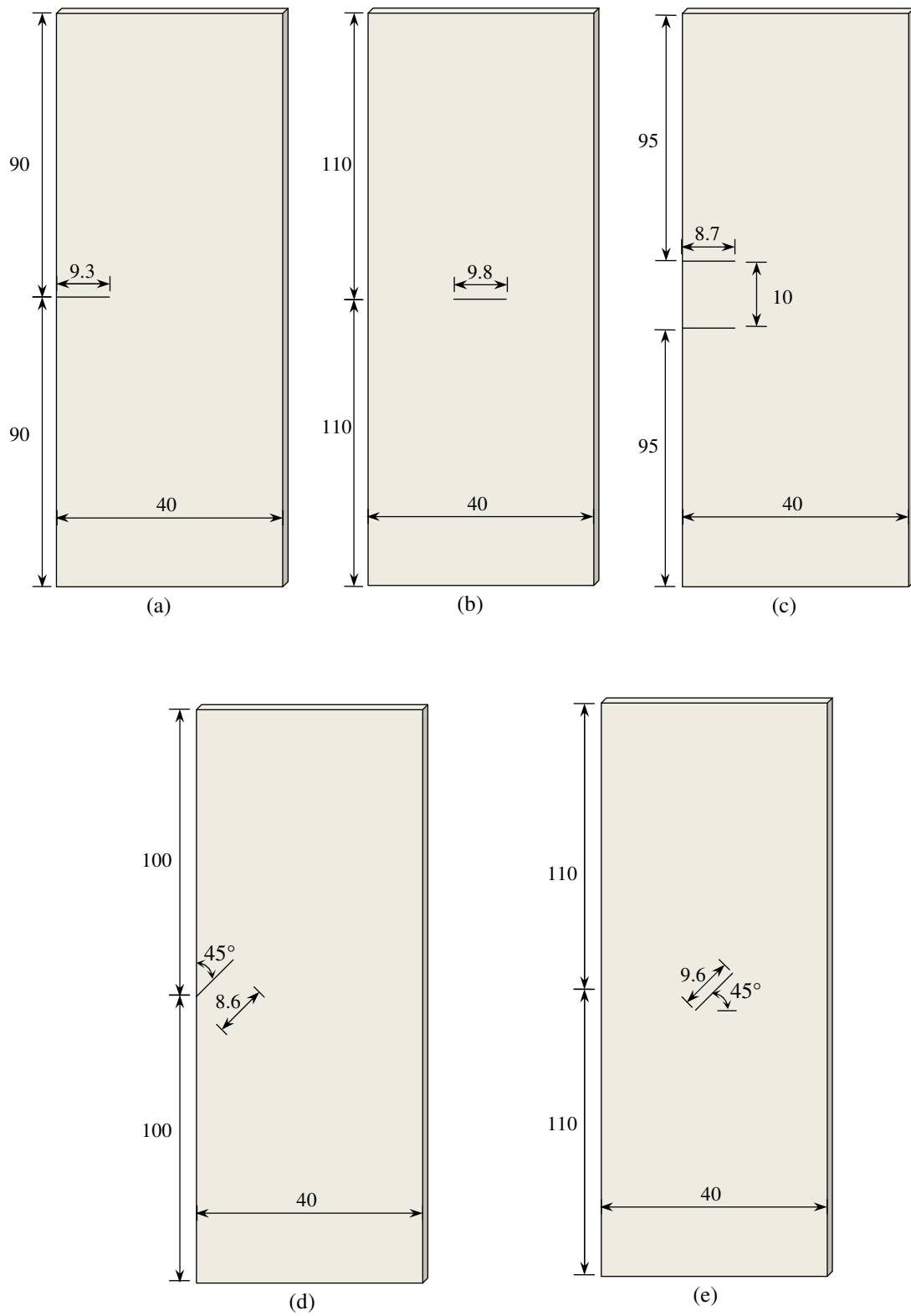


Fig. 3.2 Specimen geometries for various specimen configurations  
 (all dimensions are in mm) (a) SEN (b) SCC (c) parallel edge cracked (d) ESC (e) CSC  
 All dimensions are in mm.

Table 3.1 Summary of fatigue pre-cracking procedure

Specimen type	Initial notch length, $a_0$ (mm)	Final crack length, $a_f$ (mm)	Mean load, $P_{\text{mean}}$ (kN)	Amplitude of load, $P_{\text{amp}}$ (kN)	Number of cycles, $N$ (Hz)	Frequency $f$ (Hz)
SEN	9	9.3	4	3	14012	5
SCC	8	9.8	4	3.8	35500	10
ESC	8	8.6	3.5	3	11034	10
CSC	9	9.6	5	3.5	15000	10
Parallel edge cracked	8	8.7	3	3	5538	10

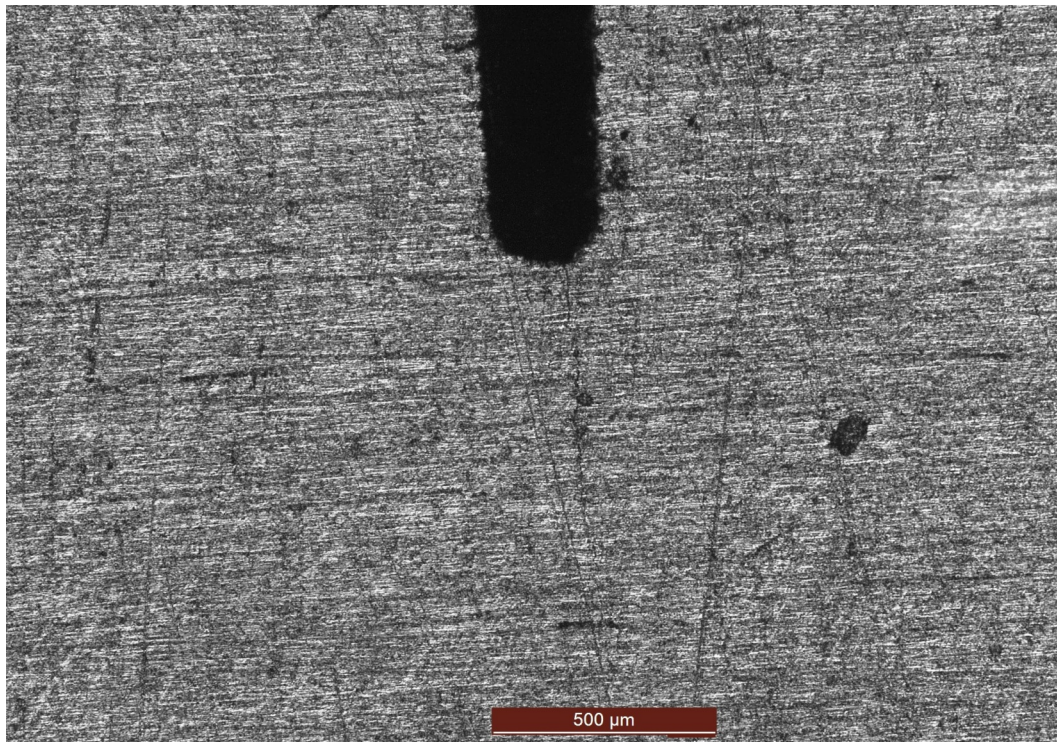


Fig. 3.3 showing the optical microscope image of short fatigue crack obtained for SEN specimen

### 3.4.2 Experimental procedure

Fig. 3.4 shows the typical experimental setup used in the present study. The hardware for the optical setup of stereo vision (3D-DIC) system that comprises a pair of CCD cameras (of  $2448 \times 2048$  spatial resolution with 8 bit intensity resolution and frame rate of 15 fps), Schneider Xenoplan lenses of 17 mm focal length, a portable computer system with image acquisition card and halogen lighting to ensure adequate image contrast. All the experiments are performed using a computer-controlled MTS Landmark<sup>®</sup> servo-hydraulic cyclic testing machine of 100 kN capacity with a computer data acquisition system. Self-adjusting hydraulic test fixtures are used to grip the specimens. Uniaxial tensile load is applied along longitudinal direction of the test specimens using displacement control mode with the crosshead speed of 0.5 mm / min. In order to facilitate the analysis of crack-tip displacements, the stereo vision system is so aligned with the test specimens that crack faces coincide with horizontal axis of the image co-ordinate system (see Fig. 3.5). Prior to the experiment, after adjusting the focus and aperture, stereo vision system is calibrated separately for each specimen using 15-20 pairs of images of a planar dot grid pattern (having a well-known spacing) rotated and tilted in different orientations. Then, clear and high quality images of the specimen surface (with a typical scale factor of 14-15 pixels/mm)

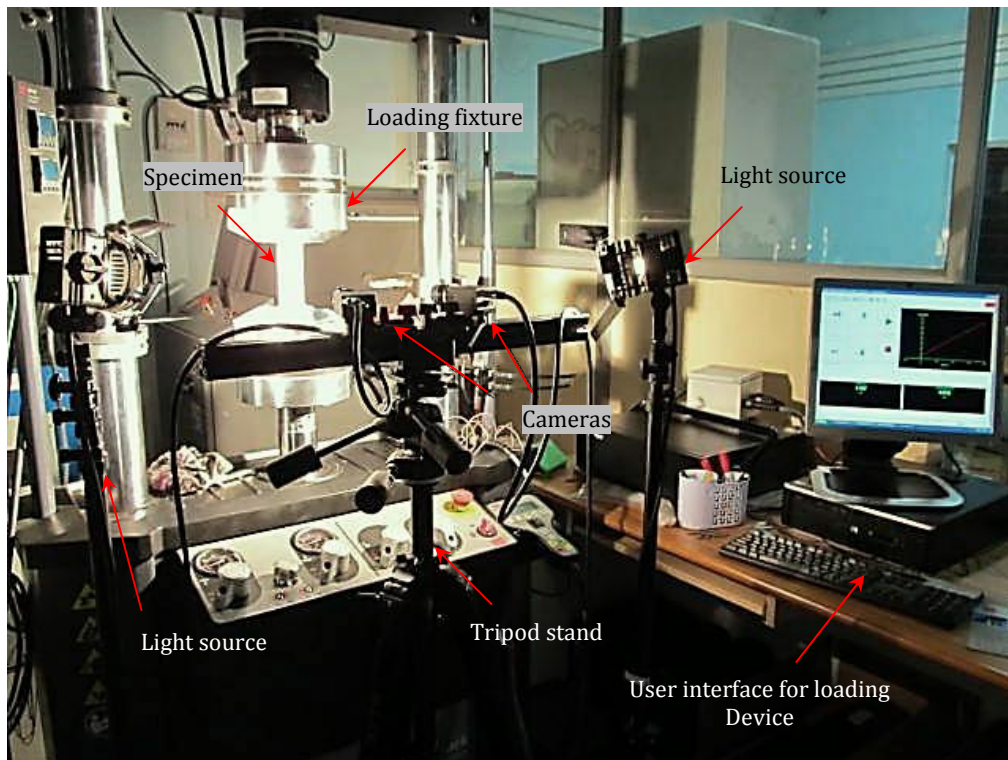


Fig. 3.4 Experimental set-up used for 3D-DIC



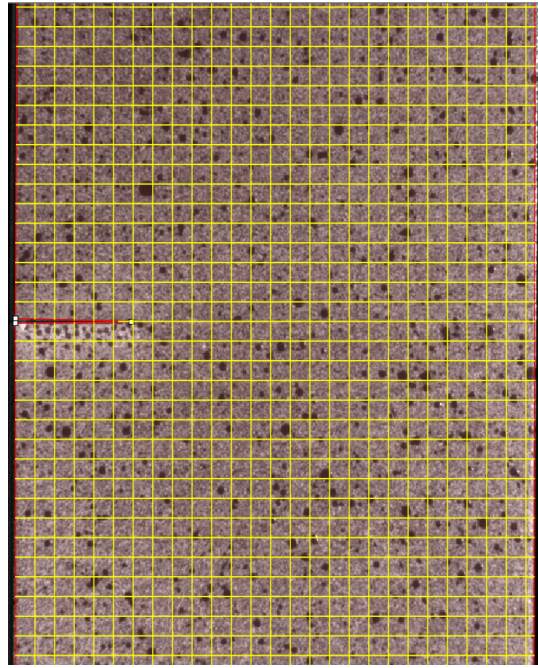


Fig. 3.5 Experimental set-up used for ESC and CSC specimen

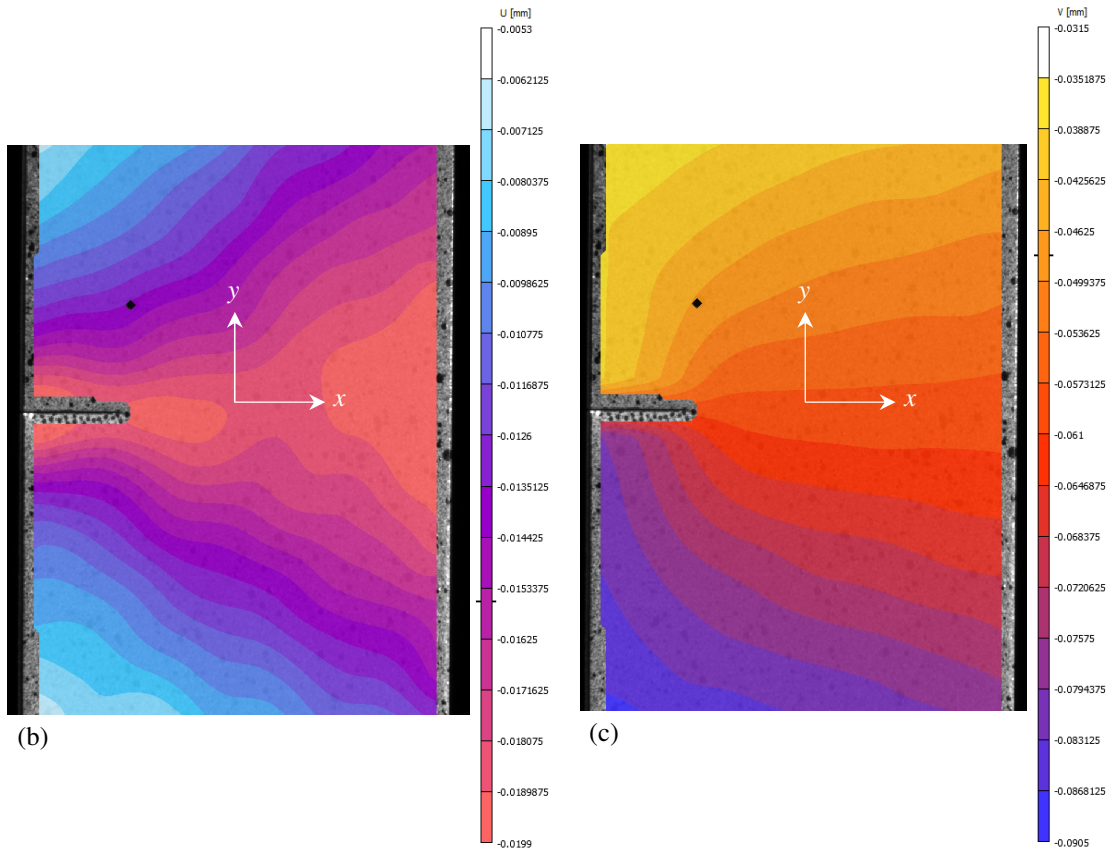
are grabbed continuously using the image acquisition system VicSnap [47] at regular time intervals. In order to ensure one-to-one correspondence between the image and instantaneous load, acquisition of images and load data is synchronized by direct input of load signals into VicSnap.

### 3.4.3 Data analysis

The images acquired by the stereo vision system are analyzed using the commercially available Vic-3D software [47] to obtain the whole field displacement distribution in the region surrounding the crack tip (Refer Fig. 3.6 and 3.7). Using the advanced data processing capabilities of Vic-3D, data ( $x'$ ,  $y'$ ,  $u$  and  $v$ ) are collected along contours of  $u$  and  $v$ -displacement components. Data is collected from the annular region surrounding the crack-tip, the inner radius of which is chosen more than half of the specimen thickness to avoid the three-dimensional effects [49] and non-linear process zone in the vicinity of the crack tip. The outer radius of the annular data collection region is limited such that  $r/a \leq 1$ . Total 1000-1300 data points are collected for each specimen individually. An over-deterministic non-linear least squares procedure is then invoked using MATLAB program to evaluate the multiple parameters governing the displacement field. Table 3.2 gives the summary of the data analysis for different specimens.



(a)



(b)

(c)

Fig. 3.6 showing the results of data analysis for SEN specimen

(a) region of interest with subsets used for correlation (b)  $u$ -displacement contour map (c)  $v$ -displacement contour map (subset size:  $17 \times 17$ )

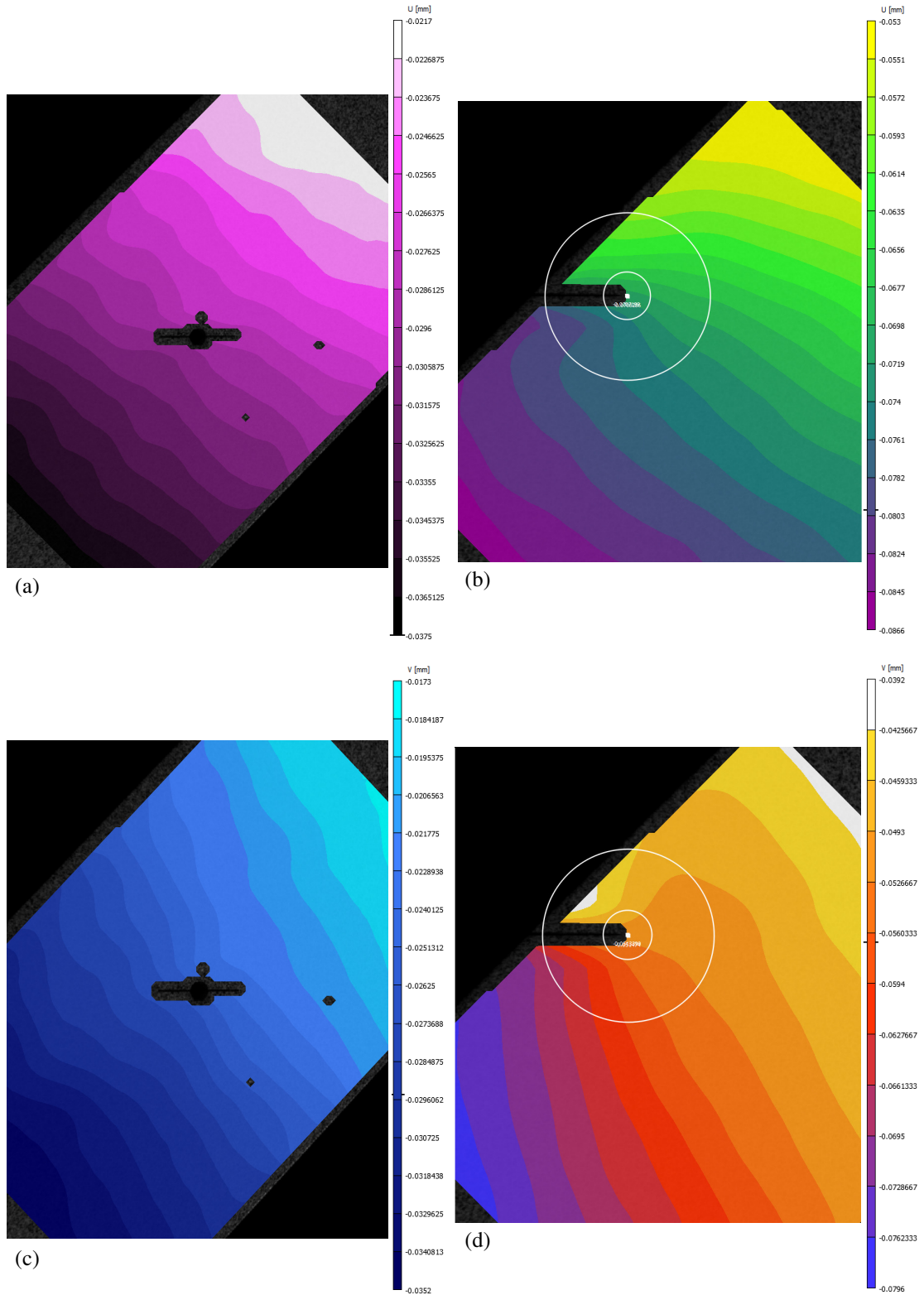


Fig. 3.7 showing the results of data analysis with subset size:  $15 \times 15$   
 (a)  $u$ -displacement contour map, (c)  $v$ -displacement contour maps for CSC specimen  
 (b)  $u$ -displacement contour map, (d)  $v$ -displacement contour maps for ESC specimen  
 (b) and (d) shows the zone of data collection for ESC specimen



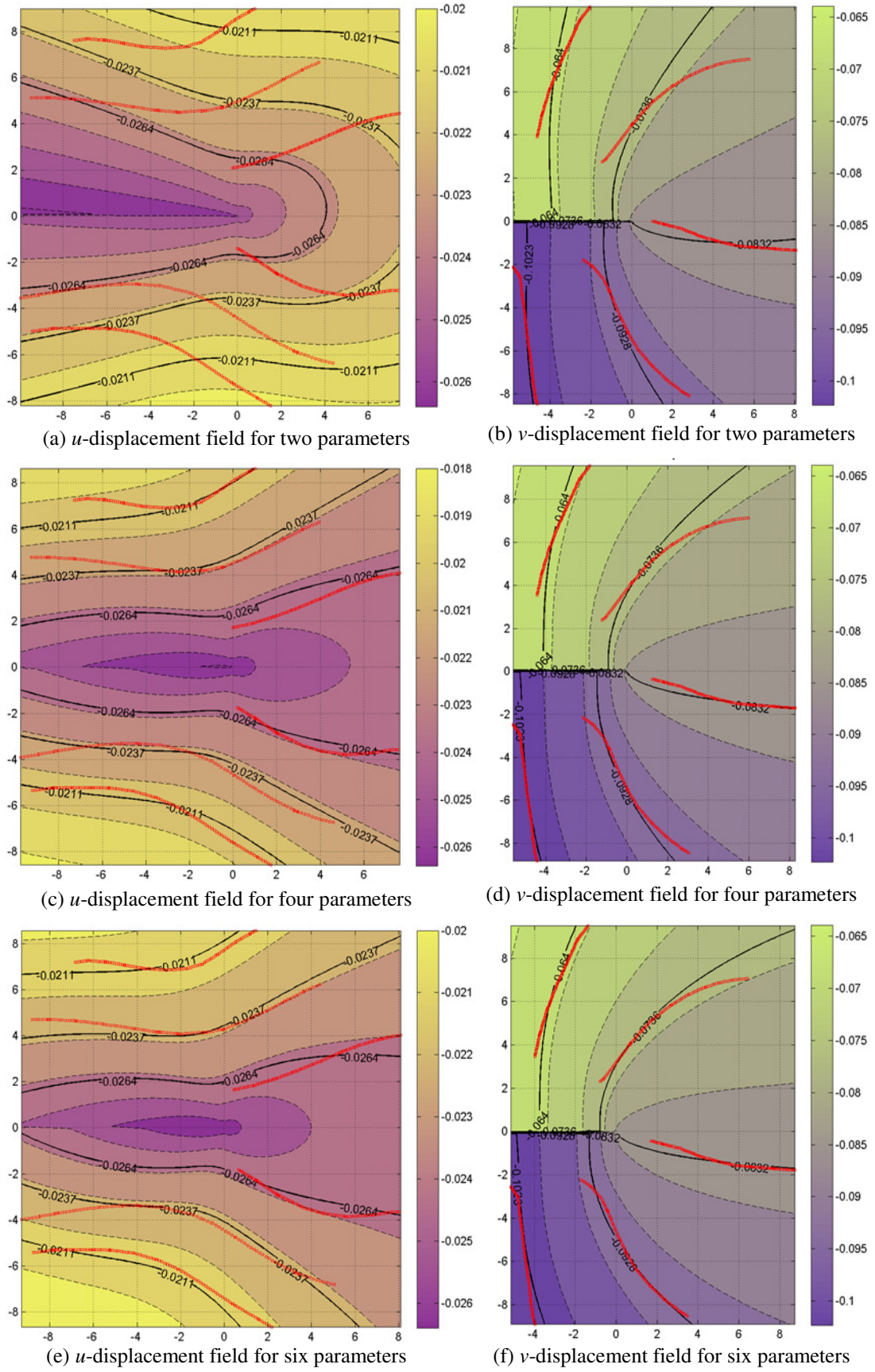


Fig. 3.8 Theoretically reconstructed displacement field for SEN specimen for various parameters



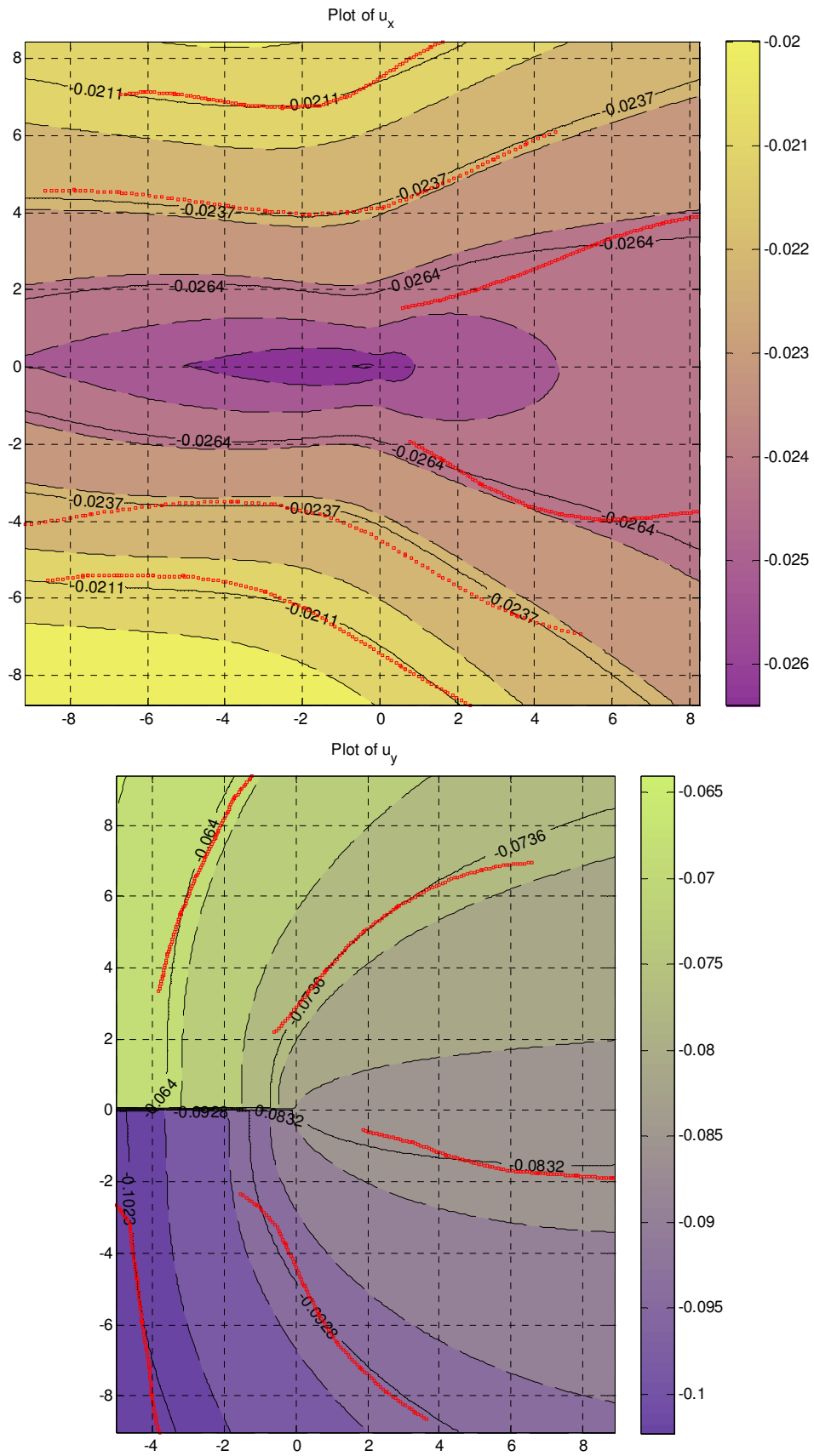


Fig. 3.9 Theoretically reconstructed displacement field for SEN specimen (8-parameter solution) with data points echoed back (indicated by red marker points)

Figure 3.8 and 3.9 shows the theoretically reconstructed displacement field around the crack tip of SEN specimen (subjected to a load of 7.5 kN) obtained using various parameters with the data points echoed back (indicated by red colored marker dots). For 8 parameters, the data points coincide very well with reconstructed contours assuring the sufficiency of eight parameters. Comparing  $K_I$  with its analytical value, the error is around 9.34 %. Figure 3.10 shows the variation of  $K_I$  and  $K_{II}$  as a function of number of parameters.

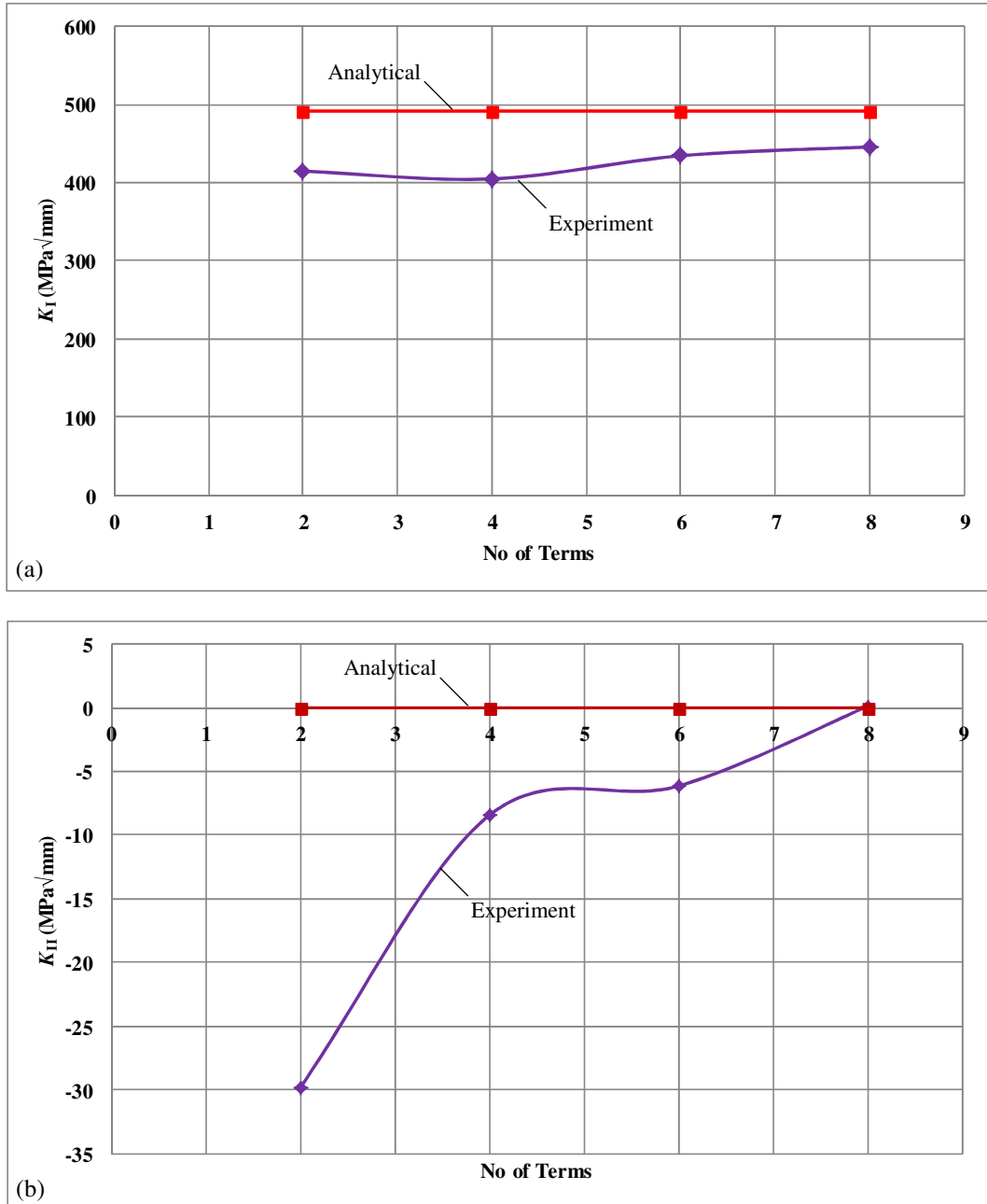


Fig. 3.10 Graph showing (a) variation of  $K_I$  (b) variation of  $K_{II}$  as a function of number of parameters

Figure 3.11 shows the graph of variation of convergence error achieved as well as calculated co-ordinates of the crack-tip location ( $x_c$  and  $y_c$ ) as a function of number of parameters for SEN specimen. With the increase in number of parameters, the convergence error reduces and also, the co-ordinates of the crack-tip stabilize to constant value. It is to be noted that co-ordinates of the crack-tip are with respect to image co-ordinate system. The value of  $x_c = -9.9$  mm and  $y_c = 1.27$  mm.

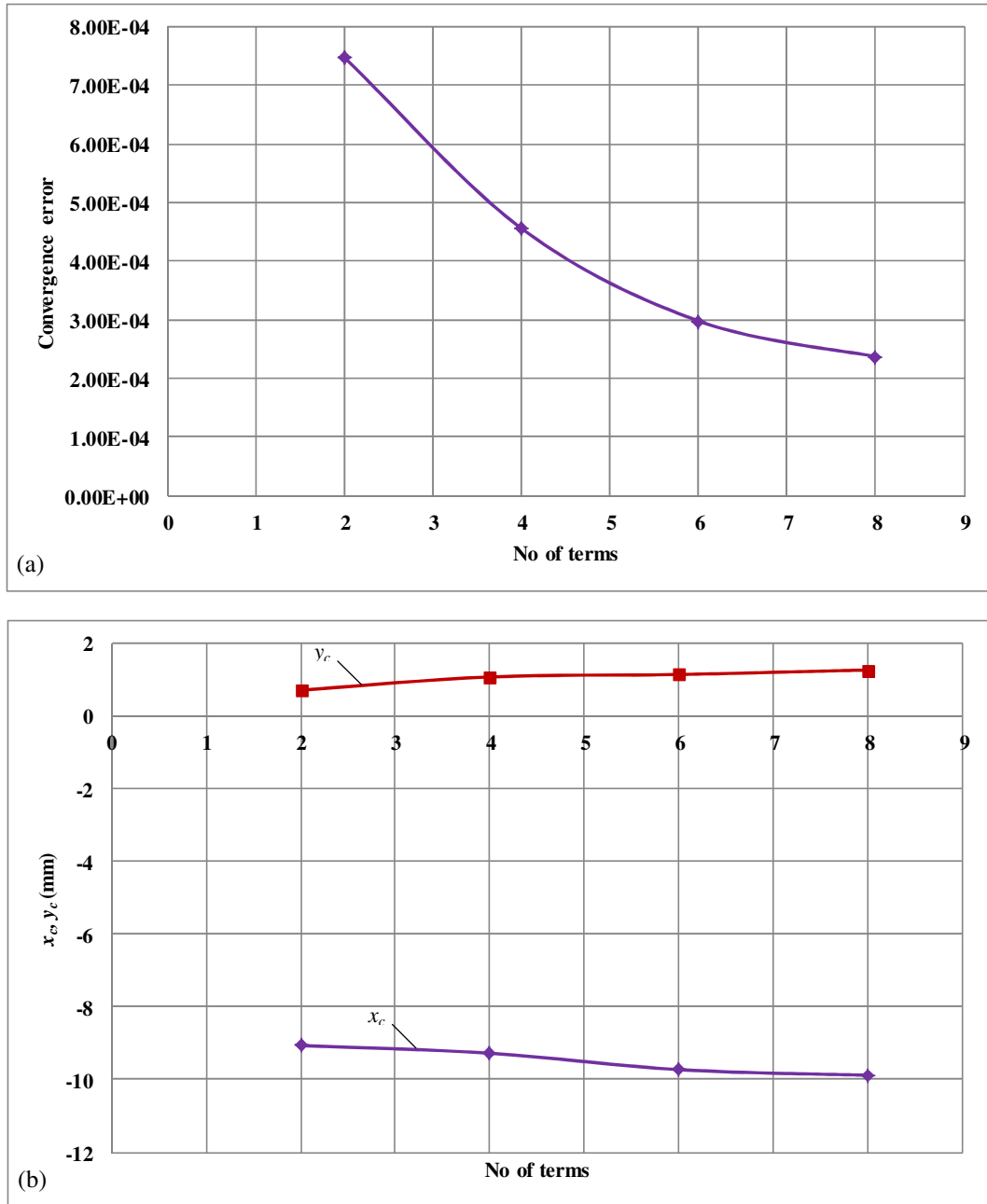


Fig. 3.11 Graph of (a) convergence error and (b) co-ordinates of the crack-tip location vs. number of parameters

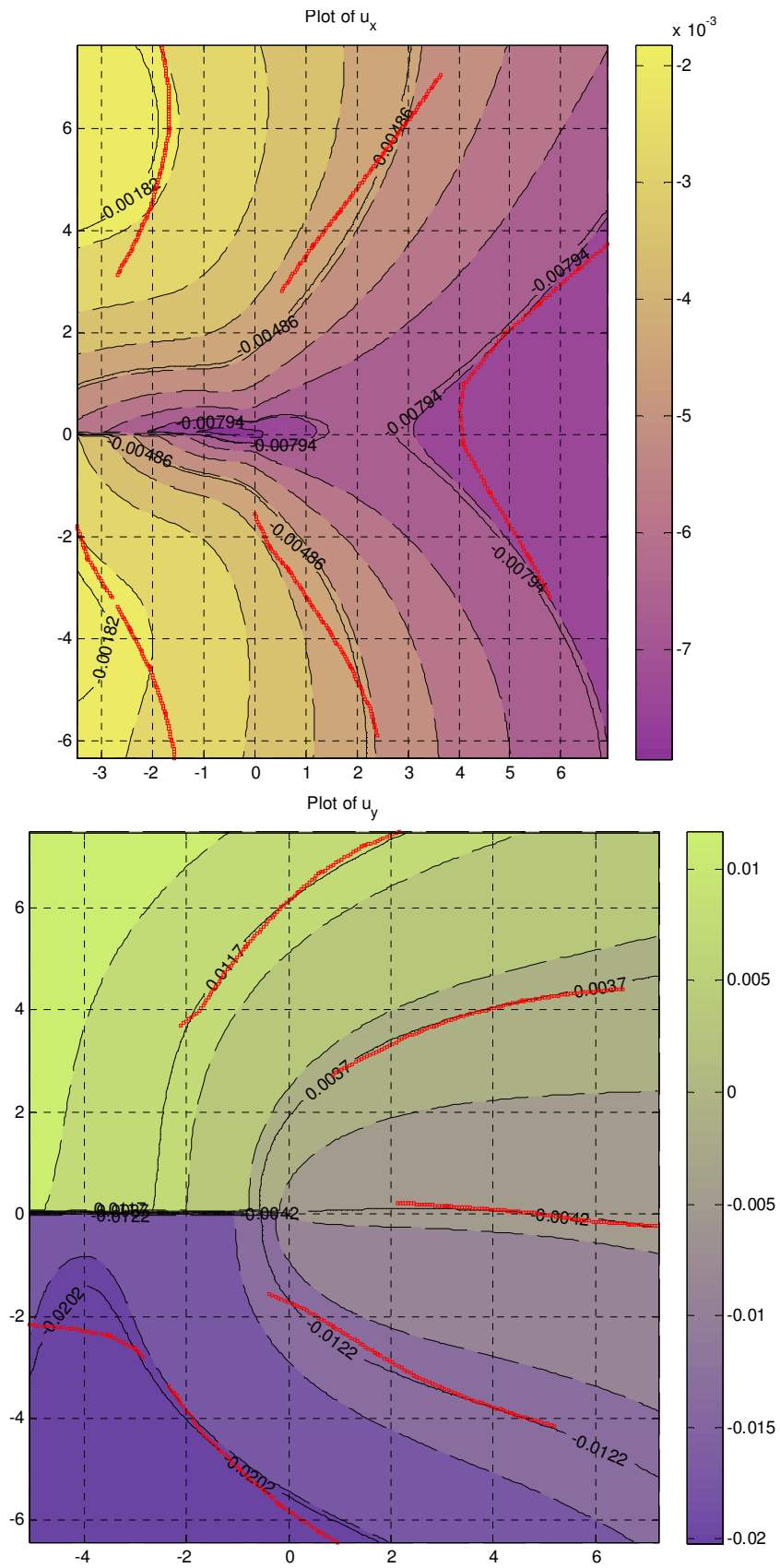


Fig. 3.12 Theoretically reconstructed displacement field for SCC specimen (14-parameter solution) with data points echoed back (indicated by red marker points)

Figure 3.12 shows the theoretically reconstructed displacement field around the crack tip of SCC specimen (subjected to a load of 15 kN) obtained using fourteen-parameter solution with data points superimposed (indicated by red colored marker dots). Similarly, Fig. 3.13 shows the theoretically reconstructed displacement field for CSC specimen (subjected to 10 kN load) obtained using fourteen-parameter solution with data points echoed back (showed by red colored marker points). Here too, in both the cases, data points coincide reasonably well with reconstructed displacement field.

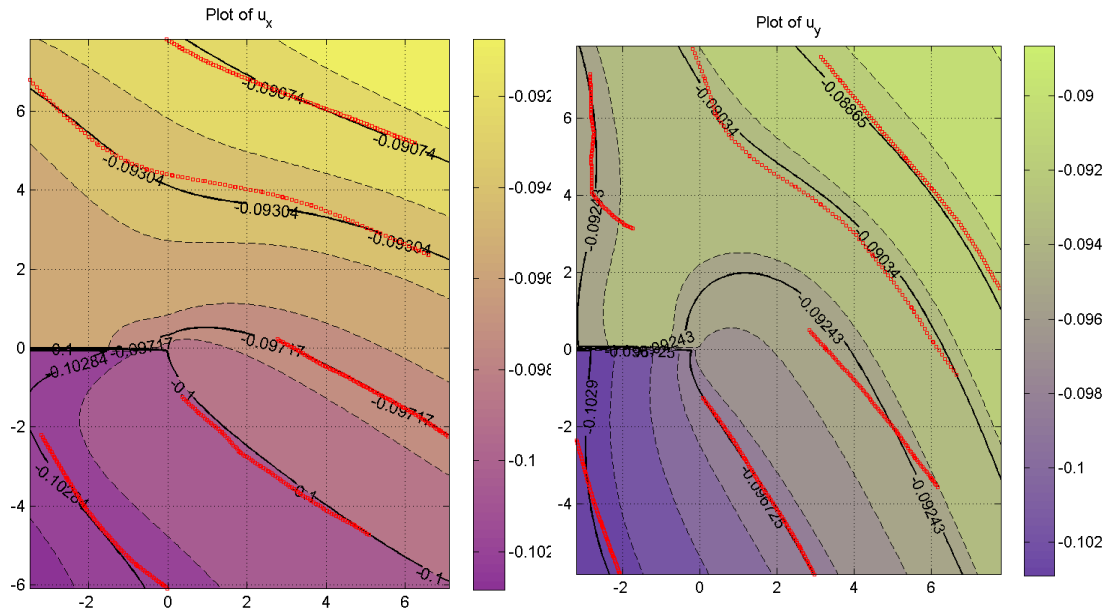


Fig. 3.13 Theoretically reconstructed displacement field for CSC specimen (14-parameter solution) with data points echoed back (indicated by red marker points)



Fig. 3.14 Graph showing variation of  $K_I$  as a function of number of parameters

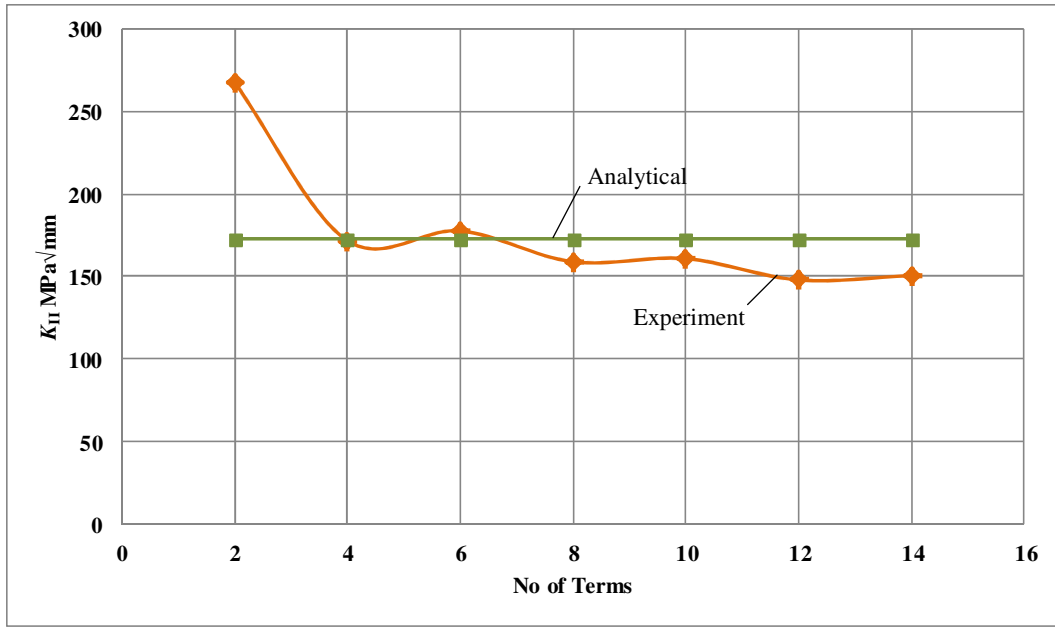


Fig. 3.15 Graph showing variation of  $K_{II}$  as a function of number of parameters

Figure 3.14 and Fig. 3.15 shows the variation of  $K_I$  and  $K_{II}$  as a function of number of parameters for CSC specimen. Fig. 3.16 shows the graph of variation of calculated co-ordinates of the crack-tip location ( $x_c$  and  $y_c$ ) as a function of number of parameters and Fig. 3.17 shows the graph of variation of convergence error achieved for CSC specimen. The percentage error in the analytical and experimental values of  $K_I$  is 4.8% and for  $K_{II}$ , this difference is 12.9 %. The co-ordinates of the crack-tip are found to be,  $x_c = 4.799$  mm and  $y_c = -0.0913$  mm ( $x_c$  and  $y_c$  measured with respect to image co-ordinate system).

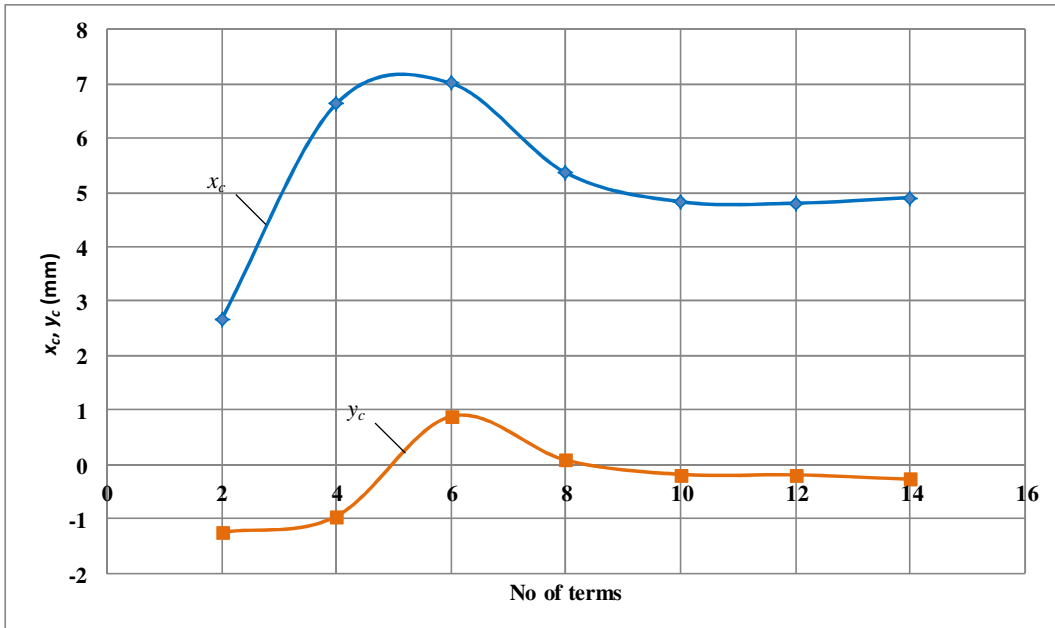


Fig. 3.16 Graph of co-ordinates of the crack-tip location vs. number of parameters

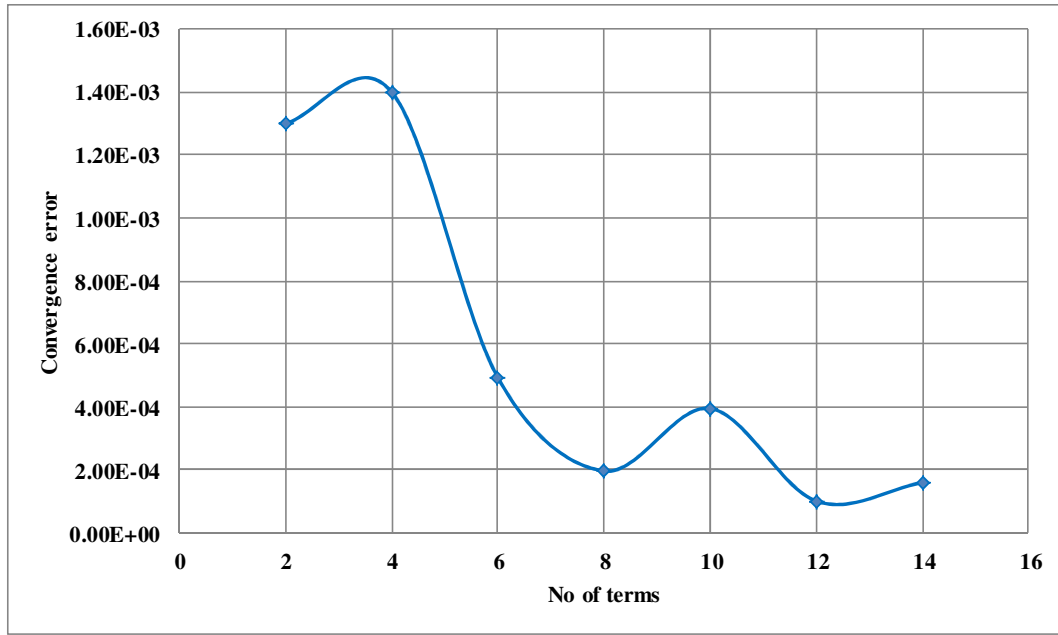


Fig. 3.17 Graph of convergence error vs. number of parameters

Figure 3.18 shows the theoretically reconstructed displacement field around the crack tip of parallel edge cracked specimen (subjected to a load of 15 kN) obtained using sixteen-parameter solution with data points echoed back (indicated by red colored marker dots). Similarly, Fig. 3.19 shows the theoretically reconstructed displacement field around the crack tip of ESC specimen (subjected to a load of 10 kN) obtained using eight-parameter solution with data points echoed back (showed by red colored marker points). In both the cases, data points match well with the reconstructed displacement contours, thus ensuring the sufficiency of the number of parameters.

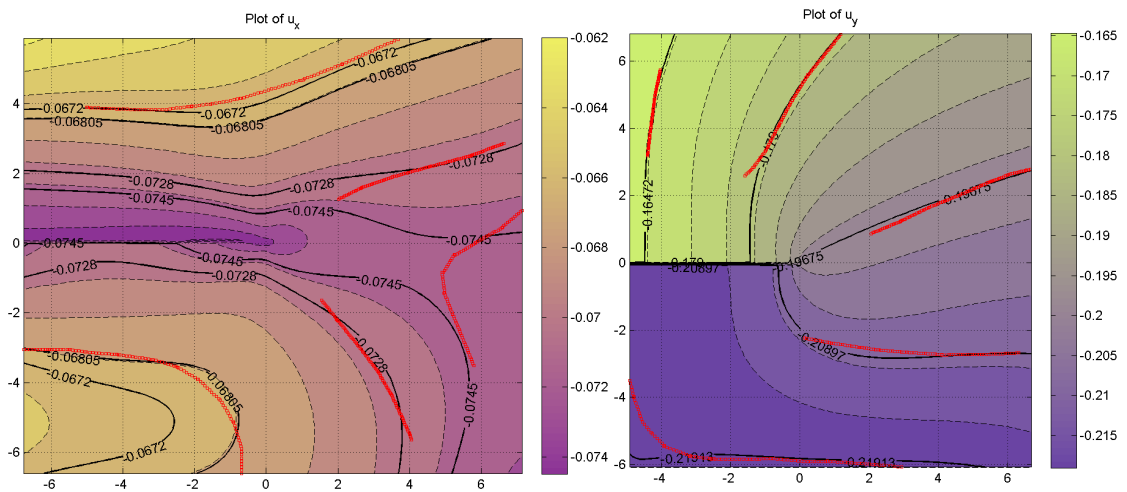


Fig. 3.18 Theoretically reconstructed displacement field for parallel edge cracked specimen (16-parameter solution) with data points echoed back (indicated by red marker points)

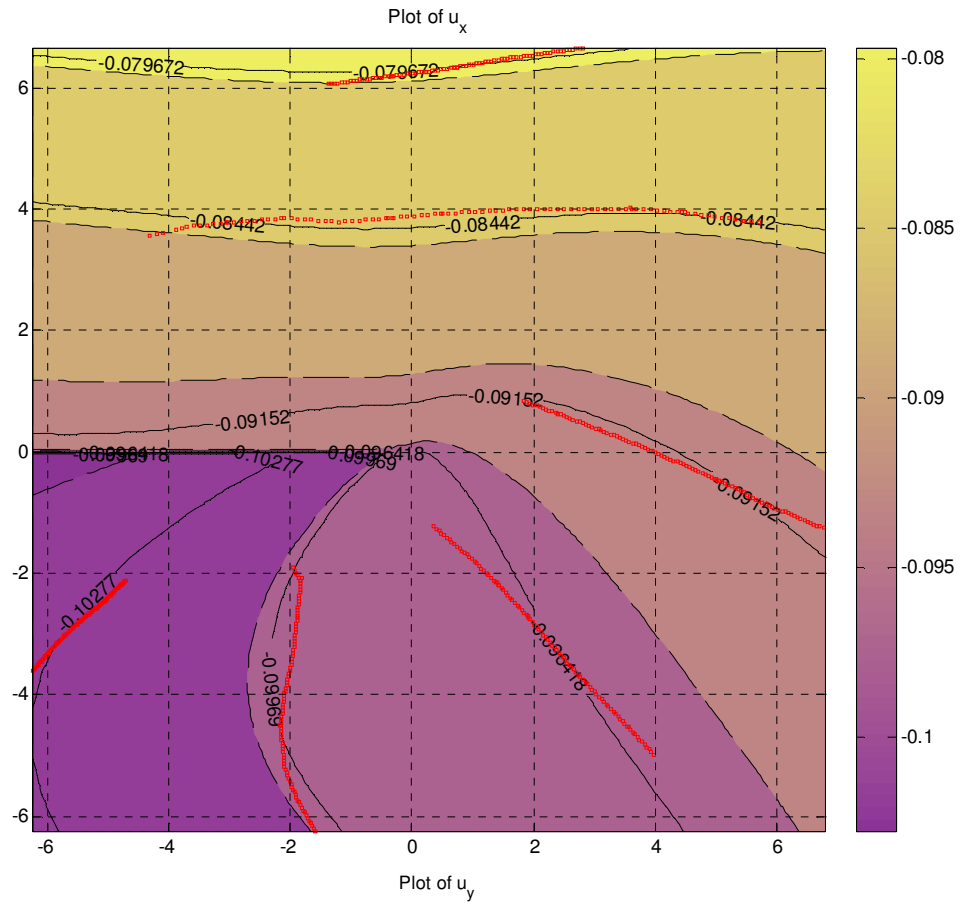


Fig. 3.19 Theoretically reconstructed displacement field for ESC specimen (8-parameter solution)  
with data points echoed back (indicated by red marker points)



### 3.5 Results and Discussion

Figure 3.20 shows the variation of mixed-mode SIF's for SEN specimen obtained using analytical (given in Appendix A) and experimental (DIC) method as a function of applied load. Experimentally obtained values are in reasonable agreement with the analytically obtained ones. Also, the variation of mode-I SIF is linear with respect to load. Average percentage error between the analytical and experimental (DIC) methods is found to be 10.24 %. The maximum error of 13.9 % is obtained at load of 2.5 kN; this is because overall values of displacement are very small at this load and inherent resolution limitation of DIC can be the reason for this value of percentage error.

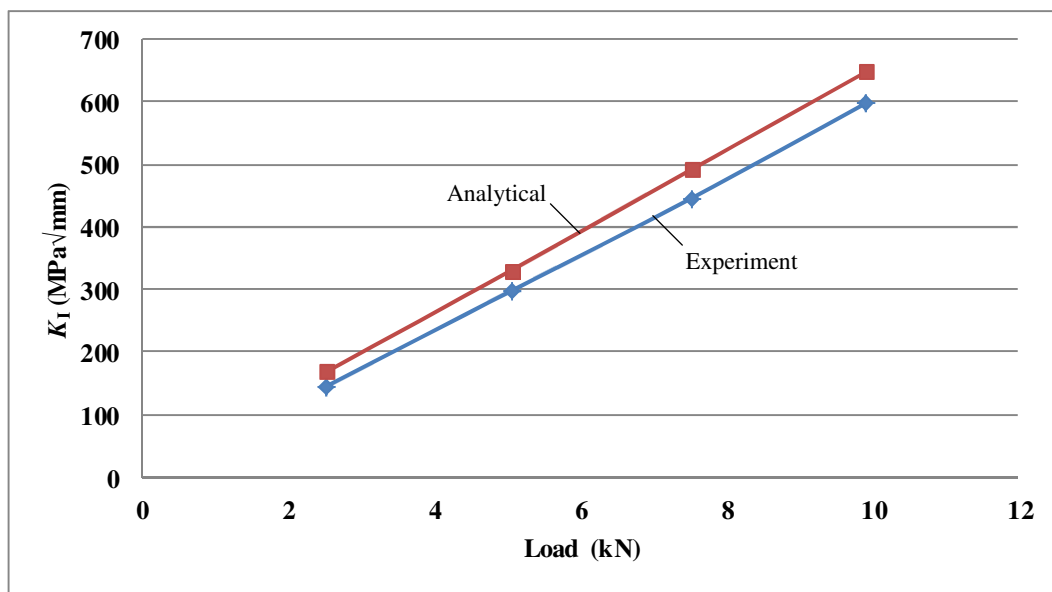


Fig. 3.20 showing the variation of mixed-mode SIF's for SEN specimen obtained using analytical and experimental (DIC) method as a function of applied load

Fig. 3.21 shows the variation of mixed-mode SIF's for CSC specimen obtained using analytical and experimental (DIC) method as a function of applied load. Values obtained by both methods are found to compare well. Both  $K_I$  and  $K_{II}$  are found to vary linearly as a function of load. Average percentage error between the analytical and experimental (DIC) values of  $K_I$  is 5.04% and for  $K_{II}$ , average percentage error is 11.24%. For  $K_{II}$ , the maximum error of 14.1 % is obtained at load of 3 kN which can be again attributed to resolution limitation of DIC for small displacement levels.

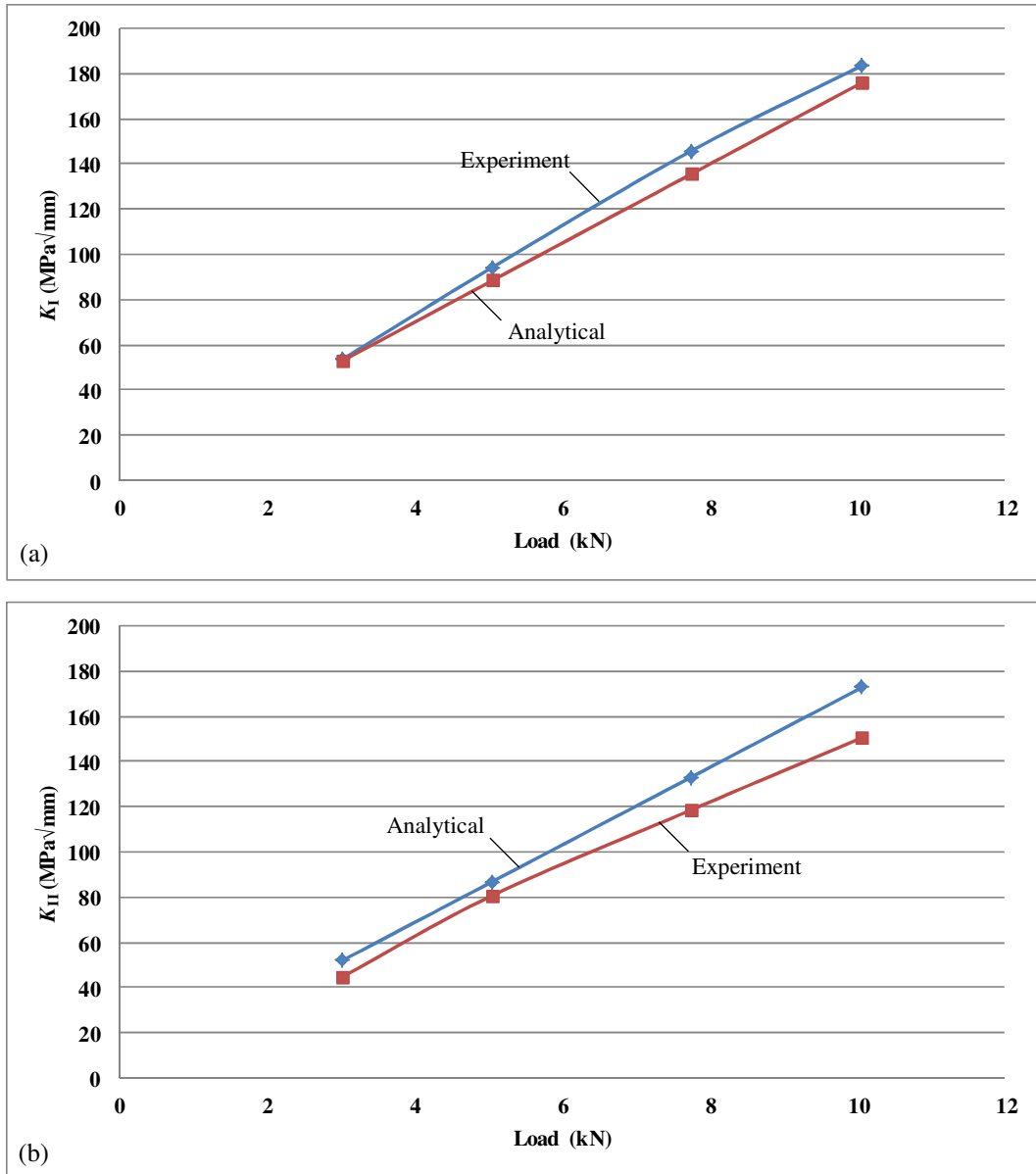


Fig. 3.21 showing the variation of mixed-mode SIF's for SEN specimen obtained using analytical and experimental (DIC) method as a function of applied load

Table 3.2 summarizes the values of mixed-mode SIF's for SCC and ESC specimens obtained using analytical (see Appendix A) and experimental (DIC) method for different loads. For both the specimens, SIF's are evaluated at sufficiently high loads due to the earlier mentioned reason of resolution limitation of DIC. For both the specimens, analytical and experimental results are found to show good agreement. Table 3.3 summarizes the values of mixed-mode SIF's for interacting parallel edge cracked panel obtained using analytical (see Appendix A), FEM (as described in chapter 2) and experimental (DIC) method.

Table 3.2 comparison of results for SCC and ESC specimen obtained by different methods

Specimen type	Load (kN)	$K_I$ (MPa√mm)		$K_{II}$ (MPa√mm)	
		Analytical	Experimental	Analytical	Experimental
SCC	10.04	340.503	337.637	----	----
	12.475	423.112	446.141	----	----
	15.098	512.091	505.942	----	----
ESC	6.029	204.986	187.3976	107.59	95.4341
	10.12	344.064	315.147	180.593	173.60

For interacting parallel edge cracked specimen, results of FEM and experimental method show good agreement; however, analytical results show significant deviation. This is because of the fact that analytical closed form solution has been derived by assuming semi-infinite geometry of interacting parallel edge cracked panel and hence underestimates the influence of finite geometry on the crack-tip stress conditions. However, in actual practice, the specimen is having finite geometry.

Table 3.3 comparison of results obtained by different methods for parallel edge cracked panel

Specimen type	$K_I$ (MPa√mm)				$K_{II}$ (MPa√mm)			
	Analytical	FEM ( <i>J</i> -integral Method)	Direct method	Exp.	Analytical	FEM ( <i>J</i> -integral Method)	Direct method	Exp.
Interacting parallel edge crack	555.9	750.544	750.59	684.172	81.6	107.434	107.41	110.5869

### 3.6 Closure

In the present work, a successful attempt has been made to estimate mixed-mode SIF's by using whole field displacement data from 3D-DIC. For this purpose, an over-deterministic non-linear least square approach has been implemented in modified form to achieve better and reliable rate of convergence. Theoretical reconstruction of contour maps of  $u$  and  $v$ -displacement components has been used to cross check whether converged solution is able to model the displacement field correctly. Data has been collected from wider zone along smoothened contours of  $u$  and  $v$ -displacements and the co-ordinates of the crack-tip are evaluated automatically. The methodology has been validated by applying it for the estimation of mixed-mode SIF's for five different fatigue pre-cracked specimens with different specimen geometries. The experimental results are found to compare well with the analytical solutions except for the case of interacting parallel edge cracked panel where analytical solution is not available for finite geometry configuration. In this case, experimental and FE results show good agreement. The slight difference between the analytical and experimental results can be due to the difference between the actual fatigue crack used in the experiments and the highly idealized model of crack used in analytical solution. This difference can be due to the reasons such as error introduced due to deviation of the crack plane from the horizontal plane of the camera, uneven fatigue crack-growth on both the sides of the specimen, non-planar crack growth, crack front curvature, crack closure and crack-tip blunting.

## Chapter 4

# Conclusion and Recommendations for Future Work

In this work, mixed-mode SIF's are estimated experimentally using digital photoelasticity and DIC. Although photoelasticity has been applied extensively in the field of fracture mechanics, there still exists a scope to improve the results obtained by digital photoelasticity using the techniques of digital image processing and the same has been explored in the present work. For the accurate evaluation of total isochromatic fringe order over the entire model domain, ten-step method has been employed. Then, using this whole field information, data has been collected in an automated manner using PSIF software. This automated data collection helped to avoid any human error and reduce the time required for data collection. Then, using the collected data as a required input, over-deterministic nonlinear procedure is invoked using FRINGPLOT software. The experimental (digital photoelastic) results showed a good agreement with FE and analytical results. The study also underlines the fact that although digital photoelasticity requires careful interpretation of experimental results, it gives the physical insight into the complex structural phenomena as shown in case of interacting parallel edge cracked panel subjected to uniaxial tensile load.

In present study, error introduced due to ambiguous location of the crack-tip has not been considered and can be exploited as an area of future scope. The influence of this error can be accounted by considering the co-ordinates of crack-tip location as one of the unknowns to be determined in the existing over-deterministic nonlinear least square technique. The complexities involved in doing so can be simplified by using the individual stress components obtained through whole field stress separation.

Because of the range of advantages DIC offers, its application in the field of fracture and damage mechanics has got a lot of potential. In the current work, for the sake of better and reliable convergence, modifications are proposed during implementation of the existing over-deterministic non-linear least square algorithm of Yoneyama. The converged solution is cross verified by the theoretical reconstruction of  $u$  and  $v$ -displacement contour maps. This method of reconstruction has been popular in the field of digital photoelasticity and the

same has been adopted in the context of DIC. The required whole field displacement data has been obtained using 3D-DIC set up. Data has been collected along the contours of  $u$  and  $v$ -displacement components. Using this data, MATLAB program is employed to estimate the mixed mode SIF's as well as the values of rigid body motion and position co-ordinates of crack-tip location. For the validation of the methodology, mixed-mode SIF's have been estimated for five different specimen configurations having varying mode-mixity. The results showed reasonable agreement with the analytical / FE estimates. The study emphasizes that DIC can be used as an effective and reliable tool in the field of fracture mechanics for the evaluation of mixed-mode SIF's.

In order to overcome the inherent resolution limitation of DIC, it is recommended to use high scale factors (pixels / mm) during experiments for low loads and for materials with high stiffness. A model needs to be developed in order to predict the sensitivity of this method to the error introduced due to misalignment between the camera plane and crack plane. Also, the modified form of the presented algorithm can be employed to determine mixed-mode dynamic SIF's for a propagating crack.

# Appendix A

## Analytical Solutions

### A.1 Single Edge Notched (SEN) specimen [1]

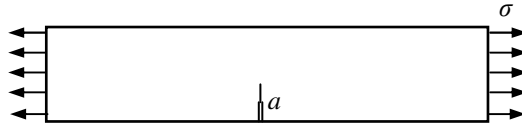


Fig A.1 SEN specimen geometry

$$K_I = \sigma \sqrt{\pi a} \cdot F_I(\alpha)$$

where,

$W$  = width of specimen

$$\alpha = \frac{a}{W}$$

$$F_I(\alpha) = 1.12 - 0.231\alpha + 10.55\alpha^2 - 21.72\alpha^3 + 30.39\alpha^4$$

### A.2 Single Center Cracked (SCC) specimen [1]

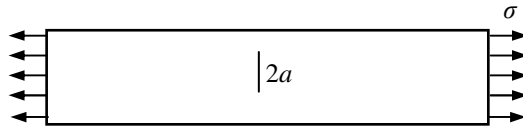


Fig A.2 SCC specimen geometry

$$K_I = \sigma \sqrt{\pi a} \cdot F_I^*(\alpha)$$

where,

$W$  = width of specimen

$$\alpha = \frac{2a}{W}$$

$$F_I(\alpha) = \sqrt{\sec\left(\frac{\alpha\pi}{2}\right)}$$

$$F_I^*(\alpha) = (1 - 0.025\alpha^2 + 0.06\alpha^4)F_I(\alpha)$$

### A.3 Edge Slant Cracked (ESC) specimen [1]

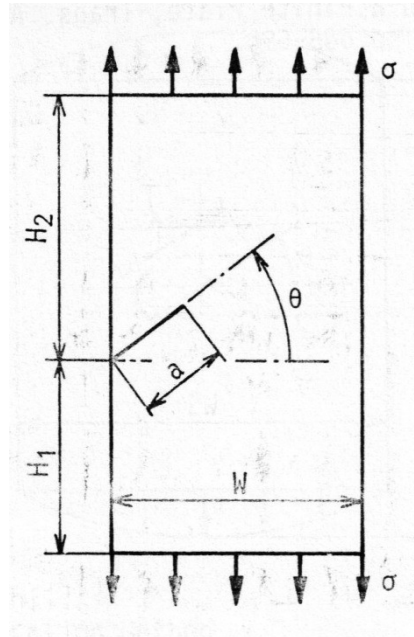


Fig A.3 ESC specimen geometry

$$K_I = \sigma \sqrt{\pi a} \cdot F_I$$

$$K_{II} = \sigma \sqrt{\pi a} \cdot F_{II}$$

where,

$\sigma$  = far field applied stress

The values of  $F_I$  and  $F_{II}$  can be obtained from Fig. A.4.

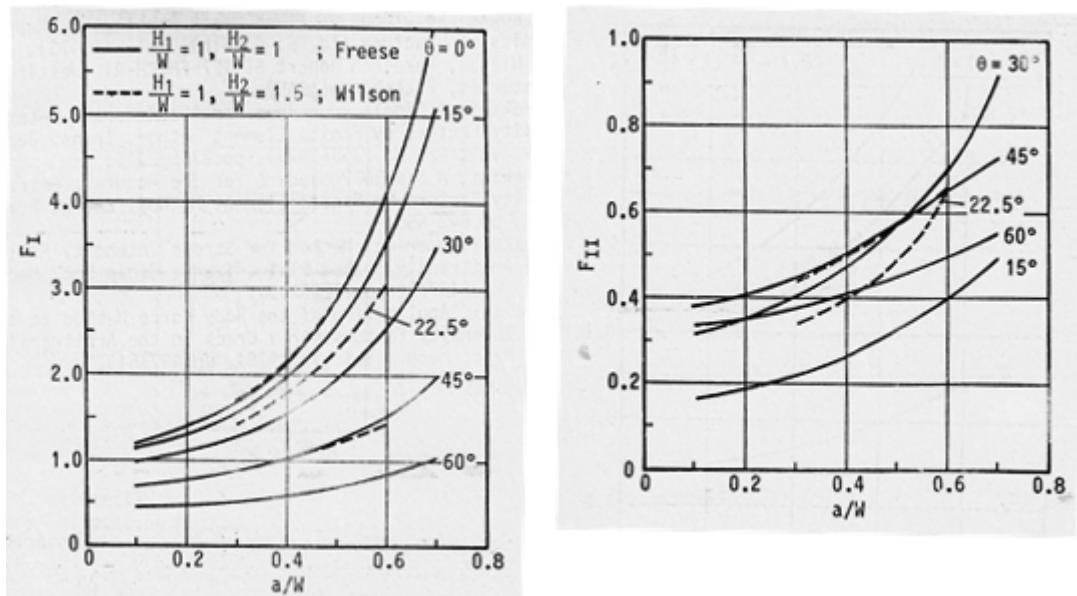


Fig A.4  $F_I$  and  $F_{II}$  for ESC specimen [1]



#### A.4 Center Slant Cracked (CSC) specimen

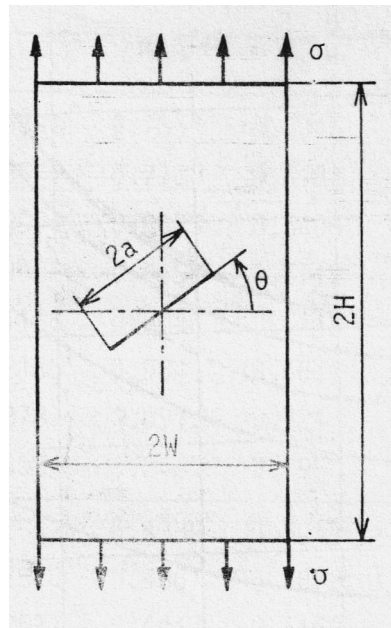


Fig A.5 CSC specimen geometry

$$K_I = \sigma \sqrt{\pi a} \cdot F_I$$

$$K_{II} = \sigma \sqrt{\pi a} \cdot F_{II}$$

where,  $\sigma$  = far field applied stress

The values of  $F_I$  and  $F_{II}$  can be obtained from Fig. A.6.

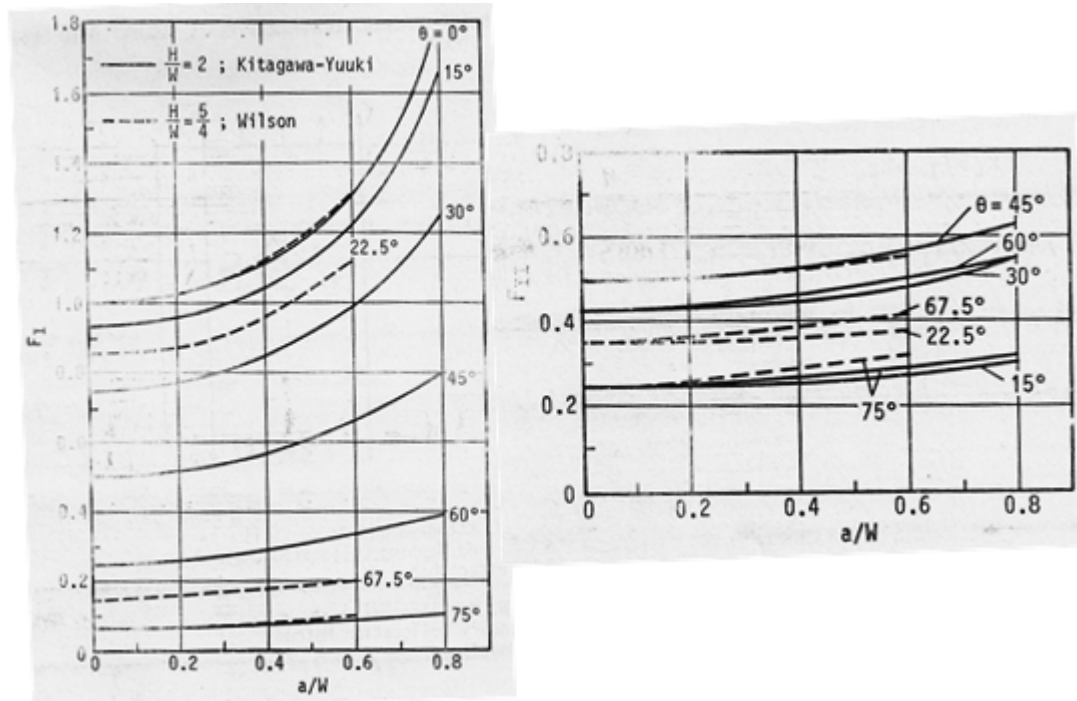


Fig A.6  $F_I$  and  $F_{II}$  for CSC specimen [1]

### A.5 Parallel Edge Cracks in Semi-Infinite Plate [1]

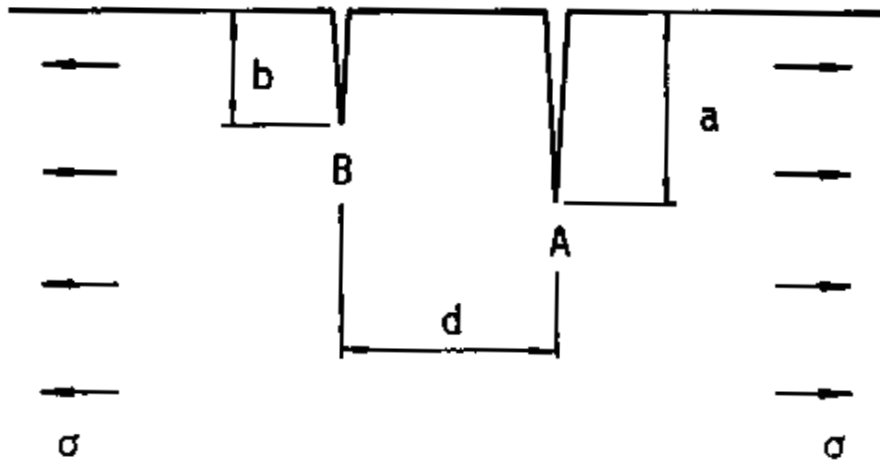


Fig. A.7 Parallel edge cracks in semi-infinite plate specimen [1]

$$K_{IA} = \sigma \sqrt{\pi a} \cdot F_{IA}$$

$$K_{IB} = \sigma \sqrt{\pi b} \cdot F_{IB}$$

$$K_{IIA} = \sigma \sqrt{\pi a} \cdot F_{IIA}$$

$$K_{IIB} = \sigma \sqrt{\pi b} \cdot F_{IIB}$$

where,  $\sigma$  = far field applied stress

The values of  $F_I$  and  $F_{II}$  can be obtained from Fig. A.8.

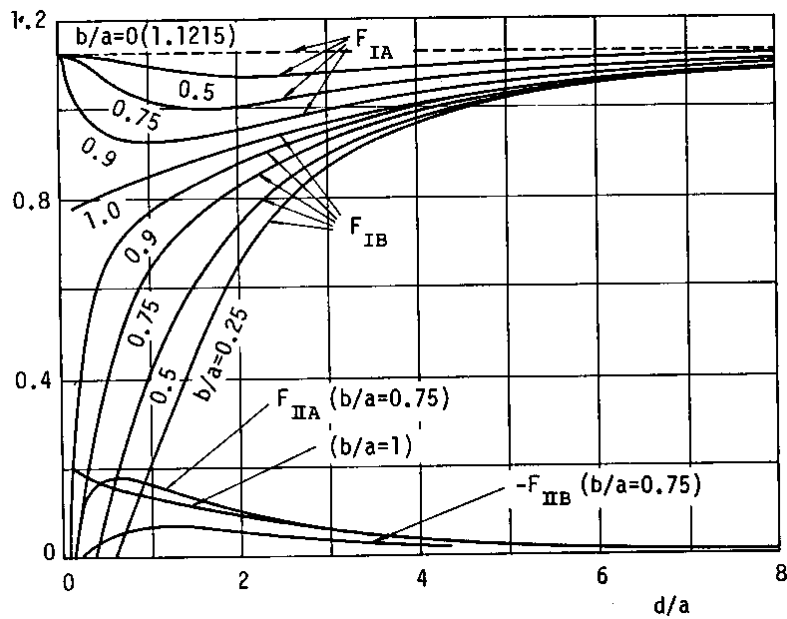
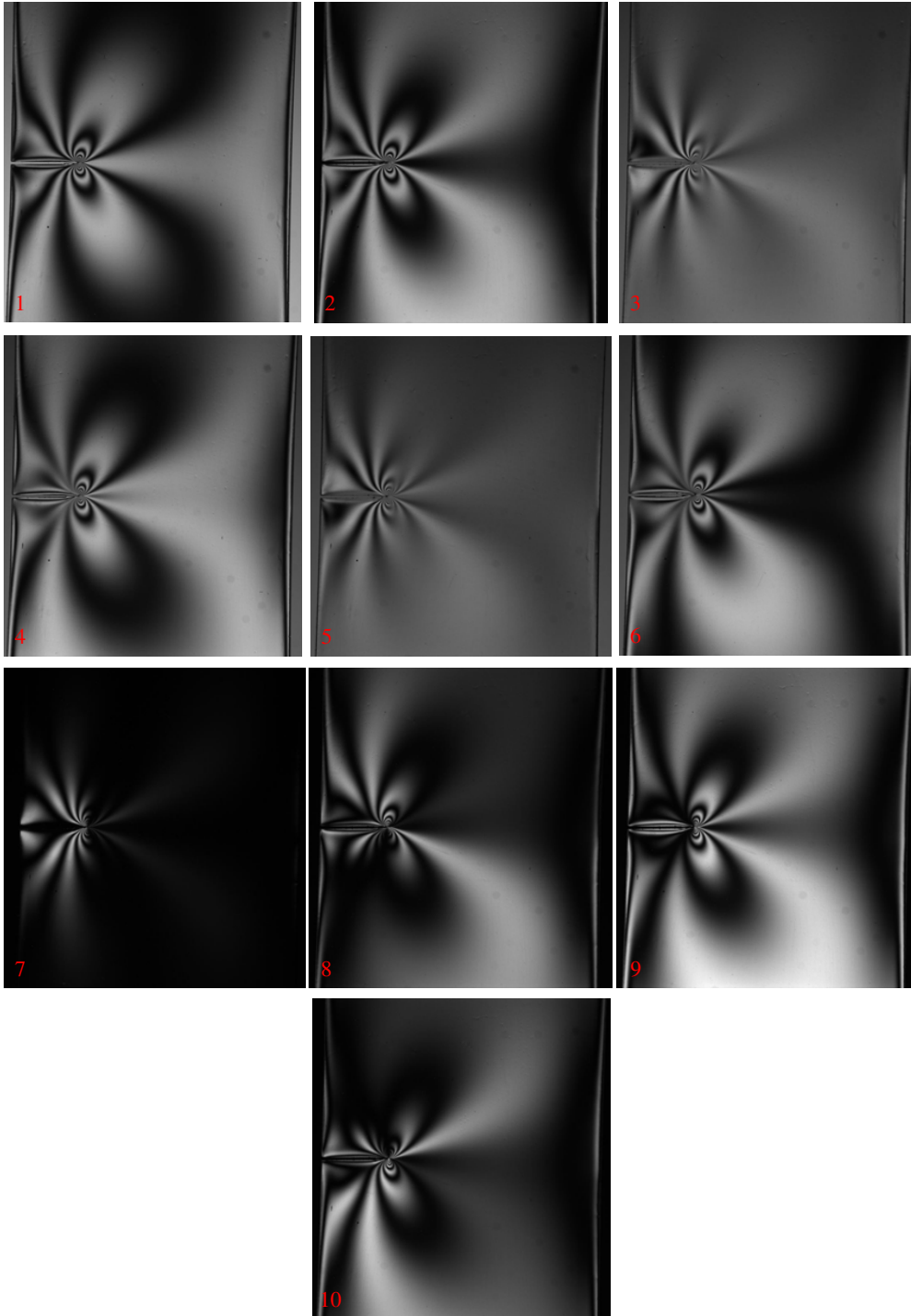


Fig. A.8  $F_I$  and  $F_{II}$  for parallel edge cracks in semi-infinite plate specimen [1]

## Appendix B

### Ten-step images for SEN specimen



# Appendix C

## Effect of Rigid Body Rotation

### C.1 Derivation

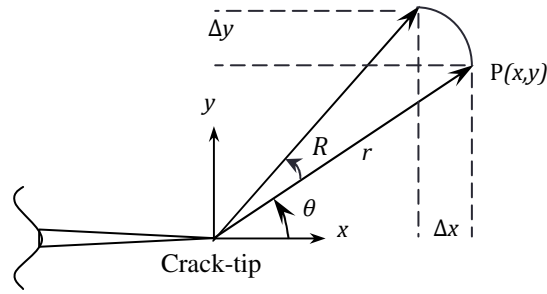


Fig. B.1 Effect of rigid body rotation

$$\Delta x = r \{ \cos(\theta + R) - \cos \theta \}$$

$$\Delta x = r \{ \cos \theta (\cos R - 1) - \sin \theta \sin R \}$$

$$\Delta x = x (\cos R - 1) - y \sin R$$

$$\Delta y = r \{ \sin(\theta + R) - \sin \theta \}$$

$$\Delta y = r \{ \sin \theta (\cos R - 1) + \cos \theta \sin R \}$$

$$\Delta y = y (\cos R - 1) + x \sin R$$

# Appendix D

## Fracture parameters obtained from DIC

### D.1 Single Edge Notched (SEN) specimen

Mode I parameters	Mode II parameters
$A_{I1} = 177.81$	$A_{II1} = -0.047431$
$A_{I2} = -10.124$	$A_{II2} = 0.000000$
$A_{I3} = 1.6883$	$A_{II3} = -0.14661$
$A_{I4} = -0.1195$	$A_{II4} = -0.073595$

Convergence error obtained: 0.00023749

Load applied: 7.5 kN

### D.2 Single Center Cracked (SCC) specimen

Mode I parameters	Mode II parameters
$A_{I1} = 201.25$	$A_{II1} = 13.629$
$A_{I2} = -30.542$	$A_{II2} = 0.000000$
$A_{I3} = 10.714$	$A_{II3} = -1.3027$
$A_{I4} = -0.20795$	$A_{II4} = 0.90072$
$A_{I5} = -0.31775$	$A_{II5} = -0.052226$
$A_{I6} = 0.059356$	$A_{II6} = -0.024922$
$A_{I7} = -0.0082543$	$A_{II7} = 0.0042646$

Convergence error obtained: 0.00032114

Load applied: 15 kN

### D.3 Center Slant Cracked (CSC) specimen

Mode I parameters	Mode II parameters
$A_{I1} = 73.271$	$A_{II1} = -60.064$
$A_{I2} = -1.343$	$A_{II2} = 0.000000$
$A_{I3} = 4.5159$	$A_{II3} = -4.4906$
$A_{I4} = -0.078264$	$A_{II4} = 0.63045$
$A_{I5} = -0.1865$	$A_{II5} = 0.07619$
$A_{I6} = 0.029077$	$A_{II6} = -0.037349$
$A_{I7} = -0.0038324$	$A_{II7} = 0.00054375$

Convergence error: 0.00015964

Load: 10 kN

### D.4 Edge Slant Cracked (ESC) specimen

Mode I parameters	Mode II parameters
$A_{I1} = 125.73$	$A_{II1} = -69.257$
$A_{I2} = 4.8687$	$A_{II2} = 0.000000$
$A_{I3} = -0.50672$	$A_{II3} = -2.9435$
$A_{I4} = 0.089751$	$A_{II4} = 0.77449$

Convergence error: 0.00017733

Load: 10 kN

### D.5 Interacting Parallel Edge Cracked Plate

Mode I parameters	Mode II parameters
$A_{I1} = 272.95$	$A_{II1} = 44.118$
$A_{I2} = -23.149$	$A_{II2} = 0.000000$
$A_{I3} = 11.709$	$A_{II3} = 0.3727$
$A_{I4} = -1.9216$	$A_{II4} = 0.89202$
$A_{I5} = 0.30229$	$A_{II5} = -0.23869$
$A_{I6} = 0.0993$	$A_{II6} = 0.082925$
$A_{I7} = -0.059421$	$A_{II7} = -0.0084476$
$A_{I8} = 0.0050371$	$A_{II8} = 0.0018969$

Convergence error: 0.00026847

Load: 15 kN

# References

- [1] Y. Murakami, (ed.) Stress Intensity Factors Handbook, Pergamon, Oxford, (1987).
- [2] T. D. Dudderar and H. J. Gormanm, The Determination of Mode I Stress-intensity Factors by Holographic Interferometry, *Experimental Mechanics*, 13(4), (1973) 145-149.
- [3] A.J. Moore and J.R. Tyrer, Phase-stepped ESPI and Moiré Interferometry for Measuring Stress-intensity Factor and *J*-Integral, *Experimental Mechanics*, 35(4), (1995) 306-314.
- [4] H.P. Rossmanith, Analysis of crack-tip Moiré fringe patterns, *Int. Journal of Fracture*, 21, (1983) 83-106.
- [5] S. Ramaswamy, H. V. Tippur and L. Xu, Mixed-mode crack-tip deformations studied using a modified flexural specimen and coherent gradient sensing, *Experimental Mechanics*, 33(3), (1993) 218-227.
- [6] Yuichi Kawagishi, Masayuki Shozu, Yukio Hirose, Experimental evaluation of stress field around crack tip by caustic method, *Mechanics of Materials*, 33, (2001) 741-757.
- [7] J.W. Dally and R.J. Sanford, Classification of Stress-intensity Factors from Isochromatic-fringe Patterns, *Experimental Mechanics*, 18(12), (1978) 441-448.
- [8] R.J. Sanford and J.W. Dally, A general method for determining mixed-mode stress intensity factors from isochromatic fringe patterns, *Engineering Fracture Mechanics*, 11, (1979) 621-633.
- [9] Robert J. Sanford, Application of the Least-squares method to Photoelastic Analysis, *Experimental Mechanics*, 20(6), (1980) 192-197.
- [10] C.W. Smith and O. Olaosebikan, Use of mixed-mode stress-intensity algorithms for photoelastic data, *Experimental Mechanics*, 24(4), (1984) 300-307.
- [11] H. Nigam and A. Shukla, Comparison of the techniques of transmitted caustics and photoelasticity as applied to fracture, *Experimental Mechanics*, 28(2), (1988) 123-131.
- [12] A. Mehdi-Soozani, I. Miskioglu, C. P. Burger and T. J. Rudolphi, Stress intensity factors for interacting cracks, *Engineering Fracture Mechanics*, 27 (1987) 345-359.
- [13] Robert J. Sanford, Determining fracture parameters with full-field optical methods, *Experimental Mechanics*, 29(3), 1989, 241-247.
- [14] C. Taudou and K. Ravi-Chandar, Experimental determination of the dynamic stress-intensity factor using caustics and photoelasticity, *Experimental Mechanics*, 32(3), (1992) 203-210.



- [15] K. Ramesh, S. Gupta and A. A. Kelkar, Evaluation of stress field parameters in fracture mechanics by photoelasticity – revisited, *Engineering Fracture Mechanics*, 56, (1997) 25-45.
- [16] M. Guagliano, M. Sangirardi, A. Sciuccati, M. Zakeri, Multiparameter Analysis Of The Stress Field Around A Crack Tip, *Procedia Engineering*, 10, (2011) 2931–2936
- [17] Michael A. Sutton, Jean-José Orteu and Hubert W. Schreier, *Image Correlation for Shape, Motion and Deformation Measurements: Basic Concepts, Theory and Applications*, (Springer- Verlag, Berlin, 2009).
- [18] M.A. Sutton, J.H. Yan, V. Tiwari, H.W. Schreier, J.J. Orteu, The effect of out-of-plane motion on 2D and 3D digital image correlation measurements, *Optics and Lasers in Engineering*, 46, (2008) 746-757.
- [19] Bing Pan, Kemao Qian, Huimin Xie and Anand Asundi, Two-dimensional digital image correlation for in-plane displacement and strain measurement: a review, *Meas. Sci. Technol.*, 20, (2009) 062001 (17pp).
- [20] Michael A. Sutton, *Digital Image Correlation for Shape and Deformation Measurements*, Springer Handbook of Experimental Solid Mechanics, Part C, (2008) 565-600.
- [21] D. B. Barker, R. J. Sanford and R. Chona, Determining  $K$  and related stress-field parameters from displacement fields, *Experimental Mechanics*, 25(4), (1985) 399-407.
- [22] S.R. McNeill, W.H. Peters, M.A. Sutton, Estimation of stress intensity factor by digital image correlation, *Engineering Fracture Mechanics*, 28(1), (1987) 101-112.
- [23] M.A. Sutton, J.L. Turner, Y.J. Chao, H.A. Bruck and T.L. Chae, Experimental investigations of three-dimensional effects near a crack tip using computer vision, *International Journal of Fracture*, 53, (1992) 201-228.
- [24] P. F. Luo, Y. J. Chao, M. A. Sutton and W. H. Peters, Accurate measurement of three-dimensional deformations in deformable and rigid bodies using computer vision, *Experimental Mechanics*, 33(2), (1993) 123-132.
- [25] G. Han, M.A. Sutton and Y.J. Chao, A Study of Stationary Crack-tip Deformation Fields in Thin Sheets by Computer Vision, *Experimental Mechanics*, 34, (2), (1994) 125-140.
- [26] Y. J. Chao, P. F. Luo and J. F. Kalthoff, An Experimental Study of the Deformation Fields Around a Propagating Crack Tip, *Experimental Mechanics*, *Experimental Mechanics*, 38(2), (1998) 79-85.
- [27] P.F. Luo and F.C. Huang, Application of stereo vision to the study of mixed-mode crack-tip deformations, *Optics and Lasers in Engineering*, 33, (2000) 349-368.

- [28] S. Yoneyama, Y. Morimoto and M. Takashi, Automatic Evaluation of Mixed-mode Stress Intensity Factors Utilizing Digital Image Correlation, *Strain*, 42, (2006) 21–29.
- [29] S. Yoneyama, T. Ogawa and Y. Kobayashi, Evaluating mixed-mode stress intensity factors from full-field displacement fields obtained by optical methods, *Engineering Fracture Mechanics*, 74(9), (2007) 1399-1412.
- [30] P. López-Crespo, R.L. Burguete, E.A. Patterson, A. Shterenlikht, P.J. Withers and J.R. Yates, Study of a Crack at a Fastener Hole by Digital Image Correlation, *Experimental Mechanics*, 49(4), (2009) 551-559.
- [31] Rui Zhang and Lingfeng He, Measurement of mixed-mode stress intensity factors using digital image correlation method, *Optics and Lasers in Engineering*, 50(7), (2012) 1001-1007.
- [32] E.E. Gdoutos and P.S. Theocaris, A Photoelastic Determination of Mixed-mode Stress-intensity Factors, *Experimental Mechanics*, 18(3), (1978), 87-97.
- [33] M. A. Schroedl, J. J. McGowan and C. W. Smith, An assessment of factors influencing data obtained by the photoelastic stress freezing technique for stress fields near crack tips, *Engineering Fracture Mechanics*, 4, (1972) 801-809.
- [34] Rafael Picon, Federico Paris, Jose Cañas and Juan Marin, A complete field method for the photoelastic determination of  $K_I$  and  $K_{II}$  in general mixed-mode fracture, *Engineering Fracture Mechanics*, 51(3), (1995) 505-516.
- [35] Ramesh K., *Digital Photoelasticity: Advanced techniques and applications*, (Springer-Verlag, Berlin, 2000).
- [36] M. Ramji and K. Ramesh, Whole field evaluation of stress field components in digital photoelasticity – Issues, implementation and application, *Optics and Lasers in Engineering*, 46, (2008) 257-251.
- [37] M. Ramji and R.G.R. Prasath, Sensitivity of isoclinic data using various phase shifting techniques in digital photoelasticity towards generalizes error sources, *Optics and Lasers in Engineering*, 49, (2011) 1153-1167.
- [38] M. Ramji and K. Ramesh, Adaptive Quality guided phase unwrapping algorithm for Whole field Digital photoelastic parameter estimation, *Strain*, 46(2), (2010) 184-194.
- [39] R.G.R. Prasath, PSIF and FRINGE PLOT, Engineering Optics Lab, Department of Mechanical Engineering, IIT Hyderabad.
- [40] Erdogan Madenci, Ibrahim Guven, *The Finite Element Method and Applications in Engineering using ANSYS* (Springer, 2006).
- [41] T. L. Anderson, *Fracture Mechanics Fundamentals and Applications*, 3rd edition, (CRC Press, 2005).

- [42] H. Hosseini-Toudeshky, H. Shahverdi and H. R. Daghyani, Fatigu life assessment of repaired panels with adhesively bonded composite plates In: Second Asian-Australian conference on composite materials, ACCM-2000, Kyonju, Korea (August 2000) 18-20.
- [43] Hossein Hosseini-Toudeshky, Bijan Mohammadi and Hamid Reza Daghyani, Mixed-mode fracture analysis of aluminum repaired panels using composite patches, Composite Science and Technology, 66, (2006) 188-198.
- [44] M. Ramji, R. Srilakshmi, Finite Element Modeling of Composite Patch repair, 5th International Conference on Theoretical, Applied Computational and Experimental Mechanics, IIT Kharagpur, India (2010).
- [45] ANSYS, Version 12.1, Theory reference ANSYS, Inc.
- [46] MATLAB R2010a, MathWorks Inc., Natick, USA; 2000
- [47] VicSnap / Vic-3D software, Correlated Solutions, Inc.; (<http://www.correlatedsolutions.com/>)
- [48] Evaluation of properties of Zircalloy using Digital Image Correlation Technique, Atomic Energy Regulatory Board (AERB), two years - ongoing
- [49] G. P. Mogadpalli and V. Parameswaran, Determination of Stress Intensity Factor for Cracks in Orthotropic Composite Materials using Digital Image Correlation, Strain, 44, (2008), 446–452.